PACIFIC TELECONNECTIONS DYNAMICS IN A CHANGING CLIMATE: THEORIES, OBSERVATIONS, AND MODELS

A Dissertation
Presented to
The Academic Faculty

By

Youngji Joh

In Partial Fulfillment
of the Requirements for the Degree Doctor
of Philosophy in the
School of Earth and Atmospheric Sciences

Georgia Institute of Technology

December 2020

PACIFIC TELECONNECTIONS DYNAMICS IN A CHANGING CLIMATE: THEORIES, OBSERVATIONS, AND MODELS

Approved by:

Dr. Emanuele Di Lorenzo, Advisor
School of Earth & Atmospheric Sciences
Georgia Institute of Technology

Dr. Taka Ito
School of Earth & Atmospheric Sciences
Georgia Institute of Technology

Dr. Jie He
School of Earth & Atmospheric Sciences
Georgia Institute of Technology

Dr. Antonietta Capotondi
National Oceanic and Atmospheric Administration (NOAA)

Dr. Benjamin Kirtman
Rosenstiel School for Marine and Atmospheric Science
University of Miami

Date Approved: September 3, 2020

나의 사랑하는 친구 병진에게

ACKNOWLEDGEMENTS

Commit your actions to the LORD, and your plans will succeed.
Proverbs 16:3

TABLE OF CONTENTS

LIST OF FIGURES

SUMMARY

Pacific climate and weather extreme events such as heatwaves, drought, and hydrological extremes, which drive economically significant changes along the US, are dynamically linked large-scale climate variability (e.g., North Pacific decadal variability and El Niño Southern Oscillation). This work aims at improving the current understanding of the role of climate coupling within the Pacific system and investigating their changes and response to anthropogenic forcing.

Using multiple observational reanalyses and reanalysis products and a 30-member global climate model ensemble, we show that prolonged multi-year marine heatwaves are linked to the dynamics of the two dominant modes of winter sea surface temperature variability in the North Pacific, the Pacific Decadal Oscillation (PDO) and the North Pacific Gyre Oscillation (NPGO). Specifically, we find a significant correlation between winter warm NPGO anomalies and the following winter PDO arising from extra-tropical/tropical teleconnections. Our work reports that marine heatwaves in the North Pacific are becoming stronger in amplitude with a larger area as well as more persistent under anthropogenic forcing.

We next propose that a preferred decadal timescale in the KE may arise from the interaction between the KE and the extra-tropical/tropical Pacific variability. We show that changes in the KE states apply a persistent downstream atmospheric response (e.g., wind stress curl, 0-12 months timescales) that projects on the atmospheric forcing of the Pacific Meridional Modes (PMM) over 9 months timescales. Subsequently, the PMM energizes the central tropical Pacific El Niño Southern Oscillation (CP-ENSO) and its atmospheric teleconnections back to the Northern Hemisphere (1-3 months timescale), which in turn excites oceanic Rossby waves in the central/eastern North Pacific that propagate westward changing the KE (~3 years timescales). Consistent with this hypothesis, we provide a cross-correlation function between the KE and the PMM/CP-ENSO indices exhibiting a significant sinusoidal shape corresponding to a preferred spectral power at decadal timescales (~10 years).

Finally, through combining observations, numerical simulations, and empirical dynamical models, we confirm that KE and the tropical Pacific are dynamically linked, especially during the recent decades. The statistical differences between the KE properties before and after the mid-1980 suggest non-stationary decadal KE variability. Moreover, the KE interaction with the CP-ENSO has been increasing in a changing climate. We discuss the link of the enhanced extratropical-tropical coupled KE system with the potential impact of anthropogenic forcing and changes in the KE atmospheric downstream response with stronger subtropical wind forcing and subsequent favorable conditions for Pacific Meridional modes and CP-ENSO. These results imply that the higher amplitude quasi-decadal fluctuations of KE/CP-ENSO may lead to a stronger basis for decadal predictions of the Pacific region, especially for societally relevant biogeochemical quantities (e.g., salinity, oxygen, and chlorophyll-A) and fisheries.

CHAPTER 1. INTRODUCTION

Climate in the Pacific region is well known to vary on decadal timescales and has been received attention due to the substantial impact on weather patterns and marine ecosystems over the Pacific sector [e.g., *Liu et al., 2012; Minobe 1996;*]. While dominant modes of Pacific decadal climate variability have been discussed extensively in previous literatures, the mechanisms that control the long-term climate variations are still unclear. In particular, the dynamical links between extratropical and tropical Pacific play a key role in the dynamics and origin of the interdecadal and decadal modes of the Pacific climate system [*Liu and Alexander, 2007; Alexander et al., 2002; Di Lorenzo et al., 2015*]. An improved understanding of the "deterministic" underlying dynamics that couple the extratropical and tropical Pacific will not only lead to better understanding of Pacific decadal variability but also of the predictability of the climate system.

1.1 Background and motivation

An important mechanism linking the North Pacific and the tropics is the Pacific Meridional Modes (PMM), which is known as the precursor of El Niño Southern Oscillation (ENSO) and is excited by local midlatitude stochastic forcing [e.g., *Chowdary et al., 2012; Wang and Mehta, 2008; Vimont et al., 2001; 2003*] as well as the high-frequency North Pacific atmospheric variability (e.g., North Pacific Oscillation, NPO) [*Rogers, 1981; Linkin and Nigam 2008*]. Specifically, positive feedback of wind-induced latent heat flux and SST anomalies (Wind-evaporation-SST feedback, WES feedback, *Xie 1999*), propagates coupled surface wind and SST anomalies from the subtropics onto the tropics during the spring season. The PMM is also termed as the "seasonal footprinting mechanism" because the mid-latitude stochastic forcing that triggers the PMM and the subsequent ENSO are locked with

the seasonal cycle starting in the winter/spring (PMM) and ending in the following fall/winter (ENSO). [*Chiang and Vimont 2004; Chang et al. 2007; Larson and Kirtman 2013*]. Recent findings suggest that PMM may collectively contribute to tropical Pacific decadal variability, exhibiting significant periodicities longer than ~5 years associated with reddening of oceanic response to white-noise atmospheric forcing [*Chiang and Vimont, 2004; You and Furtado, 2018; Zhang et al., 2014*]. While much of the PMM dynamics have been explained in the context of air-sea coupling, we also recognize that the atmospheric stochastic forcing associated with the initiation of the PMM is also favoring the development of ENSO through the wind-induced oceanic waves (e.g., downwelling equatorial Kelvin waves) [Alexander et al., 2010; Capotondi et al., 2015].

On the other hand, the ENSO has a significant impact on global climate and weather, especially the North Pacific region, through the ENSO-driven large-scale atmospheric teleconnections as the dynamic link from the tropical to extratropical Pacific [e.g., *Atmospheric bridge, Alexander et al., 2002*]. By altering the near-surface air temperature, wind, and the distribution of clouds over the equatorial Pacific, the resulting variations in mid-latitude surface heat and momentum fluxes induce changes in sea surface height, temperature, wind, and mixed layer depth over the North Pacific [*Trenberth et al., 1998*; *Liu and Alexander, 2007; Alexander et al., 2002*]. ENSO and the tropical Pacific decadal variability thus exert a strong influence on Pacific decadal climate modes such as Pacific Decadal Oscillation (PDO, *Mantua et al., 1997; Zhang et al., 1997*) and the North Pacific Gyre Oscillation (NPGO, *Di Lorenzo et al., 2008*). Specifically, when the ENSO events peak during boreal winter, the excited atmospheric stationary waves (e.g., Pacific-North-America (PNA) pattern) project the North Pacific internal atmospheric variability (e.g., Aleutian Low and NPO), changing the wind-driven mixing, surface heat fluxes, and Ekman

transport in the upper ocean over the central Pacific [*Yu and Zwier, 2007*; *Alexander et al. 2002; Alexander and Scott 2008; see also Strong and Magnusdottir 2009*]. As the result of a combination of remote tropical forcing and mid-latitude air-sea interactions, the atmospheric anomalies in the Aleutian Low or NPO excite and drive the westward-propagating oceanic Rossby waves (e.g., the PDO and NPGO sea surface height signals) that reach and impact the western boundary current systems (WBCs) in the Pacific region.

The goal of this thesis is to explore and improve our fundamental understanding of the mechanisms of Pacific extratropical-tropical interactions, and their role in contributing to climate extremes (e.g., marine heatwaves) and their sensitivity to anthropogenic changing climate.

A diagnostic of ocean extremes statistics in past observations and in future model projections under the radiative forcing scenario is provided in Chapter 2. Using the examination of observation reanalysis product and global climate model ensemble, we investigate the mechanisms underlying the generation and evolution of ocean temperature extremes in the North Pacific (e.g., the 2014/15, the 2019) and the relation to the Pacific decadal variability. Chapter 2 is organized around two key questions: (1) Do prolonged ocean extremes events follow recurrent patterns with a transition from a winter NPGO-like pattern to PDO-like pattern in the following winter? and (2) how the coupling between these modes via tropical/extra-tropical teleconnections is changing under a warmer climate favoring more prolonged winter to winter warm events?

The examination of a mechanistic hypothesis for exploring a new set of decadal climate interactions between the North Pacific western boundary current and the tropical Pacific are presented in Chapter 3 and Chapter 4. Using observations, numerical

simulations, and empirical dynamical models, we introduce an expanded hypothesis for the decadal KE dynamic system and provide supporting evidence through a set of statistical analyses. Chapter 3 and 4 are organized with the following key questions: (1) Is the preferred decadal timescale in the KE linked to the interaction between KE and the central tropical Pacific? (2) Consistent with observational results, do numerical simulations and empirical dynamical model also capture the extratropical-tropical coupled KE system? (3) Is the interaction between KE and tropical Pacific changing in a warmer climate?

1.2 References

Liu, Z. & Alexander, M. Atmospheric bridge, oceanic tunnel, and global climatic teleconnections, *Rev. Geophys*. **45**, RG2005 (2007).

Minobe, S., 1996: Interdecadal temperature variation of deep water in the Japan Sea (East Sea).Proc. Fourth CREAMS Workshop, Vladivostok, Russia, CREAMS secretariat, 81–88.

Solomon A, Shin SI, Alexander MA, McCreary JP. The relative importance of tropical variability forced from the North Pacific through ocean pathways. Clim Dyn. 2008;31:315–31.

Alexander, M. A., I. Blade, M. Newman, J. R. Lanzante, N. C. Lau, and J. D. Scott (2002), The atmospheric bridge: The influence of ENSO teleconnections on air-sea interaction over the global oceans, *Journal of Climate*, 15(16), 2205-2231.

Chowdary JS, Xie S-P, Tokinaga H, Okumura YM, Kubota H, Johnson NC, Zheng X-T (2012) Inter-decadal variations in ENSO teleconnection to the Indo-western Pacific for 1870–2007. J Clim 25:1722–1744

Wang, H., and V. M. Mehta, 2008: Decadal variability of the IndoPacific warm pool and its association with atmospheric and oceanic variability in the NCEPNCAR and SODA reanalyses. J. Climate, 21, 5545−5565.

Vimont DJ, Battisti DS, Hirst AC. Footprinting: a seasonal connection between the tropics and mid-latitudes. Geophys Res Lett. 2001;28:3923–6.

Vimont DJ, Battisti DS, Hirst AC. The seasonal footprinting mechanism in the CSIRO general circulation models. J Clim. 2003;16: 2653–67. https://doi.org/10.1175/1520-0442(2003)016<2653: TSFMIT>2.0.CO;2.

Rogers, J. C. The North Pacific oscillation. *J. Climatol.* https://doi.org/10.1002/joc.3370010106 (1981).

Linkin ME, Nigam S. The North Pacific oscillation-West Pacific teleconnection pattern:mature-phase structure and winter impacts. J Clim. 2008;21:1979–97.

Xie S. P. A dynamic ocean–atmosphere model of the tropical Atlantic decadal variability. *J. Climate* **12**, 64–70 (1999).

Chiang, J. C. H., and D. J. Vimont (2004), Analogous Pacific and Atlantic meridional modes of tropical atmosphere-ocean variability, *Journal of Climate*, 17(21), 4143-4158.

Chang, P., L. Zhang, R. Saravanan, D. J. Vimont, J. C. H. Chiang, L. Ji, H. Seidel, and M. K. Tippett (2007), Pacific meridional mode and El Nino-southern oscillation, *Geophysical Research Letters*, 34(16).

Larson, S., and B. P. Kirtman, 2013: The Pacific meridional mode as a trigger for ENSO in a high-resolution coupled model. Geophys. Res. Lett., 40, 3189–3194, doi:10.1002/grl.50571.

You, Y. J., and J. C. Furtado (2017), The role of South Pacific atmospheric variability in the development of different types of ENSO, Geophys Res Lett, 44(14), 7438-7446.

Alexander, M. A., D. J. Vimont, P. Chang, and J. D. Scott (2010), The Impact of Extratropical Atmospheric Variability on ENSO: Testing the Seasonal Footprinting Mechanism Using Coupled Model Experiments, *Journal of Climate*, 23(11), 2885-2901.

Capotondi, A., and Sardeshmukh, P. D. Optimal precursors of different types of ENSO events. *Geophys. Res. Lett.*, **42**, 9952–9960 (2015) https://doi.org/10.1002/2015GL066171.

Trenberth, K. E., Branstator, G. W., Karoly, D., Kumar, A., Lau, N. C. & Ropelewski, C. Progress during TOGA in understanding and modeling global teleconnections associated with tropical sea surface temperatures. *J. Geophys. Res*. **103**, 14,291–14,324 (1998).

Liu, Z. & Alexander, M. Atmospheric bridge, oceanic tunnel, and global climatic teleconnections, *Rev. Geophys*. **45**, RG2005 (2007).

Mantua, N. J., S. R. Hare, Y. Zhang, J. M. Wallace, and R. C. Francis (1997), A Pacific interdecadal climate oscillation with impacts on salmon production, *Bulletin of the American Meteorological Society*, 78(6), 1069-1079.

Zhang, Y., J. M. Wallace, and D. S. Battisti (1997), ENSO-like interdecadal variability: 1900- 93, *Journal of Climate*, 10(5), 1004-1020.

Di Lorenzo, E., et al. (2008), North Pacific Gyre Oscillation links ocean climate and ecosystem change, *Geophys Res Lett*, 35(8).

Yu, B., and F. W. Zwiers, 2007: The impact of combined ENSO and PDO on the PNA climate: A 1,000-year climate modeling study. Climate Dyn., 29, 837–851, doi:10.1007/s00382-007-0267-4.

Alexander, M. A., L.Matrosova, C.Penland, J. D.Scott, and Chang, P. Forecasting Pacific SSTs: Linear inverse model predictions of the PDO. *J. Climate*, **21**, 385–402 (2008) doi:https://doi.org/10.1175/2007JCLI1849.1.

Strong, C., and G. Magnusdottir, 2009: The role of tropospheric Rossby wave breaking in the Pacific decadal oscillation. J. Climate, 22, 1819–1833, doi:10.1175/2008JCLI2593.1.

CHAPTER 2. INCREASING COUPLING BETWEEN NPGO AND PDO LEADS TO PROLONGED MARINE HEATWAVES IN THE NORTHEAST PACIFIC

This work is published in Geophysical Research Letters.

Joh, Youngji and Di Lorenzo, E. (2017), Increasing coupling between NPGO and PDO leads to prolonged marine heatwaves in the Northeast Pacific. Geophysical Research Letters, 44: 11,663-11,671. doi: 10.1002/2017GL075930

2.1 Introduction

The 2013/15 marine heatwave of the Northeast Pacific was characterized by the strongest ocean temperature extremes ever recorded in the North Pacific [*Wang et al., 2014; Baxter and Nigam, 2015; Bond et al., 2015; Hartman, 2015; Anderson et al., 2016; Hobday et al., 2016; Peterson et al., 2016*] and by an unusual persistence that spanned the winters of 2013/14 and 2014/15 [*Di Lorenzo and Mantua, 2016*], culminating in one of the strongest El Niño events of the 20th century in the fall/winter of 2015/16. The progression of the event followed distinct spatial and temporal winter patterns in the ocean and atmosphere that closely resemble the two dominant modes of variability of sea surface temperature and sea level pressure anomalies (SSTa, SLPa). Specifically, the spatial structures of the January-February-March (JFM) SSTa in 2013/14 and 2014/15 are captured by the 2nd and 1st principal components of the North Pacific SSTa [Di Lorenzo and Mantua, 2016] (Figure S2.1). In the Northeast Pacific, these modes are commonly referred to as the North Pacific Gyre Oscillation (NPGO) [*Di Lorenzo et al., 2008*] and the Pacific

Decadal Oscillation (PDO) [*Mantua et al., 1997*] (Figure S2.1). The similarity between the marine heatwave patterns and the mode of Pacific decadal variability suggests that the statistics and persistence of these ocean extremes are linked to the dynamics underlying the North Pacific modes.

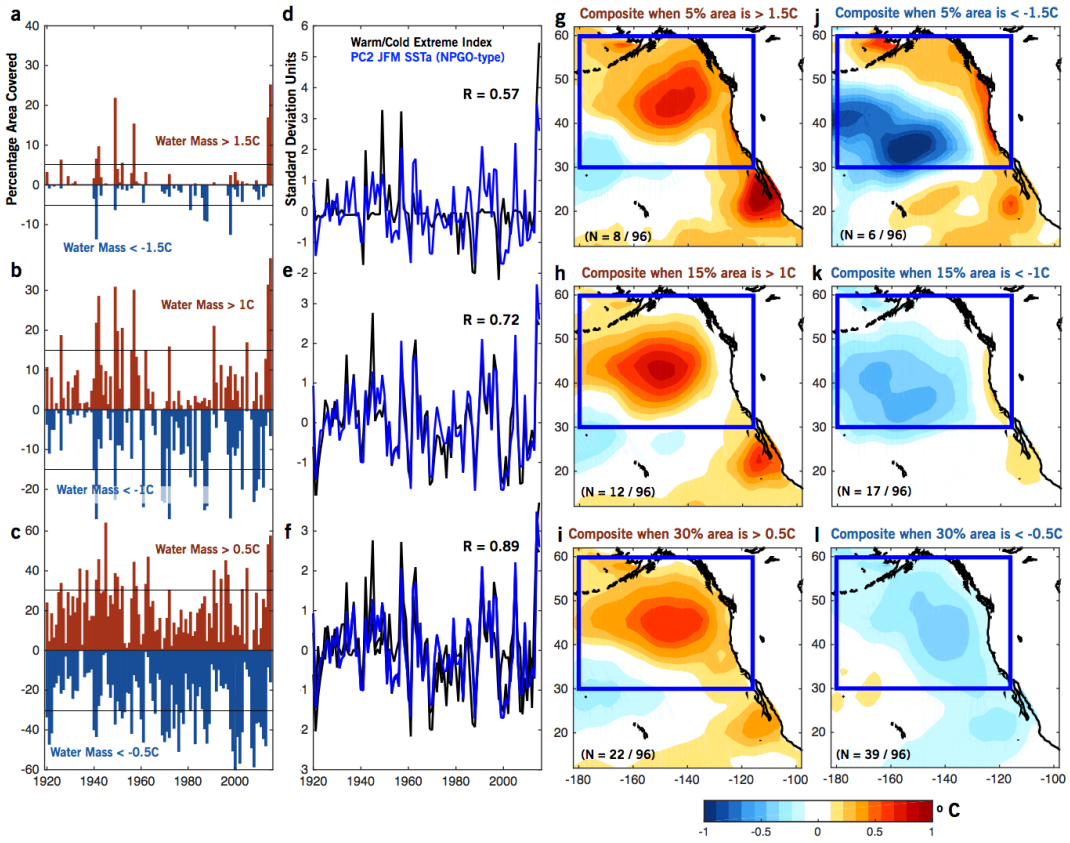

Figure 2.1. Characteristics of winter ocean temperature extremes in the Northeast Pacific. Percentage of the grid points with anomalously warm (red bars) and cold (blue bars) SSTa of the Northeast Pacific where the JFM SSTa are above the threshold values of 1.5°C (a), 1°C (b) and 0.5°C (c). Corresponding ocean extreme index (OEI) (black) vs. PC2 (blue) of JFM SSTa where R is a correlation coefficient between the OEI and PC2 (d-f). Composite of JFM SSTa (°C) when the percentage surface areas covered by anomalously warm/cold water with threshold of 1.5°C, 1°C and 0.5°C exceeds 5% (g/j), 15% (h/k), and 30% (i/l) respectively. Blue box denotes a region used to compute percentage of grid and EOF analysis. Values in parenthesis are the number of events.

Using historical reanalysis products and a climate model ensemble, this study provides a diagnostic of ocean extremes statistics in past observations and in future model projections under the radiative forcing scenario RCP8.5. The goal of this study is to (1) confirm the hypothesis that prolonged ocean extremes events follow recurrent patterns with a transition from a winter NPGO-like pattern to PDO-like pattern in the following winter, and (2) examine how the coupling between these modes via tropical/extra-tropical teleconnections is changing under a warmer climate favoring more prolonged winter to winter warm events.

2.2 Data and Methods

Observations used for investigating the ocean temperature extremes are monthly mean SST data [2° X2° horizontal grid] of the National Oceanic and Atmospheric Administration Extended Reconstruction SST, version 3 (ERSST.v3) product [Smith and Reynolds, 2004] and the Hadley Centre Sea Ice and Sea Surface Temperature (HadiSST) data set [*Rayner et al., 2003*]. For winter extremes, January-February-March [JFM] mean SSTa over the Northeast Pacific (20°N-60°N, 170°E-110°E) are used. Anomalies for SST are constructed by removing the mean monthly climatology and linear trend at each grid point. The limited period between 1920 and 2015 is analyzed.

Given that the North Pacific multi-year marine heatwave of 2014/15 developed initially as a large surface area with anomalously warm SST spanning most of the Northeast Pacific (e.g., the blob), we develop an ocean extreme index (OEI) that is designed to track the occurrence of ocean temperature extremes that cover large areas of the Northeast Pacific [180E-115E and 30N-60N] (blue box of Figure 2.1). For a given winter (JFM), we measure the surface area of anomalously warm and cold SSTa that exceed selected

thresholds values (1.5°C, 1°C and 0.5°C), where 0.5°C is the average of standard deviations of SST at all the grid points in Northeast Pacific between 1920 to 2015 (Figure 2.1a-c). The red and blue bars indicate the warm and cold water area respectively. The OEI is then defined by taking the difference of warm minus cold percentage area (black line in Figures 2.1d-e), so that a large positive OEI indicates a winter when most of the Northeast Pacific is covered by surface area with warm SSTa exceeding the selected threshold.

To examine changes in the statistics of ocean temperature extremes under greenhouse forcing, we use the output of the first 30-members of the CESM-LENS from 1920-2100 under the RCP8.5 greenhouse radiative forcing scenario available at https://www2.cesm.ucar.edu/models/experiments/LENS39 [*Kay et al., 2015*]. Each ensemble member is forced with historical radiative fluxes for the period 1920-2005 and with the RCP8.5 radiative forcing for the period 2005-2100. The CESM-LENS uses a 1-degree latitude/longitude version of CESM1(CAM5). Prior to analyzing the CESM-LENS data, we remove the warming trends by removing the ensemble mean SST timeseries at each grid point. This approach to removing the warming trend leads to almost the same results as removing a quadratic trend at each grid point (Figure S2.6).

In both the observational and model data, we define the first two Empirical Orthogonal Functions (EOFs: computed over the region outlined by the blue box in Figures 2.1g-l, the principal components (PC1 and PC2) are then regressed on Northeast Pacific JFM SSTa) as a proxy of the PDO (PC1) and NPGO (PC2) type variability. These modes track closely the spatial and temporal evolution of the record-breaking warm anomalies patterns of JFM 2014 (EOF2) and JFM 2015 (EOF1) [*Di Lorenzo and Mantua, 2016*].

2.3. Observed and predicted statistics of ocean temperature extremes

To examine the relationship between the modes of the JFM SSTa of the Northeast Pacific (NEP) and the emergence/evolution of marine heatwaves like the 2014/15, we use the historical reanalyses of SSTa from NOAA ERSSTv3 and HadiSST. Rather than inspecting the statistics of a priori specific SSTa patterns in the data (e.g., PC1 and PC2), we use the OEI to objectively identify the years of emergence of ocean extremes that cover most of the NEP waters like in the winter of 2014 – the initiation of the marine heatwave. Inspection of the OEI winter timeseries (Figures 2.1d-f) shows that 2013/14 and 2014/15 SSTa emerge as record-breaking warm temperature events independent of the threshold selected in the analysis. A correlation analysis of the OEIs with the dominant modes of NEP JFM SSTa (Figures 2.1d-f) confirms a significant correlation (> 99% significance, see Methods) with PC2 (e.g., NPGO-like variability) rather than PC1 (e.g., PDO-like). Although this result may be expected, given that the NPGO pattern is characterized by a monopole structure in the NEP, it confirms that we can explore the dynamics of the extreme events in the context of the North Pacific modes (e.g., NPGO, PDO). In fact, a correlation of the OEIs with the PC1 (e.g., PDO-like variability) reveals no significant correlations.

To more clearly reveal the spatial patterns associated with these temperature extremes, we perform a composite analysis of winter SSTa when the percent area covered by warm/cold water (Figures 2.1a-c) is above the thresholds values of 5%, 15% and 30%, respectively (Figures 2.1g-l). In all threshold cases, warm composites exhibit a large open-ocean anomaly in the eastern and central North Pacific resembling the PC2 or NPGO-type expression (Figures 2.1g-i), confirming the temporal relationship found between the OEI and the PC2 timeseries. In contrast, the spatial structures of cold composites demonstrate a more variable pattern that captures both the NPGO and PDO signatures (Figures 2.1j-l).

For example, the large amplitude cold events (Figure 2.1j) exhibit a spatial pattern similar to the PDO expression, with negative SSTa in the central Pacific and positive SSTa along west coast of North America. This suggest that warm/cold temperature extremes in the NEP are not symmetric in space and follow different expressions of the dominant modes of the North Pacific decadal variability.

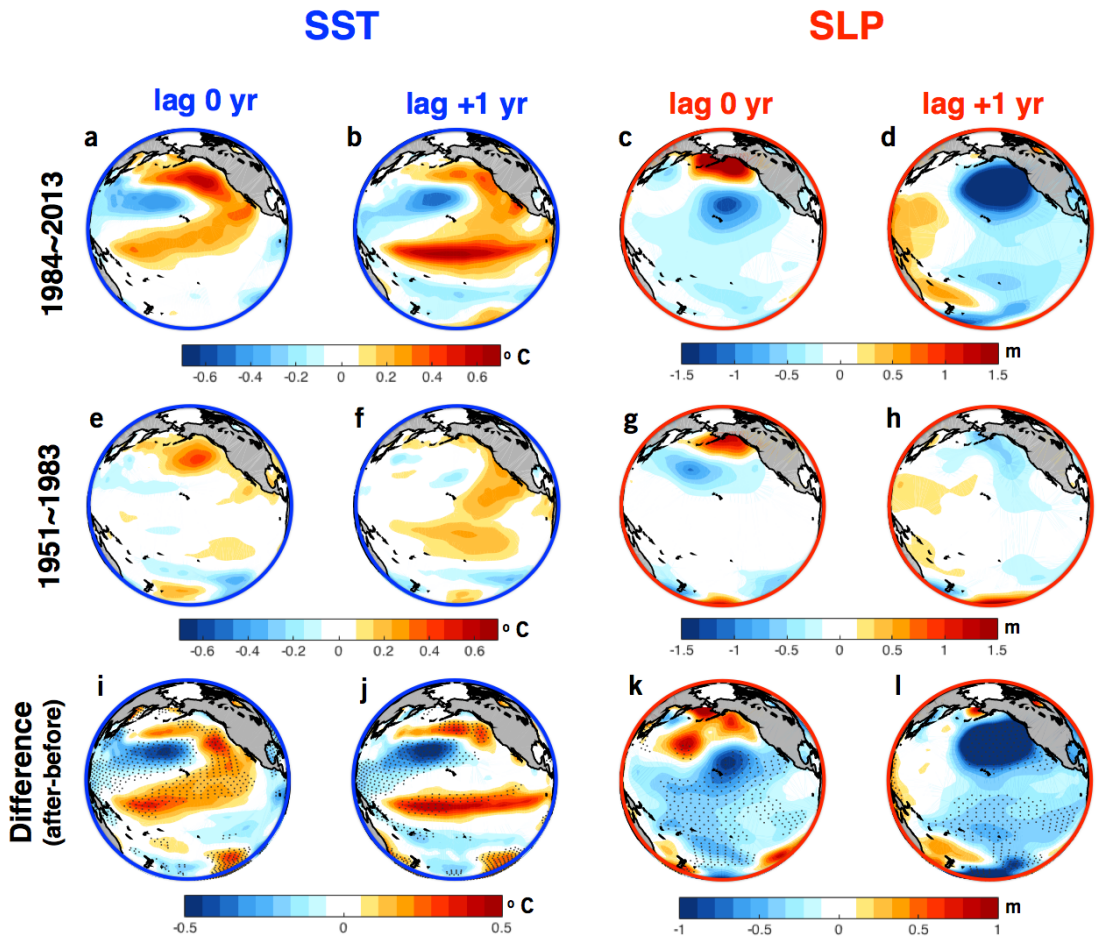

Figure 2.2. Evolution of observed NEP warm temperature events and related atmospheric forcing. Regression maps of OEI (of 1°C to SSTa and SLPa with 0 and +1 year lag during the period of 1984-2013 (a-d), 1951-1983 (e-h). Difference maps between the two periods (recent-previous) (i-l). Stippling indicates regions where the difference of two regression coefficients is statistically significant above the 90% confidence level as determined by a two-tailed Student's t test.

A similar analysis of the OEI is performed on the 30-members of CESM-LENS from 1920-2100 forced with the RCP8.5 scenario (see Methods) to explore how robust the characteristics of temperature extremes are in the NEP compared to observations, and how they respond to anthropogenic forcing. Prior to the analysis we subtract the ensemble mean SSTa timeseries at each grid point to remove the warming trend "forced" signal, which would bias the statistics of warm/cold events (Figure S2.6). The model data is divided into the period of 1951-2000 (hereinafter referred to as the historical simulation) and the period of 2051-2100 (hereinafter referred to as RCP8.5). An inspection of the probability density function (PDF) of the historical and RCP8.5 SSTa over the NEP exhibits overall Gaussian distributions (Figures S2.2a and S2.2b). However, a difference of the RCP8.5 minus historical PDF shows a right skewed SSTa distribution in the RCP8.5 indicating an increased (decreased) frequency of warm (cold) temperature anomalies (Figure S2.2c). This indicates some degree of non Gaussian behavior in the response of the NEP to anthropogenic forcing, which is likely associated with the lack of spatial symmetry in the patterns of the warm and cold composites found in both the observations (Figure S2.1) and in the CESM-LENS (Figures S2.3 and S2.4, as discussed below).

Similar to the treatment of the reanalysis products (e.g., Figure S2.1), we compute warm/cold composites for SSTa thresholds of 0.5°C, 1°C, 1.5°C, and also 2°C to account for the larger number of occurrences of high amplitude events found in the CESM ensemble (e.g., more realizations increase the number of larger extremes counted in the composite, see Figures S2.3 and S2.4). Consistent with the observations, both the historical and RCP8.5 warm composites show a preferred monopole pattern resembling the NPGO-like expression while the cold composites exhibit the hybrid of NPGO-like and PDO-like signatures (Figures S2.3 and S2.4). An analysis of the difference in maximum amplitude

in the RCP8.5 minus historical composites (Figure S2.2d) reveals that warm events intensify between 0.3-0.5 °C and the percentage area covered by surface area with anomalously warm water becomes significantly larger by ~18% (> 99% significance) across the different thresholds (Figure S2.2f). In the frequency statistics, warm events tend to occur slightly more often in the RCP8.5 simulations by ~6% (>99% significance) for 1 °C and by ~3% (>95% significance) for 1.5 °C cases (Figure S2.2h). In contrast, differences in cold composites between historical and RCP8.5 show no significant change in the statistics of amplitude or frequency (Figures S2.2e and S2.2i) except for the spatial coverage (Figure S2.2g).

2.4. Trends of coupling between the dominant modes of North Pacific decadal variability

A distinguishing characteristic of the 2014/15 NEP marine heatwaves is the multi-year winter to winter prolonged nature of the event [*Di Lorenzo and Mantua, 2016*] associated with the transition from an NPGO- (2014) to a PDO-like (2015) SSTa expression (Figure S2.1). We refer to this "prolonged nature" of the event as "persistence" of the warm anomalies, although the spatial pattern is changing as the anomalies transition from an NPGO to PDO type pattern. This transition is enabled by a two-way coupling between the North Pacific and tropics. Specifically, the NPGO-like winter SSTa pattern in the sub-tropics activates well-known El Niño precursors dynamics in the spring that energize the growth of El Niño-like tropical SSTa in summer and fall [e.g., *Vimont et al., 2003; Anderson et al., 2013*]. These tropical SSTa activate teleconnections to the extra-tropic that project onto, and amplify, the PDO-type pattern in the following winter [e.g., *Alexander, 1992*]. These

extra-tropical to tropical teleconnections are a key and dynamically robust mechanism for adding memory and sustaining decadal variance in the Pacific [*Di Lorenzo et al., 2015; Di Lorenzo and Mantua, 2016*].

To explore how the statistics of winter to winter persistence change over time in the observational record, we use regression maps of the OEI (1 ℃ threshold case) with concurrent and +1-year lag observed SSTa and SLPa evaluated over the periods 1984-2013 and 1951-1983 (Figure 2.2). In the analysis, we exclude the JFM 2014 and 2015 events so that the statistics are not dominated by the recent large extremes (e.g., the 2014/15 NEP marine heatwave). The patterns of SSTa and SLPa at lag 0 and +1 year show significant spatial differences. At lag 0 we find the NPGO-like SSTa expression (Figure 2.2a) and a strong SLPa dipole structure resembling the North Pacific Oscillation (NPO) (Figure 2.2c). [*Linkin and Nigam, 2008; Chhak et al., 2009*]. At lag year+1 the PDO-like coastal signature appears along with the El Niño-like pattern in the tropics (Figure 2.2b). The SLPa also changes to the typical signature of a deepening and shift of the Aleutian Low (Figure 2.2d). This progression of warm anomaly patterns is consistent with the previous findings related to the 2014/15 NEP heatwave [*Di Lorenzo and Mantua, 2016*]. By comparing the two periods 1984-2013 (Figure 2.2, top row) and 1951-1983 (Figure 2.2, middle row), we find that the multi-year persistence of warm events is more intense in the recent period (Figure 2.2, bottom row). The atmospheric forcing patterns of the NPO and Aleutian Low become stronger (Figures 2c and d) and the tropical footprint of the SSTa (Figures 2.2a and 2.2b) more intense. This suggests an increase in persistence associated with stronger tropical/extra-tropical coupling. More specifically for the recent period 1984-2013, the development of the first winter warm anomalies have a strong sub-tropical footprint typical of El Niño SSTa and SLPa precursor [e.g., Figure 2.2a, optimal growth pattern, *Penland*

and Sardeshmuch, 1995; Figure 2.2c, seasonal footprinting, *Vimont et al. 2003*]. Consistent with these precursor dynamics, the following winter is characterized by a strong El Niño and PDO signatures in the SSTa (Figure 2.2b) and a more intense Aleutian Low (Figure 2.2d).

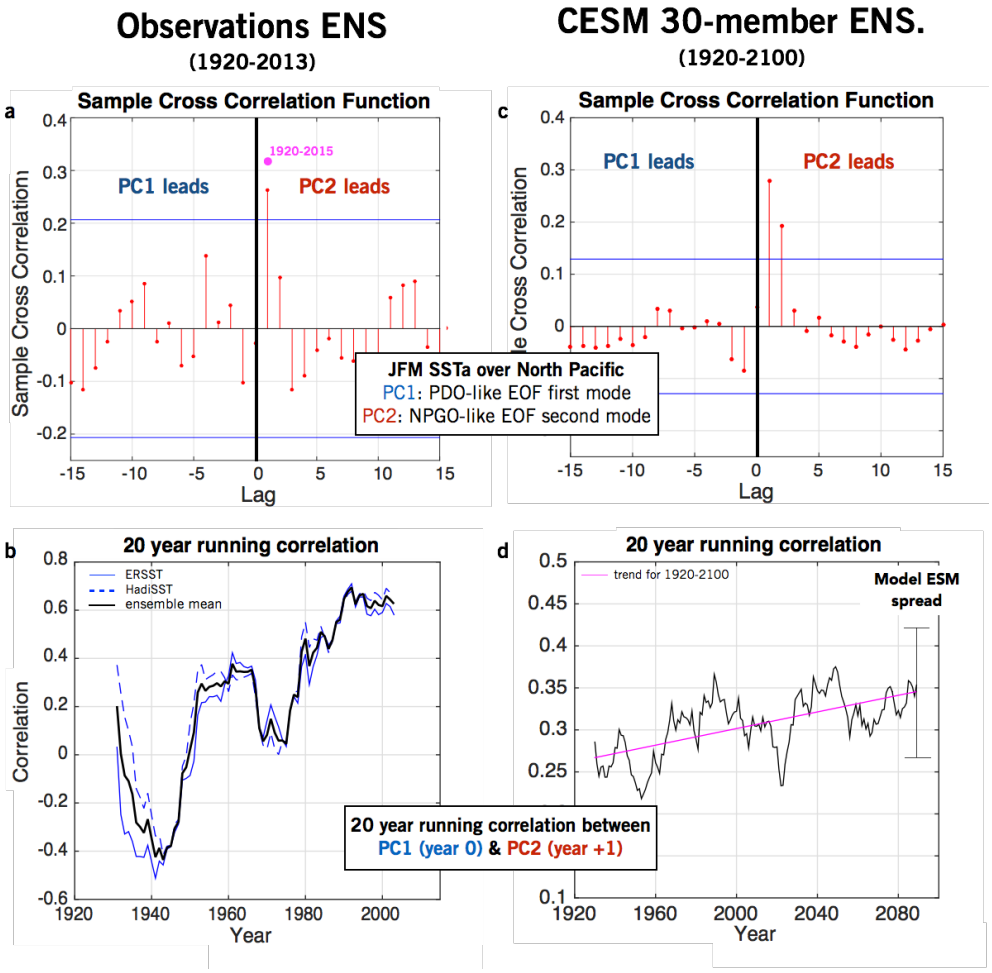

Figure 2.3. Joint statistics of the two Principal Components of NEP JFM SSTa in the observation ensemble and in the CESM-LENS 30-member ensemble. (a) Cross-correlation function of observations (ERSST and HadiSST) between observed PC1 and PC2 with a peak (R=0.27, > 95% significance) when the PC2 (NPGO-type) leads PC1 (PDO-type) by 1 year. The pink dot indicates a peak (R=0.32, > 99% significance) when computing the same analysis using the period of 1920-2015. (b) 1-year lead relationship between observed PC2 with PC1 as a sliding 20-year correlation in the ERSSTv3 (blue line), HadiSST (blue dash line) and their ensemeble mean (black line). (c) Cross-correlation function of CESM-LENS ensemble mean between PC1 and PC2 with a peak (R=0.28, > 95% significance) when the PC2 leads PC1 by 1 year. (d) Sliding 20-year correlation of ensemble mean of 1-year

lead relationship between PC2 with PC1 with the model spread denoted as a gray bar. The pink line indicates a linear trend of 20-year running correlations in the period of 1920-2100 showing the slope of 0.08 with 94% confidence. The significance associated with lag-1 cross-correlation of 30-member CESM having a positive relationship between PC2 and PC1 is tested using a Montecarlo approach (Figure S2.7).

The trend in persistence of marine heatwaves in the NEP is quantified statistically by estimating the winter to winter lag correlation between NPGO- (year 0) and PDO-like (year +1) expressions. The overall cross-correlation function between observed PC1 (PDO-type) and PC2 (NPGO-type) of JFM SSTa (Figure 2.3a) exhibits a maximum of R=0.27 (99% significance level) when PC2 leads PC1 by 1 year. When computing a sliding 20-year of the 1-year lead correlation coefficient between PC2 and PC1 over the period 1950-2013 (Figure 2.3b) we find a significant positive trend (>95% significance) with correlation reaching R=0.6 over the last 30 years (the 2014/15 events were excluded as outliers because of their large size). This increase in correlation is evident in both the NOAA ERSSTv3 and HadiSST reanalysis, and suggests a strong increase in the multi-year winter persistence of the North Pacific SSTa associated to recurrent patterns of decadal variability, namely the NPGO (year 0) and PDO (year +1) type. An interesting aspect of this sliding correlation analysis are the negative values prior to 1950 (Figure 2.3b). While these values could be attributed to noise (e.g., significant correlations on periods of 20 years need to exceed R=0.4), they may also suggest that the observed state contains a wider range of coupling dynamics between winter to winter SSTa than can lead to a negative coupling between PC2 (year 0) and PC1 (year +1). However, further analysis of the CESM-LENS (Figure S2.7d, discussed in the next section), show that negative lag 1-year correlations never occur between PC2/PC1 in any of the ensemble members over the entire length of the simulations 1920-2100. This indicates that the lead-lag dynamics between the two

dominant modes are very robust in the CESM-LENS, and may suggest that the observational SSTa prior to 1950 may be inadequate (e.g., because of the under sampling) to fully resolve this type of variability.

To understand the significance of the increase in coupling and persistence of North Pacific SSTa in the context of climate change, we now examine the statistics of consecutive multi-year warm events in the CESM-LENS Historical (1951-2000) and RCP8.5 (2051-2100) simulations (Figure 2.4). We use the OEI (1 ℃ threshold case) extracted for each ensemble member to construct the concurrent and the +1-year lag regression maps in SSTa and SLPa. Similar to the observational findings (Figure 2), both the Historical and RCP8.5 simulations show that the warm events of the NEP originate as an NPGO-like pattern in the SSTa (Figures 2.4a and 2.4e) and evolve to a PDO-like expression accompanying El Niño (Figures 4b and f, at lags of 1 year). The correspondence with observations is particularly remarkable if we compare the recent observed period 1984-2013 (Figures 2.2a and 2.b) with the simulations for 2015-2100 using the RCP8.5 radiative forcings (Figures 2.4a and 2.4b). To better isolate the projected trends for future climate in the CESM-LENS we examine the difference maps RCP8.5 minus Historical. Consistent with the recent observational trends, the difference maps at 0 year lag reveal a stronger SSTa in the North Pacific with an equatorward sub-tropical intensification of the warm anomalies (compare Figure 2.2i vs. Figure 2.4i) followed at 1 year lag by a clear strengthening of the El Niño signature along the equator (compare Figure 2.2j vs. Figure 2.4j). Inspection of the SLPa difference maps in both observations and CESM-LENS (Figures 2.2k and 2.2l; Figures 2.4k and 2.4l) confirms that the SSTa trends are connected to a more prominent expression of the southern lobe of the NPO-like pattern at 0 year lag followed by deeper Aleutian Low at 1 year lag, which in the model is forced by the teleconnections induced by stronger El Niño

SSTa in the tropics (Figure 2.2j and Figure 2.4j). However, in CESM-LENS the strengthening of this teleconnection does not become apparent until the period 2051-2100. In fact, a comparison of regression maps between the two periods (1984-2013 vs. 1951-1983 in Figure S2.8) in CESM-LENS exhibits no significant change. This indicates that the recent changes in the observations (Figure 2.2) cannot be attributed directly to anthropogenic-induced climate change, although they are consistent with the long-term response to anthropogenic warming (e.g., 2051-2100) as by the CESM-LENS.

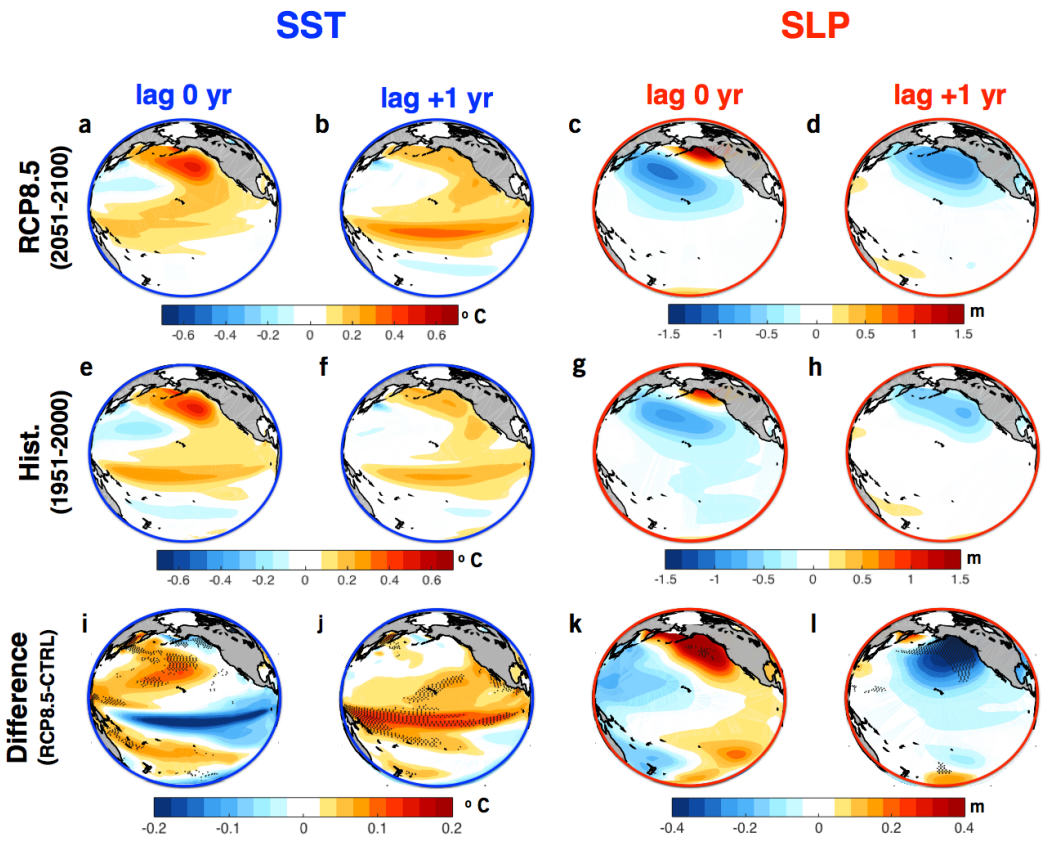

Figure 2.4. Evolution of the NEP warm events and related atmospheric forcing of the CESM-LENS ensemble mean. Regression maps of OEI (of 1°C) to SSTa and SLPa with 0 and +1 year lag for the 50 years of RCP8.5 (a-d) and Historical (e-h) scenario. Difference maps between the RCP8.5 and Historical scenario (RCP8.5-Historical) (i-l). Stippling indicates regions where the difference of two regression coefficients is statistically significant above the 90% confidence level as determined by a two-tailed Student's t test.

The multi-year persistence of North Pacific SSTa in the CESM-LENS is quantified through the multi-member ensemble 1-year lag cross-correlation between PC2 (NPGO-type) and PC1 (PDO-type) (Figure 2.3c). We confirm that the model clearly captures the multi-year persistence of warm anomalies associated with the transition from an NPGO to PDO type patters, with the 1-year lead correlation (PC2 vs. PC1) R=0.28 comparable to the observations R=0.27 (Figure 2.3a). Similar to what is done for the two reanalysis datasets, we compute a sliding 20-year average of the 1-year lead correlation between PC2 and PC1 (Figure 2.3d) in each simulation to quantify the trends in coupling of the multi-year persistence. The CESM-LENS exhibits a positive trend ~35% increase in correlation (from R=0.27 to R=0.35) over the period 1920-2100, with 21 out of 30 simulations showing a positive sign in the trend consistent with observations (Figure 2.3b). The model also shows a large spread around the ensemble mean (gray bar in Figure 2.3d) suggesting that the strong observed trend falls within the statistics of individual model realizations. Finally, we note that every ensemble members exhibits a positive correlation in the 1-year lag coupling between PC2 and PC1, even when considering windows of 20 years (Figure S2.7d). This confirms that the coupling between NPGO and PDO is a very robust dynamical feature of North Pacific climate variability in the CESM simulations.

2.5. Implications for future climate and ecology

Taken together, these analyses suggest that the recent observational trends in the coupling between the NPGO and PDO type patterns associated with the winter to winter persistence of warm anomalies in the NEP are consistent with future projections of climate change as inferred from the CESM-LENS RCP8.5 simulations in 2051-2100. However, a direct attribution of the recent trends to anthropogenic forcing is premature based in the

CESM-LENS simulations, which show that these trends become statistically significant ~2050. The model simulations also suggest that NEP marine heatwaves will become larger in size (~18%) and amplitude (0.3-0.5°C) with the potential of strong and prolonged stresses on marine ecosystems in this region.

The physiological stress from the increasing persistence and magnitude of marine heatwaves might become an important driver altering a marine food-webs in the NEP via range shifts of different species and corresponding shifts in ecosystem community structure [*Munday et al., 2008; Tittensor et al., 2010; Wernberg et al, 2013*]. Widespread and extreme negative impacts on marine life and fisheries associated with the 2014-15 marine heat wave are well-documented. If the projected increases in the area, magnitude and frequency of extreme warm events are realized, and they are superimposed upon a systematic anthropogenic warming trend, this combination would likely cause profound negative impacts on marine life and fisheries all along the west coast of North America, particularly those in the Gulf of Alaska in the 2nd half of the 21st century.

2.6 Supporting Information

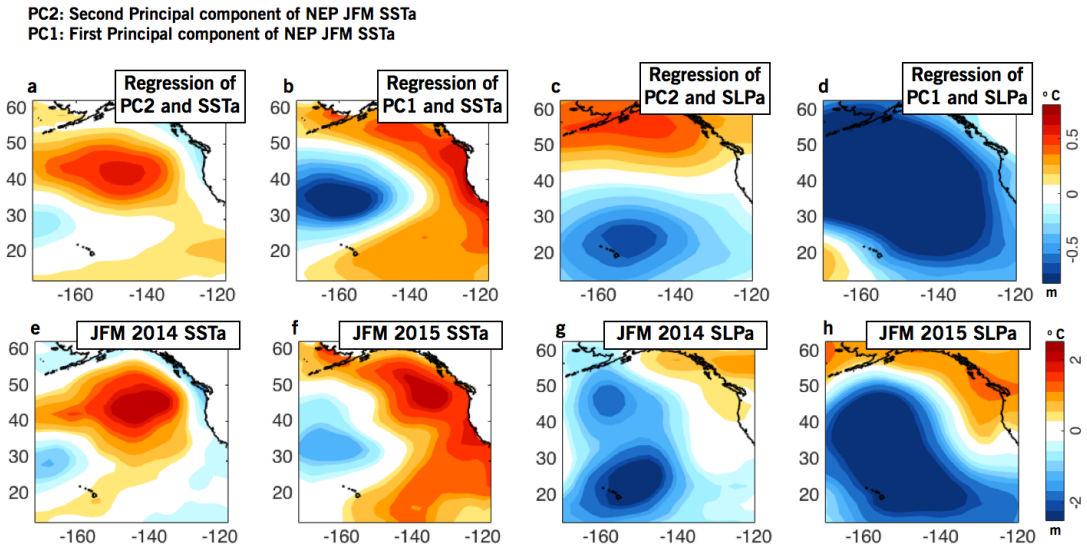

Figure S2.1. Comparison between two dominant modes of North Pacific SST variability and winter (JFM) SSTa/SLPa pattern of 2014 and 2015. Regression maps of JFM SSTa and PC2 (NPGO-type variability) (a) and PC1 (PDO-type variability) (b) of Northeast Pacific JFM SSTa. Regression maps between JFM SLPa and PC2 (c) and PC1 (d). JFM SSTa pattern of 2014 (e) and 2015 (f). JFM SLPa pattern of 2014 (g) and 2015 (h).

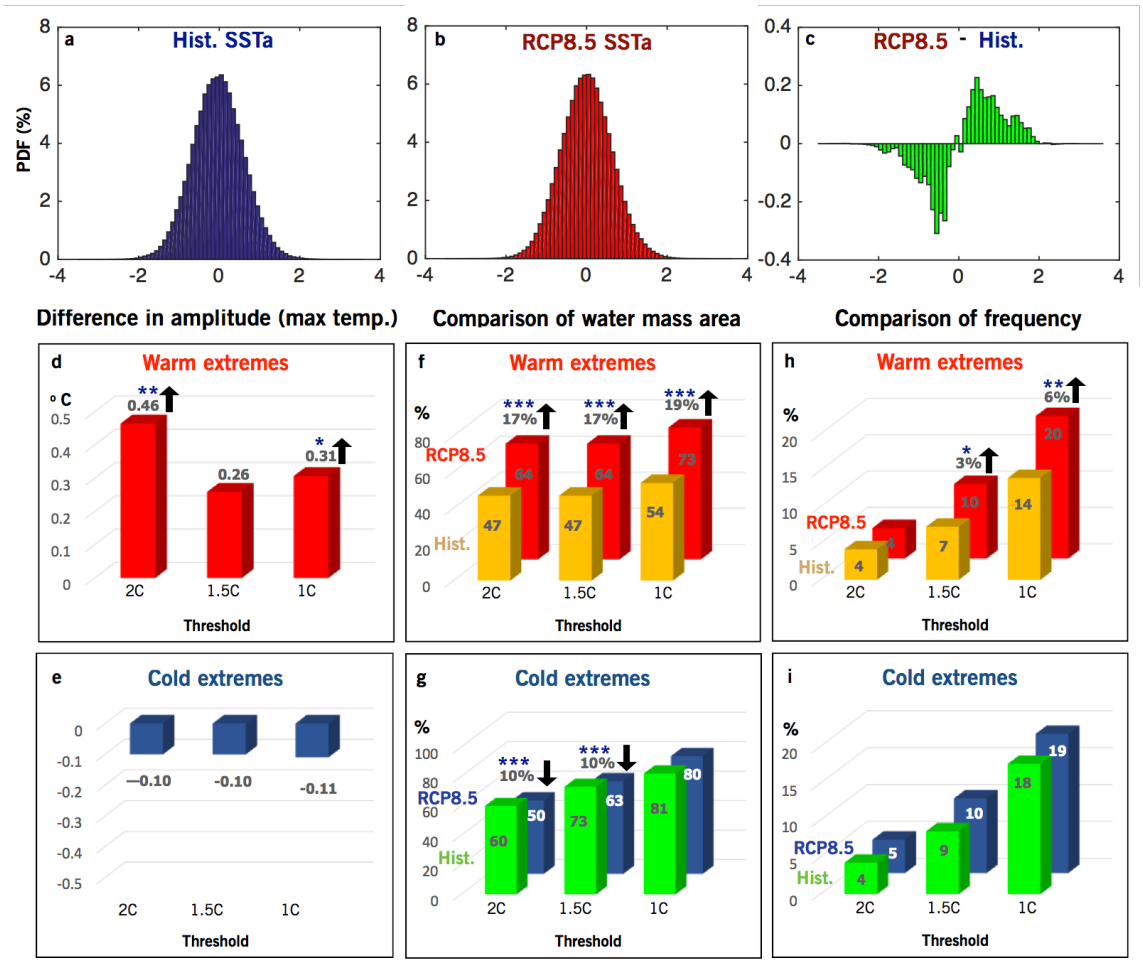

Figure S2.2. Difference in probability density functions (PDFs) of SSTa and amplitude, extreme SSTa area, and occurrence frequency of warm/cold temperature events in the Northeast Pacific between historical and for the 50-year period 2051-2100 of RCP8.5 simulations. PDFs of the historical (a) and RCP8.5 for the Northeast Pacific SSTa (b) and their difference (c). Difference in maximum temperature (°C) of warm (d) and cold (e) anomalies between the historical and RCP8.5 SSTa composites. Comparison of percentage surface area (%) with anomalously warm (f) and cold (g) water mass between the historical and RCP8.5 SSTa composites. Comparison of percentage of the number (%) of composited warm (h) and cold (i) events between the historical and RCP8.5 SSTa composites. Significant values at the 90%, 95%, and 99% confidence levels are marked by different number of asterisks ('*','**' and '***') respectively based on a Montecarlo approach (See supplementary Figure S2.4).

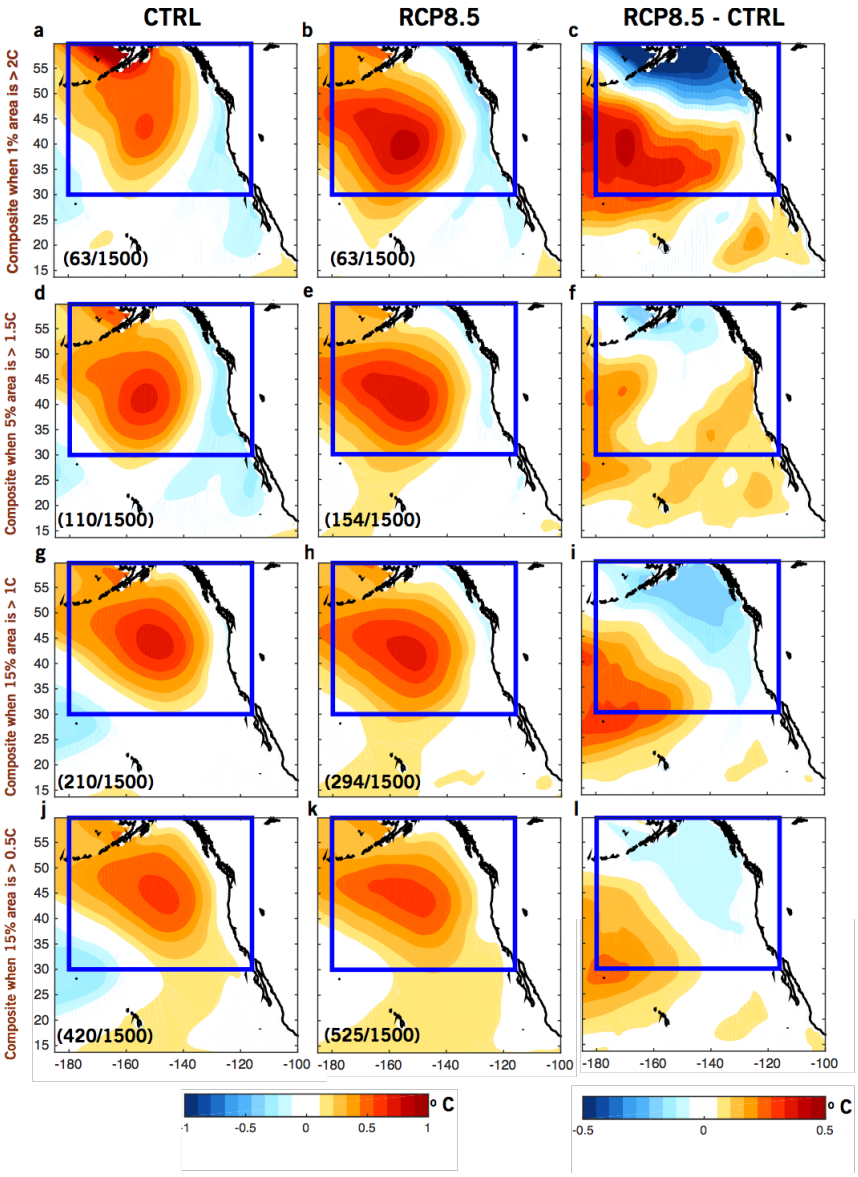

Figure S2.3. Composite of warm SSTa events of historical and RCP8.5 and difference maps between two scenarios. CESM-LENS ensemble mean composite of JFM SSTa (°C) when the percentage areas covered by warm water above the threshold of 2°C (a-c), 1.5°C (d-f), 1°C (g-i), and 0.5°C (j-l) exceed 1%, 5%, 15%, and 30% respectively. The left and middle columns indicate historical and RCP8.5 scenario and the right column shows the difference between two scenarios (RCP8.5- historical). Values in the parenthesis are the number of events used in the multi-model ensemble composite.

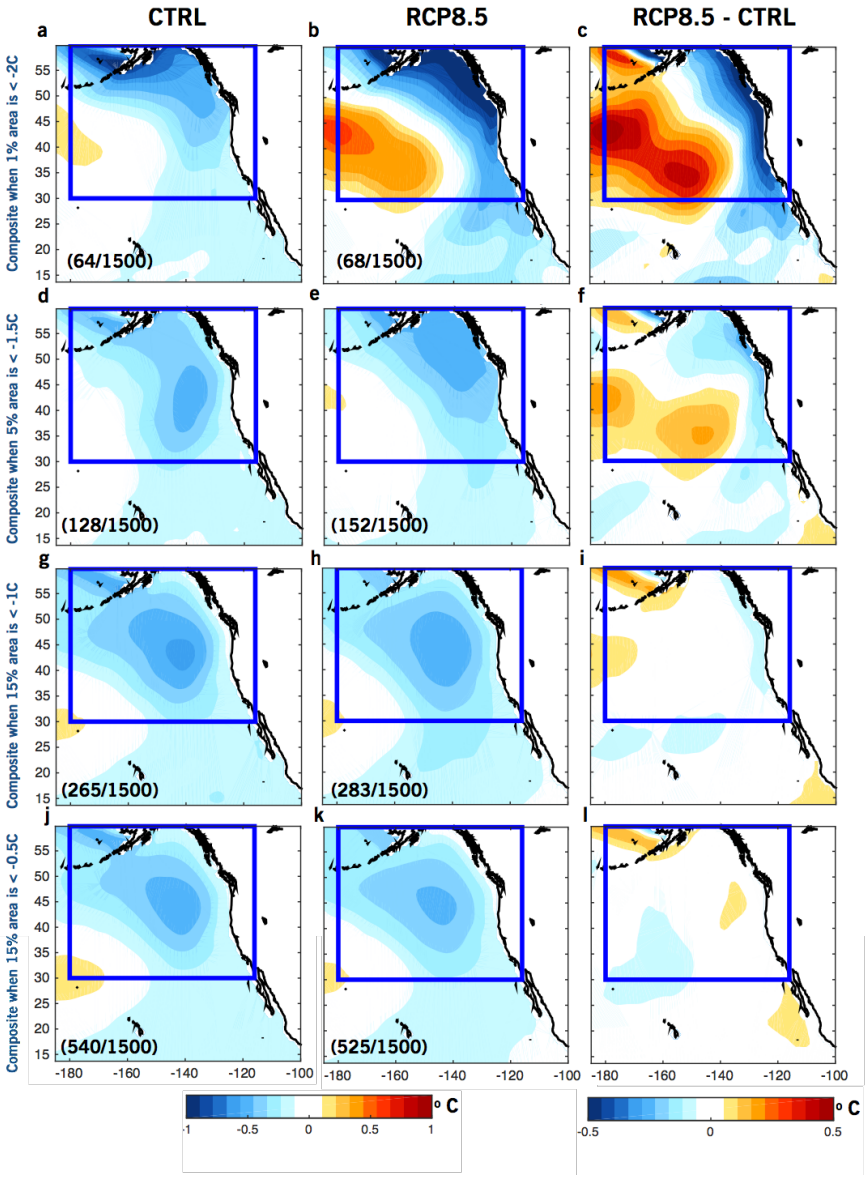

Figure S2.4. Composite of cold SSTa events of historical and RCP8.5 and difference maps between two scenarios. CESM-LENS ensemble mean composite of JFM SSTa (°C) when the percentage areas covered by cold water above the threshold of -2°C (a-c), -1.5°C (d-f), -1°C (g-i), and -0.5°C (g-i) exceed 1%, 5%, 15%, 30% respectively. The left and middle columns indicate historical and RCP8.5 scenario and the right column shows the difference between two scenarios (RCP8.5- historical). Values in parenthesis are the number of events used in the multi-model ensemble composite.

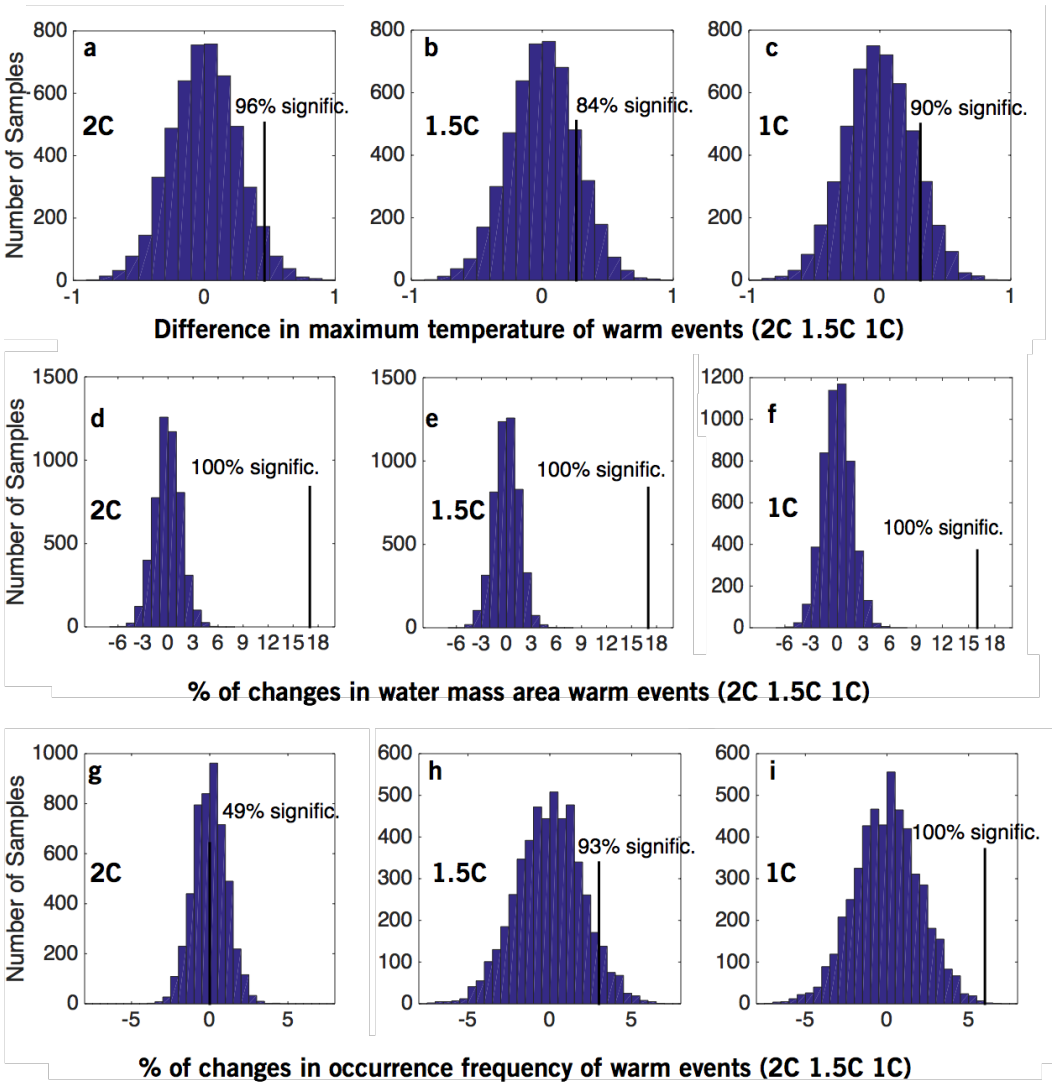

Figure S2.5. Significance test of the difference in (a-c) maximum temperature, (d-f) water mass size and (g-i) frequency of warm events between historical and RCP8.5 shown in Figures S2.2d-f based on Montecarlo approach. (a-c) Distribution of trends of 30-member ensemble mean in difference in maximum temperature between historical and RCP8.5 simulation with a model ensemble mean (black line) value 0.46°C (a), 0.26°C (b) and 0.31°C (c) shown as vertical line at 96 %, 84 % and 90 % significance level respectively. (d-f) Distribution of trends of 30-member ensemble mean in percent changes in water mass area between historical and RCP8.5 simulation with a model ensemble mean (black line) value 0.17 % (a), 0.17 % (b) and 0.18 % (c) shown as vertical line at 100 % significance level. (g-i) Distribution of trends of 30-member ensemble mean in percent changes in occurrence frequency between historical and RCP8.5 simulation with a model ensemble mean (black line) value 0 % (a), 0.3 % (b) and 0.6 % (c) shown as vertical line at 49 %, 93 % and 100 % significance level respectively.

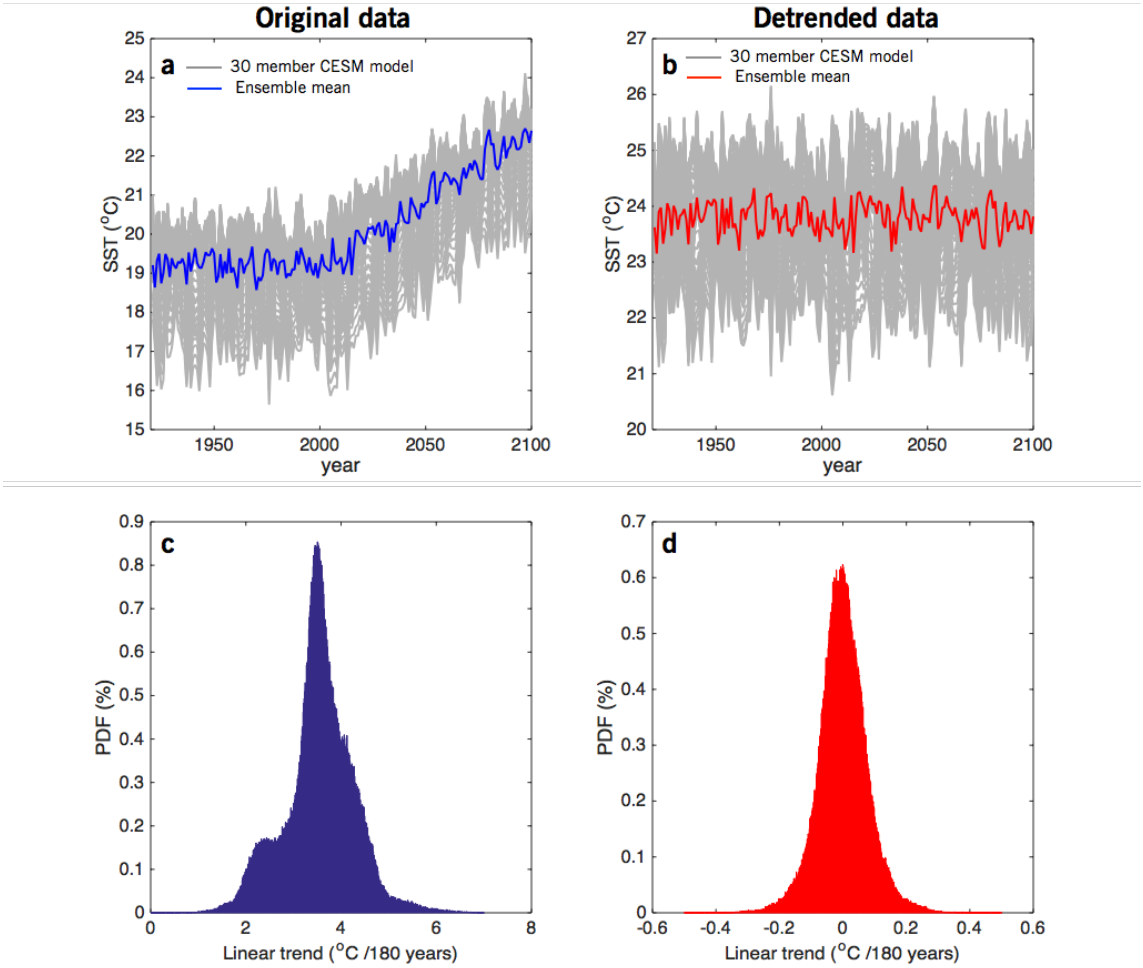

Figure S2.6. Comparison of SST time series (a and b) and PDFs of linear trend (c and d) between original and detrended CESM-LENS data. Original (a) and detrended (b) SST time series of the Northeast Pacific of each CESM-LENS member (gray) and their ensemble mean (blue in Fig. S2.5a and red in Fig. S2.5b) for the periods 1921-2100. Probability of density functions of 180-year trends in the Northeast Pacific SST for the period of 1921-2100 of each CESM-LENS member in the original (c) and detrended (d) model data.

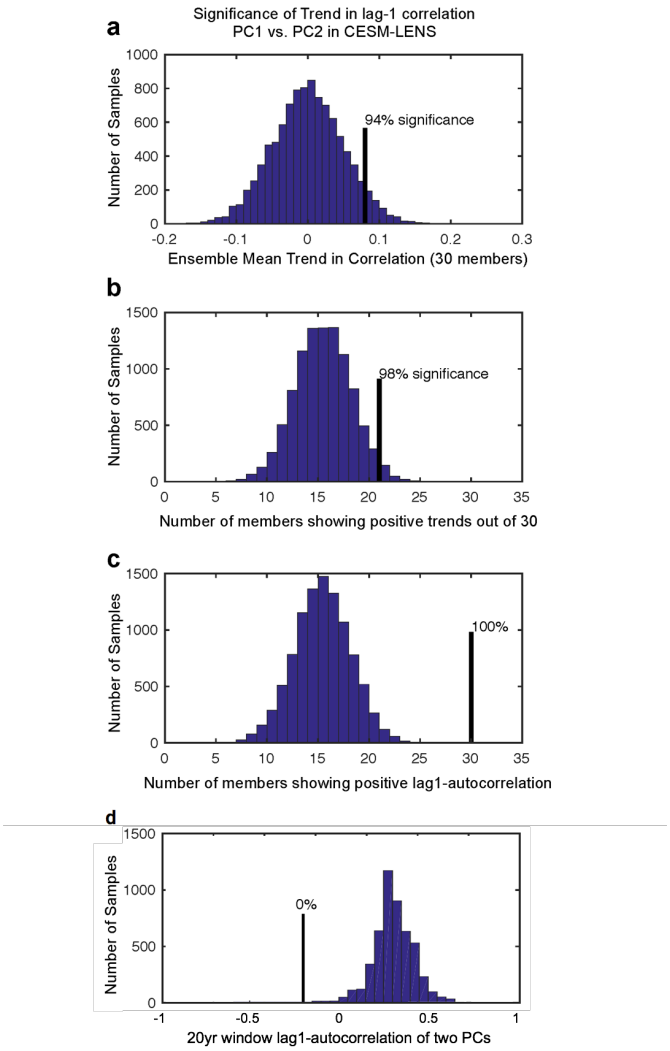

Figure S2.7. Significance test of the CESM-LENS ensemble correlations between PC1 (JFM+1) and PC2 (JFM) shown in Figure 4d based on a Montecarlo approach (N=5000 with an ensemble of 30 random noise pairs of timeseries with the same characteristics of PC1 and PC2 (e.g., same autocorrelation). (a) Distribution of trends of 30-member ensemble mean in lag-1 correlation for the 180 years with a model ensemble mean (black line) value ~0.08 shown as vertical line at 94% significance level. (b) Distribution of number of members showing positive trends out of 30 members for the period of 180 years with the number (21/30) of them found in the CESM-LENS shown as vertical line at 98% significance level. (c) Distribution of number of members showing positive lag 1-autocorrelation out of 30 members for the period of 180 years which shows the relationship between PC2 (JFM) and PC (JFM+1) is a very robust mechanism in the model and significant at the 100% level. (d) Distribution of number of members showing positive lag 1-autocorrelation using a 20-year window out of 30 members with the period of 180 years which shows there is no chance that relationship between PC2 (JFM) and PC (JFM+1) is negative in the CESM-LENS 30-member.

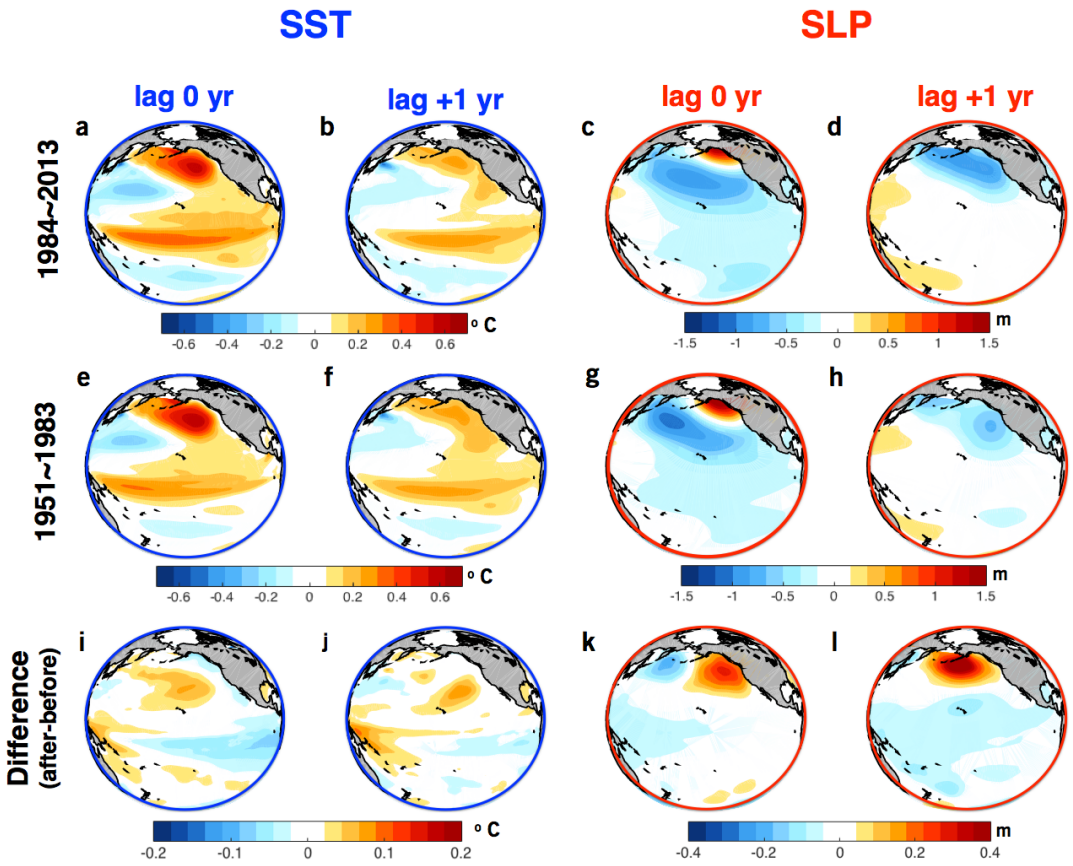

Figure S2.8. Evolution of the Northeast Pacific warm events and related atmospheric forcing of the CESM-LENS ensemble mean. Regression maps of OEI (of 1℃) to SSTa and SLPa with 0 and +1 year lag for the period of 1984-2013 (a-d) and 1951-1983 (e-h) scenario. Difference maps between two periods (1984-2013 minus 1951-1983) (i-l).

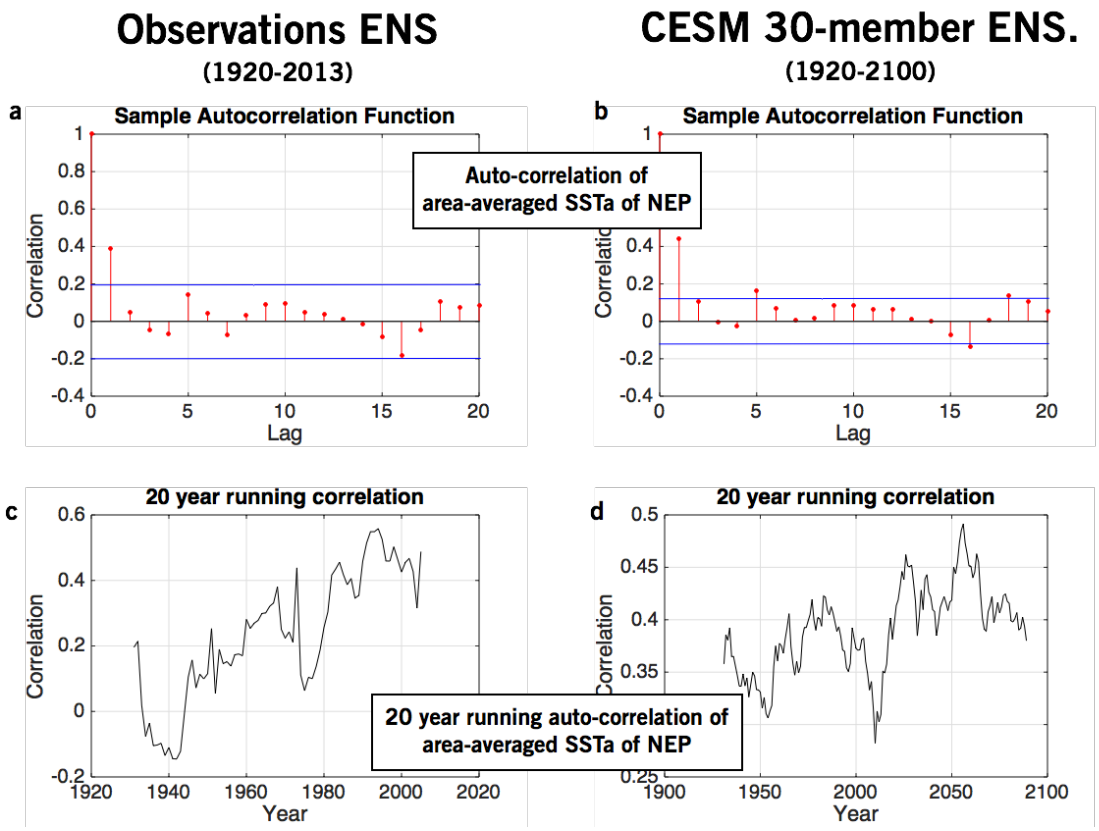

Figure S2.9. Multi-year persistence of marine heatwaves in the Northeast Pacific. Auto-correlation of an area-averaged SSTa index for the Northeast Pacific region for the observation (a) and CESM-LENS ensemble (b). 20 year running 1-year lag auto-correlation of area-averaged SSTa index for the Northeast Pacific of observation (c) and CESM-LENS ensemble (d).

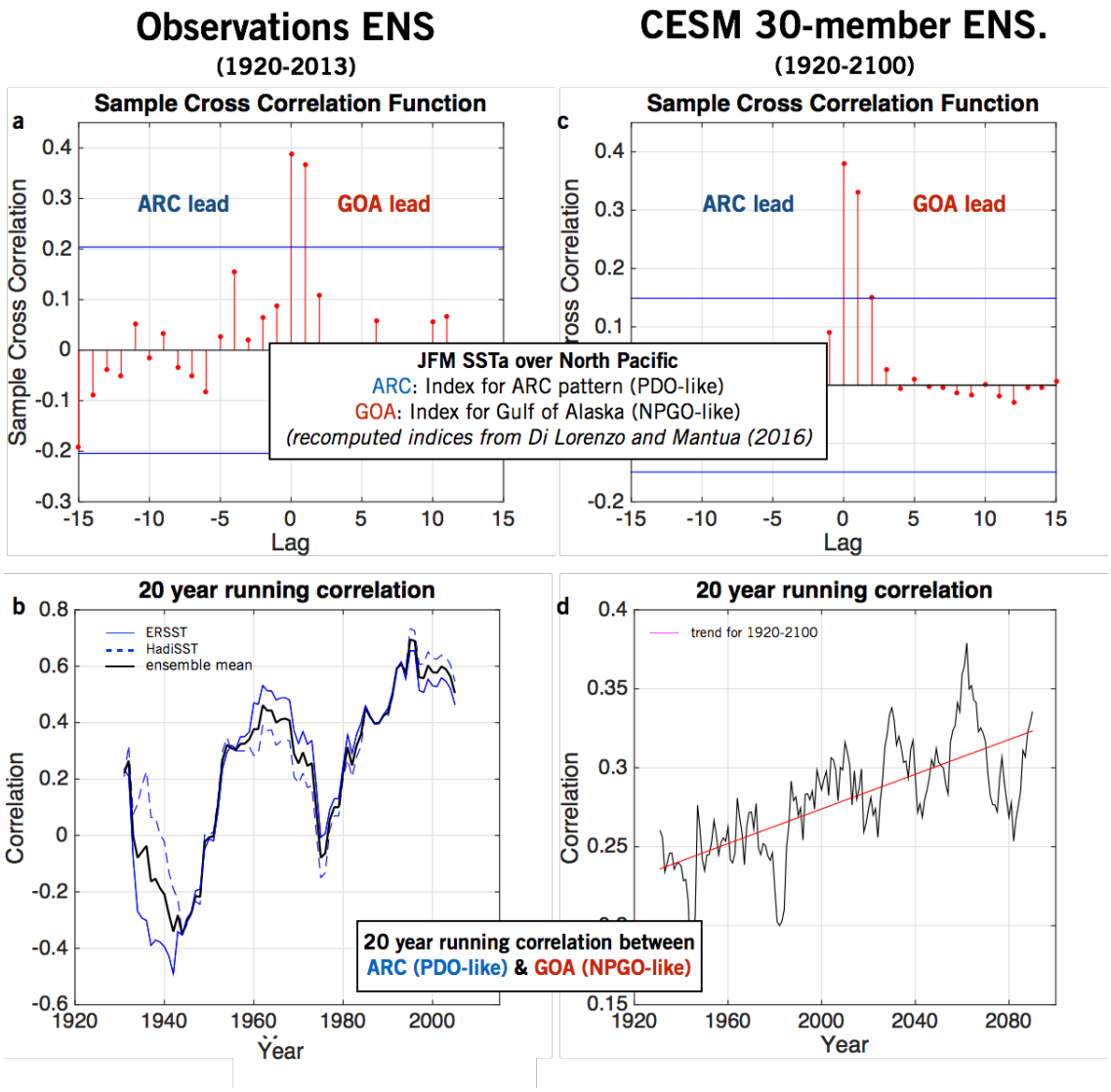

Figure S2.10. As in Figure 2.3, but for the different indices associated with the Gulf of Alaska (GOA) and ARC pattern suggested from *Di Lorenzo and Mantua (2016)*. Both the GOA and ARC SST indices are measured by taking the average SSTa in the regions of the Gulf of Alaska and along the Pacific North American boundary referred to as the 'ARC' as in *Di Lorenzo and Mantua (2016)*.

2.7 References

Alexander, M. A. (1992), Midlatitude atmosphere ocean interaction during El Nino. 1. The North Pacific-Ocean, *J. Clim.*, 5(9), 944-958, doi:10.1175/1520-0442(1992)005<0944:maiden>2.0.co;2.

Anderson, B. T., D. J. Gianotti, J.C. Furtado, and E. Di Lorenzo (2016), A decadal 326 precession of atmospheric pressures over the North Pacific. *Geophys. Res. Lett.*, DOI: 327 10.1002/2016GL068206

Anderson, B. T., R. C. Perez, and A. Karspeck (2013), Triggering of El Nino onset through trade wind-induced charging of the equatorial Pacific, Geophysical Research Letters, 40(6), 1212-1216, doi:10.1002/grl.50200

Baxter, S., and S. Nigam (2015), Key Role of the North Pacific Oscillation-West 280 Pacific Pattern in Generating the Extreme 2013/14 North American Winter, *J. Clim.*, 281 28(20), 8109-8117, doi:10.1175/jcli-d-14-00726.1

Bond, N. A., M. F. Cronin, H. Freeland, and N. Mantua (2015), Causes and impacts of the 2014 warm anomaly in the NE Pacific, Geophys. Res. Lett., 42(9), 3414-3420, doi:10.1002/2015gl063306.

Chhak, K. C., E. Di Lorenzo, N. Schneider, and P. F. Cummins (2009), Forcing of 337 Low-Frequency Ocean Variability in the Northeast Pacific, *J. Clim.*, 22(5), 1255-1276, 338 doi:10.1175/2008jcli2639.1.

Di Lorenzo, E., et al. (2008), North Pacific Gyre Oscillation links ocean climate and ecosystem change, *Geophys. Res. Lett.*, 35(8), doi:10.1029/2007gl032838.

Di Lorenzo, E., G. Liguori, N. Schneider, J. C. Furtado, B. T. Anderson, and M. A. Alexander (2015), ENSO and meridional modes: A null hypothesis for Pacific climate variability, *Geophys. Res. Lett.*, 42(21), 9440-9448, doi:10.1002/2015gl066281.

Di Lorenzo, E. and Mantua, N. (2016), Multi-year persistence of the 2014/15 North Pacific marine heatwave. *Nat. Clim. Change*, 6(11) 1042-+, doi:10.1038/nclimate3082.

Hartmann, D. L. (2015), Pacific sea surface temperature and the winter of 2014, *Geophys. Res. Lett.*, 42(6), 1894-1902, doi:10.1002/2015gl063083.

Hobday, A. J., L. V. Alexander, S. E. Perkins, D. A. Smale, S. C. Straub, E. C. J. 299 Oliver, J. Benthuysen, M. T. Burrows, M. G. Donat, M. Feng, N. J. Holbrook, P. J. 300 Moore, H. A. Scannell, A. S. Gupta and T. Wernberg (2016), A hierarchical approach 301 to defining marine heatwaves. *Prog. Oceanog*, 302 doi:10.1016/j.pocean.2015.12.014

Kay, J. E., Deser, C., Phillips, A., Mai, A., Hannay, C., Strand, G., Arblaster, J., Bates, S., Danabasoglu, G., Edwards, J., Holland, M. Kushner, P., Lamarque, J.-F., Lawrence, D., Lindsay, K., Middleton, A., Munoz, E., Neale, R., Oleson, K., Polvani, L., and M. Vertenstein (2015), The Community Earth System Model (CESM) Large Ensemble

Project: A Community Resource for Studying Climate Change in the Presence of Internal Climate Variability, Bulletin of the American Meteorological Society, doi: 10.1175/BAMS-D-13-00255.1, **96**, 1333-1349.

Linkin, M. E. and Nigam, S. (2008), The north pacific oscillation-west Pacific teleconnection pattern: Mature-phase structure and winter impacts, *J. Clim*, 21(9), 1979-1997, doi:10.1175/2007jcli2048.1.

Mantua, N. J., Hare, S. R., Zhang, Y., Wallace, J. M. and Fracis, R. C. A. (1997), Pacific interdecadal climate oscillation with impacts on salmon production, *Bull. Amer. Meteorol. Soc.*, 78(6), 1069-1079, doi:10.1175/1520-0477.

Munday, P. L., Jones, G. P., Pratchett, M. S. and A. J. Williams, Climate change and the future for coral reef fishes, Fish Fisheries 9, 261–285.

Penland, C., and P. D. Sardeshmukh (1995), THE OPTIMAL-GROWTH OF TROPICAL SEA-SURFACE TEMPERATURE ANOMALIES, *Journal of Climate*, *8*(8), 1999-2024, doi:10.1175/1520-0442(1995)008<1999:togots>2.0.co;2.

Peterson, W., Bond, N. and Robert, M. (2016), The Blob (Part Three): Going, going, gone ? PICES Press 24, 46-48 (2016).

Rayner, N.A., Parker, D. E., Horton, E. B., Folland, C. K., Alexander, L. V., Rowell, D. P., Kent, E. C. and Kaplan, A. (2003), Global analyses of sea surface temperature, sea ice, and night marine air temperature since the late nineteenth century, *Geophys. Res. Lett*., 108(14), 4407, doi:10.1029/2002JD002670.

Smith, T.M., R.W. Reynolds, T.C. Peterson, and J. Lawrimore (2008), Improvements NOAAs Historical Merged Land–Ocean Temp Analysis (1880–2006). *J. Clim*., 21, 2283–2296.

Tittensor, D. P., Mora C., Jetz W., Lotze H. K., Ricard D., Berghe E. V. and Worm B. (2010), Global patterns and predictors of marine biodiversity across taxa. *Nat*. 466, 1098–1101.

Vimont, D. J., J. M. Wallace, and D. S. Battisti (2003), The seasonal footprinting mechanism in the Pacific: Implications for ENSO, *J. Clim., 16*(16), 2668-2675, doi:10.1175/1520-0442(2003)016<2668:tsfmit>2.0.co;2.

Wang, S. Y., L. Hipps, R. R. Gillies, and J. H. Yoon (2014), Probable causes of the abnormal ridge accompanying the 2013-2014 California drought: ENSO precursor and anthropogenic warming footprint, *Geophys. Res. Lett*., 41(9), 3220-3226, doi:10.1002/2014gl059748.

Wernberg, T., Smale D. A., Tuya F., Thomsen M. S., Langlois T. J., de Bettigneis T., Bennett S., and Rousseaux C. S. (2013), An extreme climatic event alters marine ecosystem structure in a global biodiversity hotspot. *Nat. Clim. Change* **3**, 78–82

CHAPTER 3. INTERACTIONS BETWEEN KUROSHIO EXTENSION AND CENTRAL TROPICAL PACIFIC LEAD TO PREFERRED DECADAL-TIMESCALE OSCILLATIONS IN PACIFIC CLIMATE

This work is published in Scientific Reports.

Joh, Youngji and Di Lorenzo, E. (2019), Interactions between Kuroshio Extension and Central Tropical Pacific lead to preferred decadal-timescale oscillations in Pacific climate. Scientific Reports, 9: 13558 (2019). https://doi.org/10.1038/s41598-019-49927-y

3.1 Introduction

The North Pacific climate variability is characterized by strong interactions between ocean and atmosphere on a wide range of timescales. Due to significant influences of the North Pacific decadal fluctuations on marine ecosystems [*Francis and Hare, 1994; Mantua et al., 2017; Nakata and Hidaka, 2003; Di Lorenzo et al., 2008; Sydeman and Thompson, 2010; Cloern and Jassby, 2010; Di Lorenzo and Ohman, 2013*], and climate extremes [*Hartman, 2015; Di Lorenzo and Mantua, 2016; Joh and Di Lorenzo, 2017*], examinations of the mechanism generating a preferred decadal peak in the North Pacific climate spectrum are important. Previous studies have suggested that low-frequency variability of the North Pacific is driven by several mechanisms which include remote forcing from the tropical Pacific [*Trenberth et al., 1998; Liu and Alexander, 2007*] and oceanic processes such as anomalous advection acting on the mean thermal gradient [*Qiu, 2000; Vivier et al., 2002; Scott and Qiu, 2003*], the reddening of atmospheric internal variability [*Scott and*

Qiu, 2003; Xue et al., 1995; Seager et al., 2001], the reemergence mechanism [*Chhak et al., 2009; Alexander et al., 1995*], and the westward propagation of long Rossby waves [*Qiu et al., 2007; Andres et al., 2009; Ceballos et al., 2009; Newman et al., 2016*]. Spatially, these mechanisms give rise to a pattern of sea surface temperature (SST) variance that is referred to as the Pacific Decadal Oscillation (PDO) [*Mantua et al., 1997*]. By decomposing the mechanisms and modes that make up the PDO, Newman et al. (2016) reveals that strong quasi-periodic decadal fluctuations of the North Pacific climate are connected to the dynamics of the Kuroshio Extension (KE) region. However, the mechanisms behind a preferred decadal timescale are still being debated.

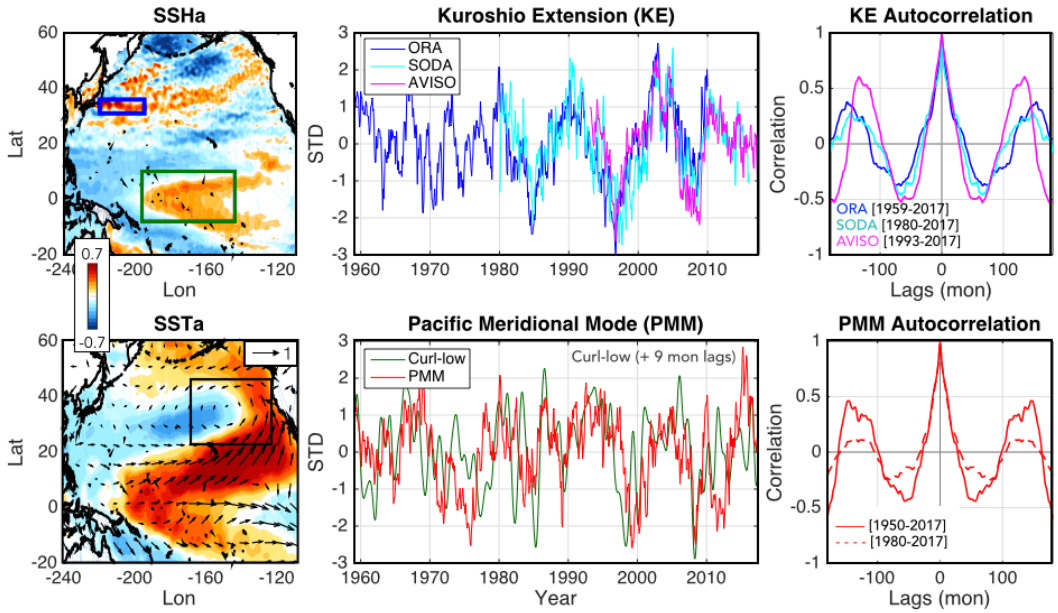

Figure 3.1. Spatial and temporal structures of the Kuroshio Extension (KE) and Pacific Meridional Modes (PMM) over the historical period. The spatial patterns of the KE and PMM computed by correlating (a) SSHa and KE index and (d) SSTa/winds and PMM index (see text for definitions). Normalized observational time variations of the (b) KE and (e) PMM indices between 1959-2017. The green line of (e) is the curl downstream index computed by using a downstream curl pattern of black box in Figure 3.4a. Autocorrelation function of (c) KE and (f) PMM indices with different time period.

In this study, we combine satellite sea surface height (SSH) data with several reanalysis products, to present observational evidence that a preferred decadal timescale in the KE may arise from the interaction between the KE and the extra-tropical/tropical Pacific variability associated with the Pacific Meridional Modes (PMM) and the El Niño Southern Oscillation (ENSO). Initial support for this hypothesis comes from examining the spatial and temporal structure of the KE SSH anomalies (SSHa) variability (Figures 3.1a-3.1c). Specifically, the KE temporal variability, measured by taking a time-series of the average satellite SSHa between 31°–36°N & 140°–165°E (Figure 1a, blue box, see Data and Methods for details), is characterized by strong low-frequency fluctuations (Figure 3.1b) that have a clear decadal spectral peak (~10 years) evident in the auto-correlation function, particularly after the 1976/77 Pacific climate regime shift (Figure 3.1c). The spatial footprint of this KE decadal variability extends to the central tropical Pacific variability (Figure 3.1a, green box), where several studies have reported a weak, but still significant, preferred decadal spectral peak ~10 years in SST [*Cobb et al., 2003; Nurhati et al., 2011; Sullivan et al., 2016*] that is identical to that of the KE[21] (see Supplementary information Figure 3.1). These results suggest that the KE and central Pacific interact to give rise to a preferred quasi-decadal period (~10 years), potentially enhancing the decadal predictability of the North Pacific.

3.2 Data and Methods

Observations for investigating the SSH-based KE variability are obtained by three different SSH dataset within the period between 1959 and 2017 from the European Centre for Medium-Range Weather Forecasts (ECMWF) Ocean Reanalysis System: ORA-S3 [*Balmaseda et al., 2008*], Simple Ocean Data Assimilation (SODA) reanalysis version 3

[*Carton et al., 2018*], and satellite distributed by Archiving, Validation, and Interpretation of Satellite Oceanographic (AVISO) data available at https://www.aviso.altimetry.fr/en/data/products/auxiliary-products/mss.html [*Schaeffer et al., 2016*]. To explore the KE variability at the air–sea interface, the monthly mean Hadley Centre Sea Ice and Sea Surface Temperature (HadiSST) dataset [*Rayner et al., 2003*] are used, and sea Level pressure (SLP), geopotential height at 300 hPa (Z300), zonal and meridional wind stress are taken from European Centre for Medium-Range Weather Forecasts (ERA) reanalysis product [*Dee et al., 2011*]. All anomalies are constructed by removing the mean monthly climatology and linear trend at each grid point. The limited period between 1959 and 2017 is analyzed.

The KE index is defined as monthly area-averaged SSH anomalies in the 31°–36°N & 140°–165°E region (Box in Figure 3.1a) following the Qiu et al. (2014) [*Qiu et al., 2014*]. The SST-based monthly PMM index was obtained at https://www.esrl.noaa.gov/psd/data/timeseries/monthly/PMM/ [*Chiang and Vimont, 2004*]. The Central Pacific ENSO (CP-ENSO) is defined by utilizing the C-index computed by the sum of the first and the second principal component of tropical SST [*Takahashi et al. 2011*]. All the indices are normalized and detrended before analysis. To show the oceanic/atmospheric spatial responses to the time-varying KE dynamic state and their oscillation patterns, we use lead/lag correlation maps between oceanic/atmospheric anomalies and KE index.

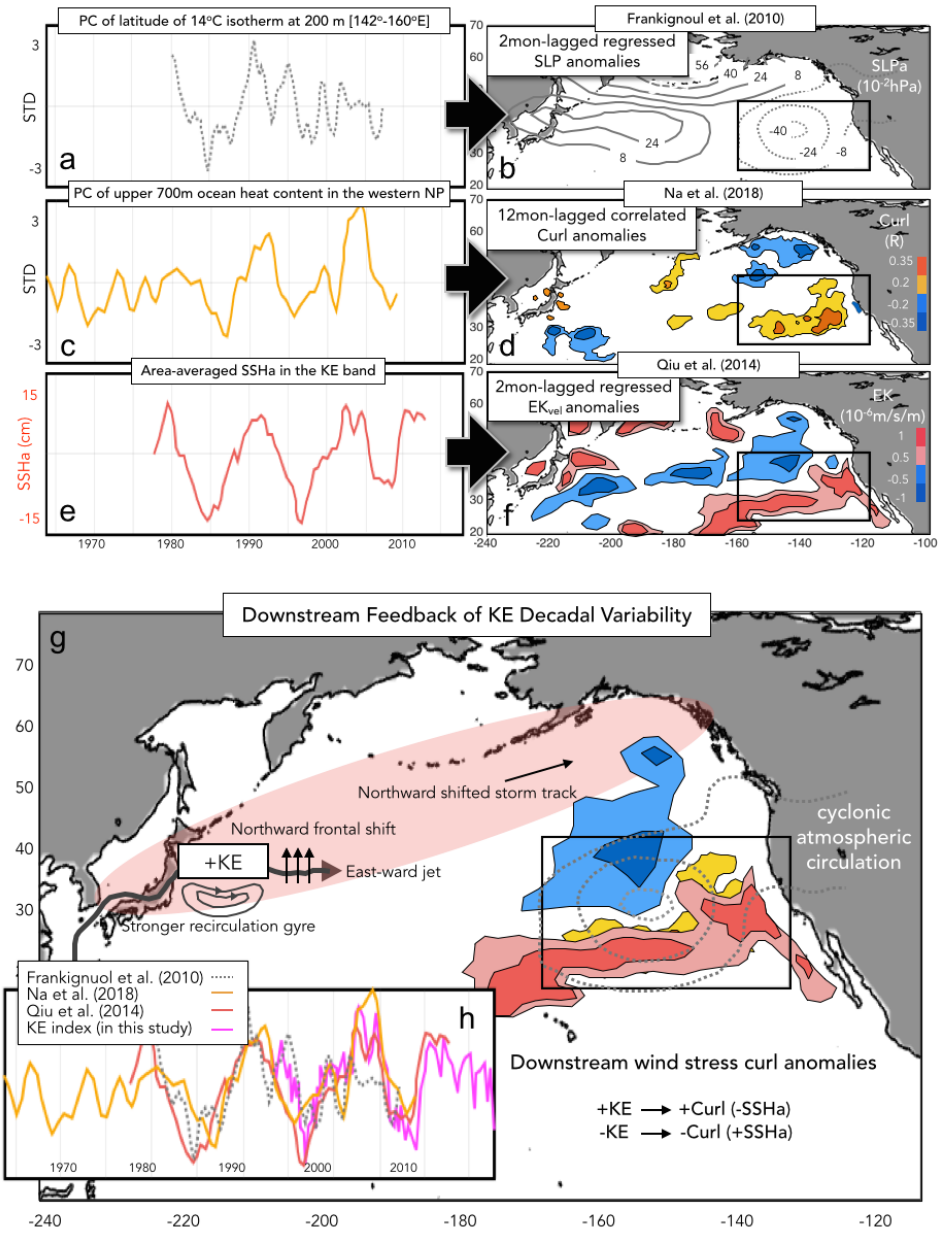

Figure 3.2. Observational results of the KE feedback from previous studies. The KE index used in (a) Frankignoul et al. 2010, (c) Na et al. 2018, and (e) Qiu et al. 2014. The corresponding atmospheric/oceanic responses using (b) sea level pressure anomalies, (d) wind stress curl anomalies, and (f) Ekman pumping velocity field anomalies to the positive KE mode (e.g., stable state). (g) Illustration of the KE feedback with an integrated KE downstream feedback by -SLP anomalies in (b), +Curl anomalies in (d) +EK anomalies in (e), where the migration of North Pacific storm tracks leads downstream SLP/Curl/Ek responses as described in Qiu et al. (2014). (h) Comparison of the KE indices from Frankignoul et al. 2011[36] (dashed), Na et al. 2018 (yellow), Qiu et al. 2014 (red), and this study (pink).

3.3 Hypothesis 1: Ocean-atmosphere coupling internal to the North Pacific

Over the last decade, many studies concluded that the KE region is governed by the North Pacific air-sea coupled system where the decadal changes in the wind forcing over the midlatitude North Pacific are responsible for the transitions of the KE dynamic state (e.g., stable vs. unstable) [*Qiu and Chen 2005, 2010; Taguchi et al., 2007; Kelly et al. 2007; Ceballos et al., 2009; Qiu et al., 2014*]. Qiu et al. (2014) examines the characteristics of the KE decadal system using four dynamic quantities: the length of KE jet, the upstream KE position, the SSH difference across the KE jet, and the KE recirculation gyre strength. For example, through satellite altimeter measurements it is found that the stable state (positive phase) of the KE is characterized by an eastward-extended surface transport of KE jet with a northward migration of latitudinal position of the KE front and an enhancement of the southern recirculation gyre (see schematic Figure 3.2g). The reverse holds when the KE switches to the unstable state (negative phase). Qiu et al. (2014) demonstrates that the SSHa variability in the KE southern recirculation box [31°–36°N & 140°–165°E] is an effective way to represent the average fluctuation of those dynamic quantities. The KE SSHa variability between a stable (+SSHa) and an unstable (-SSHa) states (Figure 3.1b) are remotely modulated by the arrival of oceanic Rossby waves which are excited by anomalous wind stress curl over the central and eastern North Pacific region [*Miller et al., 1998; Deser et al., 1999; Seager et al., 2001; Schneider et al., 2002; Qiu 2003; Taguchi et al., 2007; Sasaki et al., 2013; Qiu et al., 2014*]. The westward propagating SSHa forcing of KE has been confirmed by subsequent studies with a homvuller diagram of Rossby waves traveling along the midlatitude North Pacific KE band [31°-38°N] [*Ceballaos et al., 2009; Andres et al., 2009; Qiu et al 2014*].

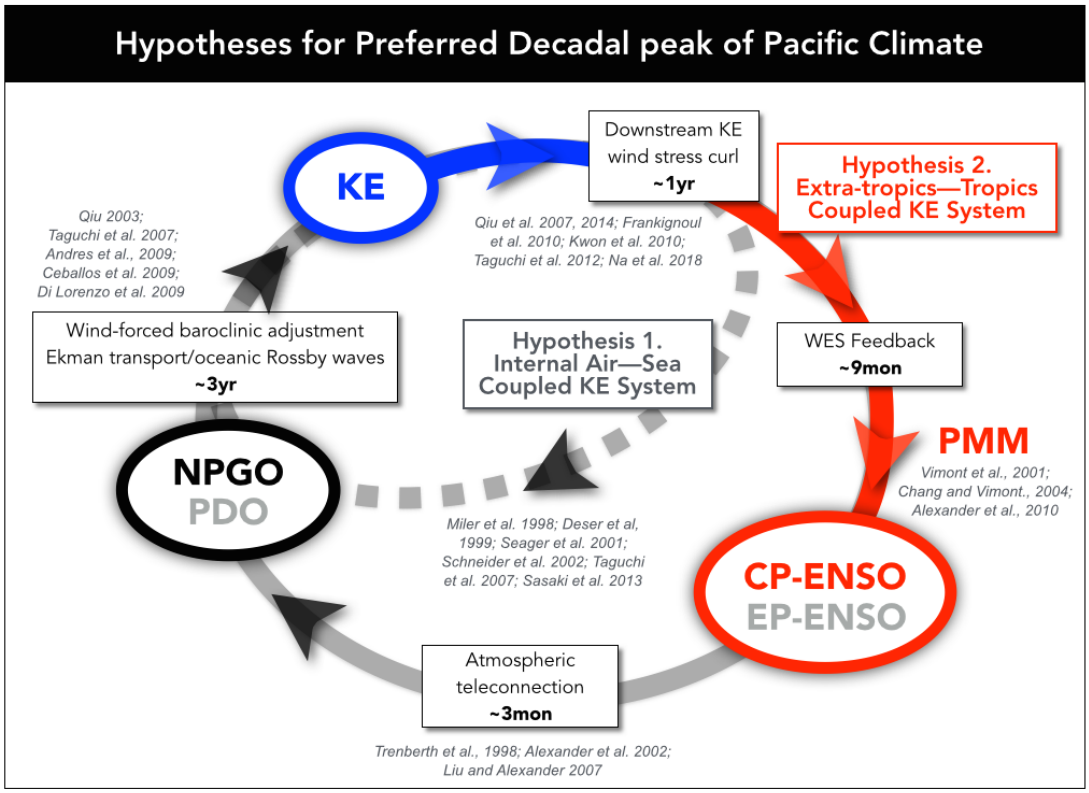

Figure 3.3. Diagram of hypotheses for generating preferred decadal timescale in Pacific climate variability. The internal air-sea coupled KE system proposed by Qiu et al. (2014) (KE → KE downstream response → PDO/NPGO → KE, *hypothesis 1*) and the coupled Extra-tropics-tropics KE system suggested in this study (KE → KE downstream response → PMM/CP-ENSO → NPGO → KE, *hypothesis 2*).

While the influence of large-scale wind forcing on the KE is well established, the feedback of the KE back to the atmosphere is less understood. Qiu's hypothesis states that once the KE is in the stable state, the ocean-to atmosphere heat release and the oceanic front tend to expand northward, leading a northward shift in the North Pacific storm track. This poleward shifted in the storm track is characterized by a dipolar structure of transient eddy temperature flux with a strong north-south gradient along a northeast-southwestward direction. Qiu et al. (2014) explains that the dividing line (e.g., maximum gradient) is associated with the region where the time-mean Ekman pumping velocity anomalies field

is zero (W_{ek} = 0), which indicates also a northward migration of the W_{ek} response to the KE. The study concludes that the tilted spatial structure of the KE Ekman pumping velocity feedback allows the W_{ek} anomalies in KE band [31°–36°N] to have a sinusoidal spatial pattern, which can excite large-scale Rossby waves that reach the western boundary back (Figure 2g) [*Ceballaos et al., 2009; Andres et al., 2009; Qiu et al 2014*]. Support for this air-sea coupled mechanism of the KE feedback comes from several observational studies that investigate the downstream atmospheric/oceanic response to the KE stable state (Figure 3.2). Even though the definitions of the KE variability (e.g., indices) differ among these previous studies (Figure 3.2a, 3.2c, and 3.2e), a comparison of their time-series reveals strong overlaps in the low-frequency KE variability (Figure 3.2h). Similarly, the downstream spatial response found in these studies, despite the use of different response variables like sea level pressure (SLP) anomalies (Figure 3.2b), wind stress curl anomalies (Figure 3.2d) and Ekman pumping velocity anomaly (Figure 3.2f), all show a consistent response (e.g., cyclonic atmospheric circulations) in the subtropical eastern Pacific (Figure 3.2g).

In Qiu's hypothesis, the KE downstream wind forcing (Figure 3.2g) is crucial because the generated midlatitude anomalous wind stress curl is thought to project on the same wind forcing patterns that excite the large-scale Rossby waves that propagate into the KE, which would allow the KE system to oscillate over decadal timescale [*Qiu et al., 2014*]. This hypothesis is summarized in a schematic of Figure 3.3 (Hypothesis 1). Specifically, the downstream atmospheric response of the KE induces overlying-high and downstream-low SLP anomalies [*Kwon et al., 2010; Frankignoul et al., 2010; Taguchi et al., 2012; Qiu et al., 2014; Ma et al., 2015; Reverald et al., 2017*] and may energize the atmospheric variability of the Aleutian Low and/or the North Pacific Oscillation, which in

turn drive the two dominant oceanic modes, the PDO and the North Pacific Gyre Oscillation (NPGO) respectively [*Di Lorenzo et al., 2003*]. Once excited, the PDO and NPGO SSHa signals propagate westward into the KE with a ~3 years lag [e.g., *Miler et al., 1998; Deser et al., 1999; Qiu 2003; Seager et al., 2001; Schneider et al., 2002; Taguchi et al., 2007; Sasaki et al., 2013*]. This midlatitude wind-SSH coupling of the North Pacific may explain the preferred decadal period ~10 years of the KE and improve the predictive skill of low-frequency KE variability. Qiu's hypothesis states that the preferred time-period for one phase of the KE (~5 years) is obtained by the sum of (1) persistence timescale of the KE index (~1-2 years) and (2) delayed SSH feedback via baroclinic Rossby waves (~3 years). Although the Qiu's conceptual model can lead to enhance decadal variance (Figure 3.3, Hypothesis 1), a closer examination of the downstream response pattern of the KE shows significant differences from the forcing patterns of the NPGO, PDO and KE in the central and eastern North Pacific. To show this, we begin by defining the spatial and temporal downstream response structure of the KE in the observed wind stress curl anomalies.

3.3.1 Definition of the KE atmospheric downstream response and Curl index

To extract the atmospheric downstream response pattern of the KE (Figure 3.4a), we compute a set of correlation maps of the KE index with the wind stress curl for lags 0-12 month and average these maps to obtain the pattern of the KE atmospheric response. These lags are selected based on previous studies that document a persistent downstream atmospheric response on these timescales (see Figure 3.2). Prior to the computation of the correlations, a 12 months lowpass filter is applied to the wind stress curl field to better extract the low-frequency response. Given that previous studies have shown that the KE downstream response is persistent from 0-12 months, this averaging approach allows to

recover a pattern of response that is consistent with the previous findings (compare Figure 3.4a with the patterns from previous studies in Figure 3.2). In this framework, the KE downstream response is interpreted as a slow nudging of the storm tracks rather than a sudden change in the atmospheric circulation that is more typical of an ENSO teleconnection (e.g., the excitation of a train of atmospheric Rossby waves). We next use the correlation pattern (Figure 3.4a, black box) to define a curl index of the KE downstream response (here and after referred to as the curl downstream index). Specifically, the correlation pattern of Figure 3.4a, is projected onto the raw and 12-month lowpass filtered wind stress curl anomalies to extract indices of temporal variability of the wind stress curl pattern in the eastern Pacific region [30-50N and 170-120W] outlined by the black box of Figure 3.4a. The resulting curl downstream indices (black=12m lowpass and gray=raw lines in Figure 3.4b) shows significant correlations with the KE index (R=0.6 with the 12month lowpass curl index, R=0.25 with raw curl index), when the KE index is leading by 12 month. A cross correlation analysis between the KE index and the 12m lowpass curl index confirms that the strongest correlation is when the KE index leads the curl index by 12 months (Figure 3.4c).

3.3.2 Relation between KE atmospheric response pattern and the NPGO/PDO forcing pattern

We now compare the downstream response pattern of the KE (Figure 3.4a) with the forcing patterns of the PDO, NPGO and KE in the central and eastern North Pacific. The forcing patterns for the NPGO and PDO are obtained by correlating the indices of the climate modes with the wind stress curl anomalies (Figure 3.5c and 3.5e). Similarly, the forcing pattern of the KE is computed by correlating the KE index with the wind stress curl

anomalies 36 months earlier (to account for the ocean Rossby wave excitation and propagation). Consistent with previous studies, we find that the NPGO, and to some extent the PDO, forcing patterns compare well with the spatial structure of the KE forcing pattern (compare Figure 3.5a against 3.5c, and 3.5e)[*Qiu, 2002; Ceballos et al. 2009*]. However, if we compare the KE, NPGO, and PDO forcing patterns with the KE downstream response pattern (Figure 3.4a), we find important differences and an overall insignificant spatial correlation.

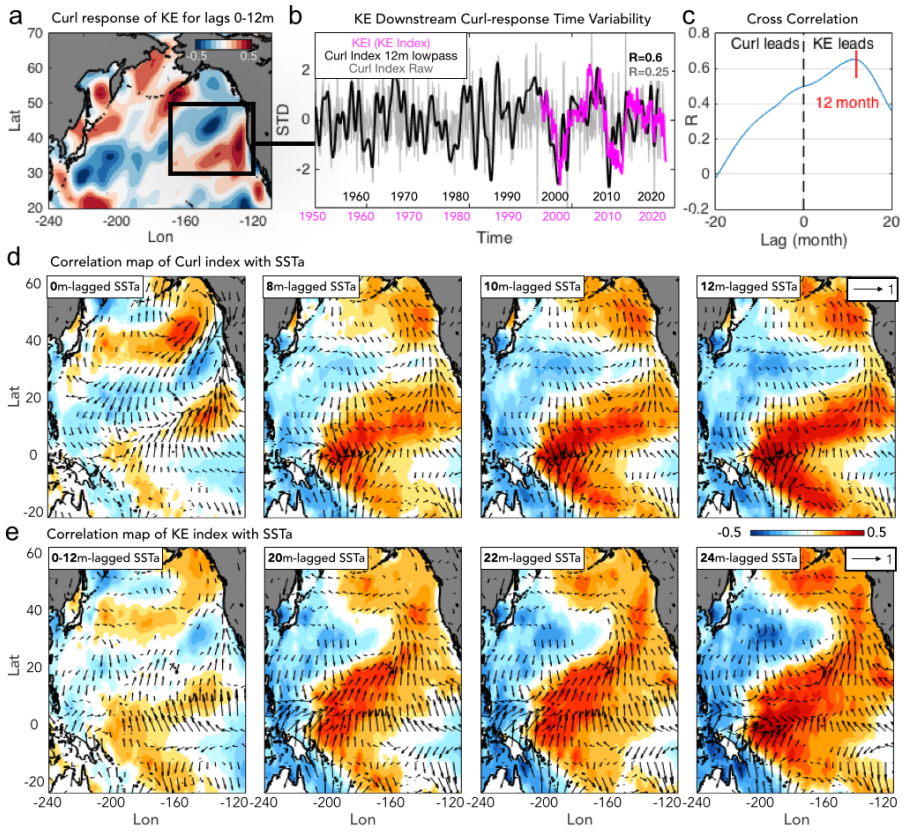

Figure 3.4. Spatial and temporal structures of downstream wind stress curl feedback of the KE. (a) Averaged correlation maps of wind stress curl and the KE index for lag 0-12 months (lagged curl anomalies vs. KE index). (b) Comparison between the KE index (pink) and curl indices (12-month lowpass curl index-gray line and raw curl index-black line) with correlation coefficients R (R=0.6 for the 12-month lowpass curl index, R=0.25 for the raw curl index both at 99% confidence level). (c) Cross-correlation of 12-month lowpass curl index and KE index. (d) Correlation maps of 12-month lowpass curl index with lagged

SSTa and wind vectors at 0, 8, 10, and 12 month. (e) Correlation maps of KE index with lagged SSTa and wind vectors at 0-12 average, 20, 22, and 24 month.

Further inspection of the spatial and temporal structure of the KE atmospheric response in the SSTa and wind stresses fields, reveals that the KE downstream pattern is more closely related to the forcing pattern of the PMM (see next section and Figures 3.4d and 3.4e).

3.3.3 Relation between KE atmospheric response pattern and PMM/CP-ENSO

To examine the KE response pattern in the wind stress curl in more depth, we compute correlation maps of the curl downstream index (Figure 3.4b, black line) with SSTa and wind stress anomalies at lags of 0, 8, 10 and 12 months (Figure 3.4d). These sets of maps reveal the spatial and temporal forward evolution of the SSTa and winds stress vectors associated with the KE downstream atmospheric response and are characterized by a progression from a PMM structure (e.g., 0 month lag shows the typical PMM pattern with a weakening of the off-equatorial winds) to a central Pacific El Niño type pattern (lags of 8, 10, 12 months). This suggest that the response pattern of the KE, even though it may have some impact on the forcing patterns of the PDO and NPGO, is more consistent with a PMM/CP-ENSO response. These results lead to a revised hypothesis for explaining the preferred decadal timescale in the KE and central tropical Pacific variability.

3.4 Hypothesis 2: Coupling between the extra-tropical and tropical Pacific via Pacific Meridional Modes

The PMM is a coupled SST-surface wind pattern in the mid-latitude North Pacific characterized by the subtropical north-south SST gradient (Figure 3.1d) which is driven by

the stochastic atmospheric forcing (e.g., North Pacific Oscillation, NPO) [*Chiang and Vimont, 2004; Chang et al., 2006*]. We hypothesize that the KE downstream wind stress response, discussed in the previous section (Figure 3.4), contributes to the forcing of the PMM, which triggers the air-sea interactions over the Northeast Pacific (e.g., WES feedback, *Xie 1999*). The midlatitude Pacific thermodynamic mechanism that relies on ocean-atmosphere coupling could explain the observed persistence to the downstream ocean-atmosphere anomalies, and favor the development of the PMM through weakening the trade winds (Figure 3.4d) and the consequent growth of the subtropical Pacific SSTa (KE→PMM, Hypothesis 2 in Figure 3.3).

Given that the KE downstream atmospheric response projects onto the excitation region of the PMM and develops into CP-ENSO type pattern (Figure 3.4d), it is highly plausible that the KE can also impact tropical climate through the well-known ENSO precursor dynamics associated with the PMM (PMM/CP-ENSO, Hypothesis 2 in Figure 3.3). During the PMM, the WES feedback enables southward coevolution of SSTa and wind stress anomalies that reach the central tropical Pacific where they induce ENSO favorable condition [*Chiang and Vimont, 2004; Chang et al., 2006; Capotondi et al., 2015*]. The excitation, propagation and arrival of the PMM anomalies in the tropics can lead to both flavors of ENSO on timescale of 9 months (see Supplementary Figure 3.2). The excited ENSO atmospheric teleconnections (e.g., Pacific/North American pattern) then project the variance back into the central/eastern North Pacific on timescales of 1-3 months [*Wang et al., 1999; Alexander et al., 2002; Vimont, 2005; Liu et al., 2007; Di Lorenzo et al., 2010; Furtado et al., 2012; Di Lorenzo et al., 2015; Di Lorenzo and Mantua, 2016*], leading to a deeper than normal Aleutian low (e.g., in the case of an eastern Pacific ENSO) or southern lobe of the NPO (e.g., in the case of a CP-ENSO, see Supplementary Figure 3.2). The

atmospheric anomalies in the Aleutian Low or NPO excited and drive the westward-propagating oceanic Rossby waves (e.g., the PDO and NPGO SSHa signals) that reach and impact the KE state on timescales of 2.5-3 years. This sequence of teleconnections is summarized in Hypothesis 2 in Figure 3.3: KE (12 months)→ KE downstream response (9 months) → PMM/CP-ENSO (1-3 months)→ NPGO (36 months)→ KE (*note that while the low-frequency expression of this sequence reveals a CP-ENSO/NPGO signatures, on interannual timescales we don't exclude contributions from eastern Pacific ENSO/PDO*). Consistent with this view, the timescale of the KE/PMM fluctuations are quasi-identical especially since the 1976-77 regime shift (Figures 3.1b and 3.1e) with the equivalent preferred oscillation period of ~10 years (Figures 1c and 1f, power spectra and coherence of the KE and PMM are shown in Supplementary Figure 3.1).

Using hypothesis 2 in Figure 3.3 as a roadmap for the proposed KE dynamic pathway, we explore the observational evidence associated with the dynamics pathway linking the KE to the central tropical Pacific. Specifically, we examine more closely the role of the KE downstream atmospheric response in the eastern Pacific as forcing of the PMM and central tropical Pacific variability (section a below). The link between ENSO teleconnections and the North Pacific modes (see Supplementary Figure 3) will not be discussed given the large amount of existing literature documenting this part of the loop in hypothesis 2 (Figure 3.3). However, we will examine more closely the patterns of wind stress curl associated with the modes in relation to the atmospheric forcing pattern of the KE (section b below).

3.4.1 Impact of KE downstream atmospheric response on PMM forcing in eastern Pacific

Support for Hypothesis 2 (KE→PMM in Hypothesis 2 of Figure 3.3) comes from exploring the spatial evolution of the KE downstream atmospheric response in the ocean and atmosphere obtained by correlating the KE and curl downstream index with wind and SST anomalies at different lags in time (Figures 3.4d and 3.4e). The spatial progression of the curl downstream associated with the KE index shows a persistent cyclonic circulation over the Northeast Pacific, which projects onto a weakening of the off-equatorial trade winds and leads to the growth of subtropical warm SSTa through the WES feedback [*Xie and Philander, 1994*]. As the subtropical SSTa continue to grow, the PMM-like oceanic signature becomes more evident with strong wind vector anomalies that transition into the mature phase of the PMM (e.g., compare Figure 3.4e at lag 24 month with Figure 3.S1d).

The forcing of PMM associated with the KE atmospheric downstream feedback is also captured in a comparison of the time series of the PMM and the curl downstream index (Figure 3.1e). Significant correlation is found when the curl downstream leads the PMM by 9 month with R=0.39 over the entire period and R=0.54 after 1976 at 95% and 99% significance level respectively.

3.4.2 The atmospheric forcing of KE and its relation to the North Pacific modes

The link between the tropical variability (e.g., ENSO) and the North Pacific decadal modes via the "atmospheric bridge" is well established by previous literature [*Trenberth et al., 1998; Liu and Alexander 2007; Alexander et al., 2002*]. Once the ENSO atmospheric teleconnections project the tropical signal into the North Pacific, changes in the surface heat fluxes, wind-driven mixing, and Ekman pumping in the upper ocean drive the PDO-like and NPGO-like SSH signals that affect the KE system through westward propagating Rossby waves. Consistent with the previous findings, we find that the PDO/NPGO curl/SSH

patterns show a significant link of the KE atmospheric forcing (Figures 3.5a, 3.5c, and 3.5e) and its SSH signature (Figure 3.5b, 3.5d, and 3.5f) over the eastern North Pacific region. The cross correlation of the KE and the PDO/NPGO indices confirms that the KE has been interacting with the North Pacific decadal modes on quasi-decadal time scale, with significant lead/lag correlations especially to the NPGO ($R>0.6$, Figure 3.5g).

As we already noted in the previous section, the spatial progression of the KE index in wind stress curl and SSH field reveals that the KE atmospheric/oceanic downstream response patterns (Figures 3.5h-i at lag 0-12 month) are not correlated to the NPGO forcing patterns, showing a significant structural difference in the eastern North Pacific region (e.g., Figure 3.5h at lag 0-12 month vs. Figure 3.5e). Specifically, from the lagged 18-month, the tilted dipole structure of KE downstream wind stress curl changes into a blob pattern and increases in amplitude, as observed in the KE wind forcing pattern over the subtropical Northeast Pacific (Figure 3.5h). Corresponding to the spatial progression of KE curl feedback, the SSH progression also reveals the delayed response, showing that the significant eastern North Pacific SSHa appear only after the lagged 18-month (compare Figures 5i at lag 0-12 month and 30 month with Figure 3.5b).

Taken together, the examination of KE atmospheric/oceanic downstream response (section a) and forcing patterns (section b) implies that the KE downstream feedback might not be the decisive forcing to excite the baroclinic Rossby waves that effectively switch the KE phase. Instead, the eastern North Pacific wind forcing energized by the atmospheric teleconnections associated to the PMM/CP-ENSO (see Figures 3.4d and 3.4e) plays a more important role in modulating the decadal KE dynamic state by projecting onto the PDO and NPGO SSH anomalies that lead the phase transitions in the KE.

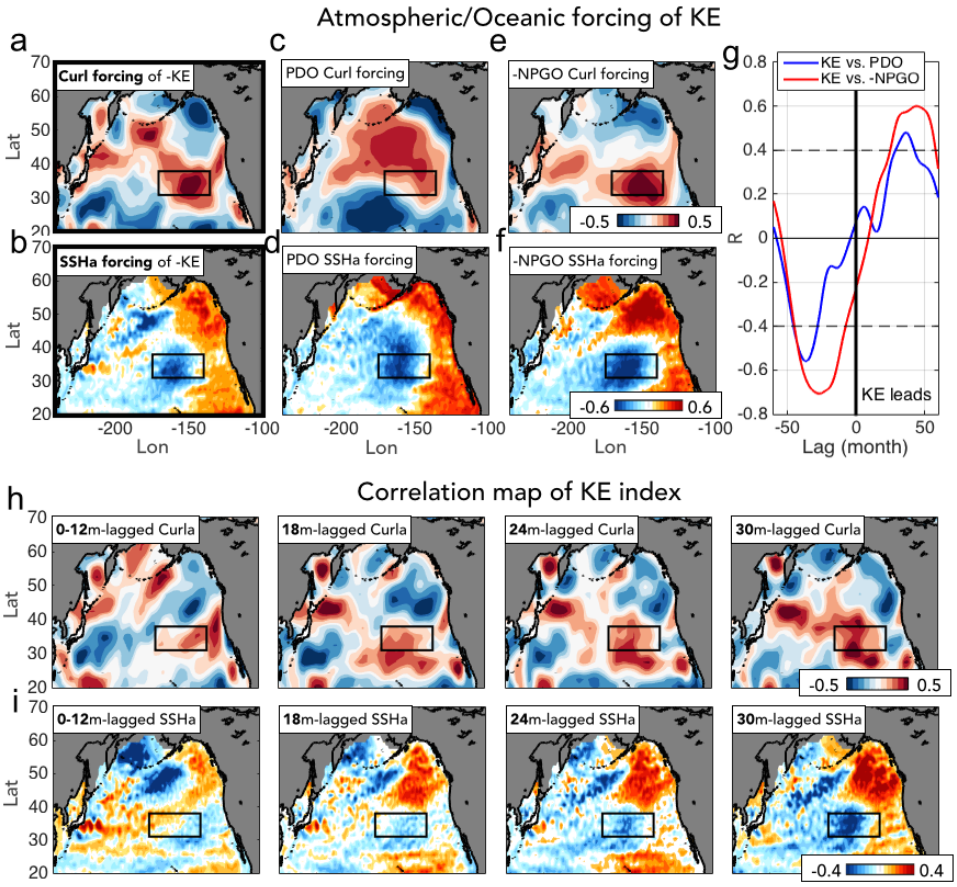

Figure 3.5. Comparison of KE/PDO/NPGO forcing patterns against the KE downstream response pattern in wind stress curl and SSH field. (a-b) Correlation maps of -KE index with (a) 3yr-leading wind stress curl and (b) 3yr-leading SSH anomalies. (c-d) Correlation maps of PDO index with (c) wind stress curl and (d) SSH anomalies. (e-f) Correlation maps of –NPGO index with (e) wind stress curl and (f) SSH anomalies. (g) Cross-correlation of KE and PDO (blue) and KE and -NPGO (red), where the indices are smoothed via 12-month running mean filter with 95% confidence level denoted as dashed lines. (h-i) Correlation maps of KE index with (h) lagged wind stress curl and (i) SSH anomalies at 0-12 average, 18, 24, and 30 month.

3.4.3 10 year spectral peak in the co-evolution of KE and PMM/CP-ENSO

The dynamical pathway of hypothesis 2 (Figure 3.3) suggests that the one phase of decadal KE state persists ~5 years with ~10 years oscillation timescales following the low-

frequency sequence of KE (12 months)→ KE downstream response (9 months) → PMM/CP-ENSO (1-3 months)→ NPGO (36 months)→ KE. This progression is evident from the temporal and spatial lead/lag relationships between the KE and PMM/CP-ENSO indices (Figure 3.6). As for the CP-ENSO index, the C index of Takahashi et al. 2011 was utilized by employing two principal components of SSTa in the tropical Pacific, whose spatial signature is only constrained to the central Pacific anomalies. Using this definition of the CP-ENSO and the PMM index, we note that the CP-ENSO decadal fluctuations are significantly correlated with the PMM at lag 0 (Supplementary Figure 3.4), which is consistent with the recent findings that the CP-ENSO is not only driven by the PMM but also interacts with the PMM on interannual timescales through the fast-positive feedback [*Stuecker, 2018*]. We find that the cross-correlation functions between the KE and PMM and KE and CP-ENSO (Figure 3.6a) both exhibit a clear sinusoidal shape with a preferred spectral power at the decadal timescale of ~10 years, which is particularly strong since the 1976/77 Pacific climate regime shift. The lead-lag relationship between the KE and the PMM is very significant with average positive and negative correlations above the 95% confidence level. The significant sinusoidal shape of the cross-correlations reveals that the KE and PMM/CP-ENSO have been interacting with each other on decadal timescales.

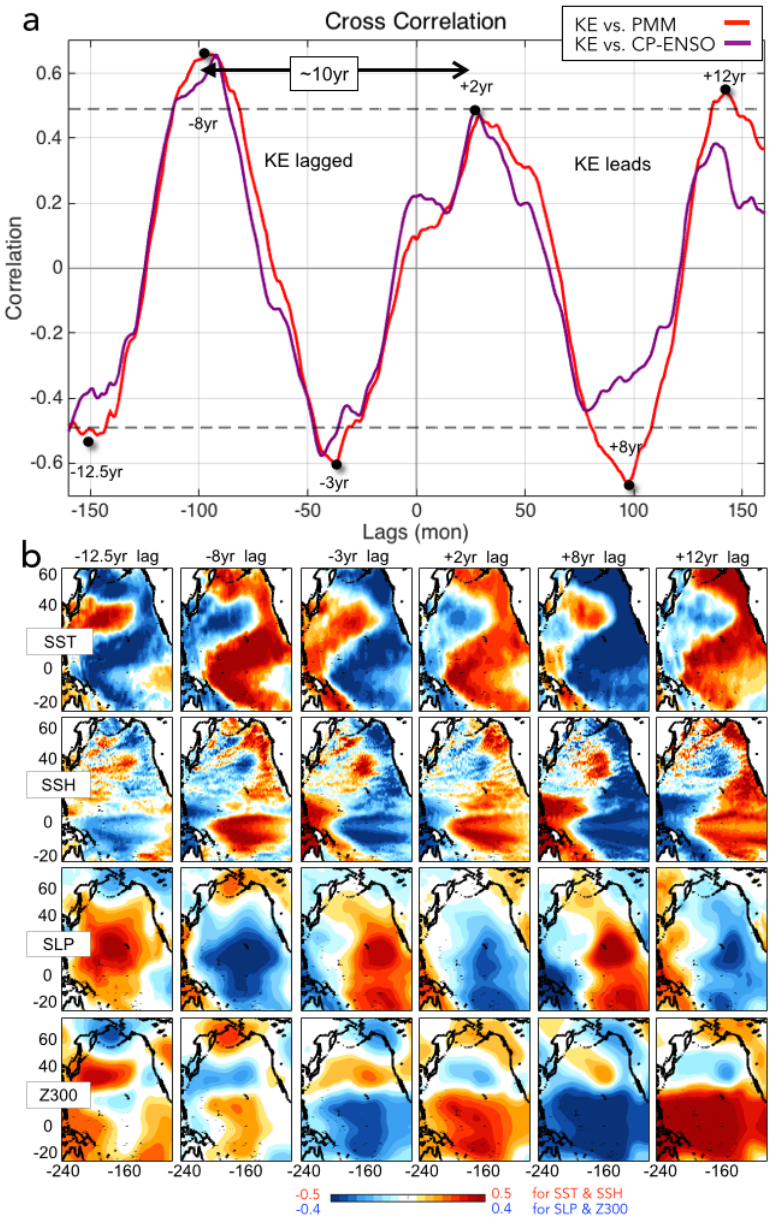

Figure 3.6. Temporal and spatial co-evolutions of KE and PMM. (a) Cross-correlation functions between the KE index with PMM and CP-ENSO indices. (b) Correlation maps between the KE index and oceanic/atmospheric variables (b-row1: SST, b-row2: SSH, b-row3: SLP, and b-row4: 300hPa geopotential height, Z300) using different time lags.

To inspect the spatial patterns that correspond to the temporal cross-correlation function between KE/PMM indices, we compute spatial correlation maps between the KE

index and oceanic/atmospheric variables over the period between 1990 to 2017 (Figures 3.6b) using different lags associated with the peaks of the cross-correlation function of Figure 3.6a. The spatial structures and temporal evolutions of SST (Figures 3.6b-row 1), SSH (Figures 3.6b-row 2), SLP (Figures 3.6b-row 3), and 300 hPa geopotential height (Figures 3.6b-row 4) patterns reveal that the decadal KE variability captures the oceanic/atmospheric signatures of the PMM and its progression. We find that the KE index can reconstruct clear transitions between the positive and negative phase of recurring PMM expressions which exhibit the hybrid of PDO-like and NPGO-like signatures with the central Pacific ENSO-like signal (Figures 3.6b-row1). The KE-induced SSH patterns (Figures 3.6b-row2) reveal that the KE variability is linked to the development of ENSO conditions, including the zonal SSH gradient in the tropical Pacific that generates the equatorial oceanic wave dynamics (e.g., downwelling equatorial Kelvin waves in positive ENSO). Corresponding to the tropical convective system caused by the central Pacific SST warming (Figures 3.6b-row1), the lower and upper atmospheric layers exhibit the large-scale east-west SLP seesaw pattern (Figures 3.6b-row3) with the characteristic pattern of the atmospheric Rossby wave train to the North Pacific at the 300 hPa (Figures 3.6b-row4). These tropical teleconnections to the North Pacific are well documented and are an important source of the reddening of the Pacific climate spectrum [*Trenberth et al., 1998; Liu and Alexander 2007; Alexander et al., 2002; Di Lorenzo et al., 2010; Furtado et al., 2012; Di Lorenzo et al., 2015; Capotondi et al., 2015*]. Taken together, the temporal interactions between the KE and PMM/CP-ENSO (Figure 3.6a) along with the spatial signatures inferred from lead/lag correlations with the KE index (Figure 3.6b) support our hypothesis that decadal fluctuations of KE can emerge through a two-way climate coupling between the North Pacific and the tropics.

3.5 Summary and Discussion

Using available observational dataset and reanalyses of the Pacific Ocean, this study explores an additional pathway for generating quasi-decadal fluctuations in the North and central tropical Pacific that relies on a two-way interaction between the KE in the extra-tropical and tropical Pacific. Through statistical analyses of the lead/lag relationship of the KE with large-scale ocean-atmosphere reanalysis, we offer initial evidence that the decadal SSH variability in the KE region is not independent of the PMM/ENSO, especially over the recent decades. The KE-PMM decadal interaction involves three key processes that are associated with the sequence of teleconnections outlined in the Figure 3.3 schematic: KE (12 months)→ KE downstream response (9 months) → PMM/CP-ENSO (1-3 months)→ NPGO (36 months)→ KE.

1. The persistent KE downstream atmospheric response (e.g., wind stress curl) projects on the forcing pattern that energizes the PMM and the central Pacific SST warming leading to ENSO conditions.
2. The activation of the ENSO system (Figures 3.4d and 3.4e) [*Vimont et al., 2001; Vimont et al., 2003; Alexander et al., 2010*] and its atmospheric teleconnections [*Trenberth et al., 1998; Liu and Alexander 2007; Chiang and Vimont, 2004*] contribute to energizing the North Pacific modes, specifically the PDO and NPGO.
3. The PDO and NPGO SSH anomalies propagate westward as Rossby waves impacting the KE state again [*Qiu 2003; Andres et al., 2009; Ceballos et al., 2009; Taguchi et al., 2007; Di Lorenzo et al., 2009*].

Although it is not possible to prove this oscillatory model without an appropriate modeling framework, a detail analysis of the KE downstream response (Figure 3.4) and forcing (Figure 3.5) patterns is consistent with our revised hypothesis 2. Specifically, we find that

the spatial and temporal evolution of the KE atmospheric downstream response is more consistent with the development of a PMM/CP-ENSO expression (Figure 3.4) than with the forcing pattern of the KE reverse phase (Figure 3.5a). This finding is further supported by the cross-correlation functions between indices of the KE and PMM/CP-ENSO (Figure 3.6a), which exhibit a sinusoidal shape with significant ± correlation peaks with ~5yr intervals. This is indicative of a preferred decadal oscillation of ~10 years (Figure 3.6a) and is consistent with the timescale of hypothesis 2: KE (12 months)→ KE downstream response (9 months) → PMM/CP-ENSO (1-3 months)→ NPGO (36 months)→ KE, which is also evident in the spatial progression of oceanic/atmospheric anomalies associated with this cross-correlation function (Figures 3.6b). To quantify how the KE signal propagates through the sequence we examined the signal to noise ($SNR=1/[1-R^2]$) ratio of the KE index against indices of the wind stress curl, PMM, CP-ENSO, NPGO, and KE using optimal lag correlations (R) at 12, 28, 30, 34, 60 months, which are consistent with the timescale of propagation of the sequence. On average the SNR remains constant at about 1.5 (Figure S3.5) suggesting a steady propagation of the signal across the sequence with little loss of variance. The SNR values become higher (~2) if we apply a low-frequency filter (5-year), suggesting that this sequence explains an important fraction of the low-frequency variance of the North Pacific system. As noted earlier, while the low-frequency expression of this sequence reveals CP-ENSO/NPGO signatures, on interannual timescales we don't exclude contributions from eastern Pacific ENSO/PDO. Further, the low-frequency expression of this sequence may serve as a physical mechanism to a new mode of quasi-decadal climate variability over the North Pacific—the Pacific Decadal Precession (PDP) [*Anderson et al., 2017; Anderson et al., 2019*] which is characterized by a ~10 year counter-clockwise progression of an atmospheric pressure dipole around the North Pacific, one phase of which

maps onto the NPO and is coincident with CP-ENSO variability discussed here, and another phase of which maps onto (and is coincident with) KE pattern of the atmospheric variability seen in Figure 3.2 (e.g., the spatial expression of the KE index).

In this study, the persistence of the KE downstream atmospheric feedback (~1yr) shown in our results supports the previous view, where the SSH-based KE variability has a long memory and can represent prolonged forcing of ocean dynamics (e.g., modulations of oceanic recirculation gyre and stability of the KE jet) to the North Pacific atmosphere [*Qiu 2003; Qiu et al., 2007; Ceballos et al., 2009; Qiu et al., 2014; Frankignoual et al., 2010; Na et al., 2018*]. Teleconnections excited by the central tropical Pacific SSTa are also known to influence the extra-tropical atmosphere in the region of the KE downstream wind stress curl response pattern [*Di Lorenzo et al., 2015*]. However, the spatial imprint of CP-ENSO onto the curl response pattern of the North Pacific (Figure S3.6b) is characterized by a meridional wave train that resembles more closely the North Pacific Oscillation (NPO) and is structurally different from the curl response pattern of the KE (Figure S6a). Nevertheless, we cannot exclude that the central Pacific SSTa have some impact on, and explain some of the variance (R=0.1-0.2) of, the KE wind stress curl response pattern, as evident from correlating the index of the curl response pattern with concurrent and leading SSTa in the tropical Pacific (Figure S3.6c). This is consistent with some studies suggesting that the CP-ENSO can influence the initiations of the North Pacific PMM in the following season by altering the NPO variability [*Di Lorenzo and Ohman, 2013*].

Although the analyses presented use monthly data, seasonality plays a key role in the extra-tropical/tropical interactions between the PMM and the ENSO system. While the KE variability is characterized by low-frequency fluctuations that have persistence on timescales of one year (e.g., KE auto-decorrelation length scale ~12 months), the wind

stress curl downstream response pattern to KE forcing (Figure 3.4a) exhibits a seasonal modulation with maximum amplitude during the Winter (from January to March) (see Figure S3.7). This seasonal timing is important because the dynamics of the PMM as precursors to ENSO are also seasonally locked with an initiation in Winter [*Xie 1999; Vimont et al., 2001*], development during Spring, and peak in Summer with the growing ENSO.

The observational evidence in this study provides a mechanistic hypothesis for exploring a new set of decadal climate interactions between the North Pacific western boundary current and the tropical Pacific, which could explain the quasi-preferred decadal peak in the observed spectrum of Pacific climate (e.g., central tropical Pacific, KE system). While we are unable to provide ultimate proof that this interaction is real, given the short observational record, the consistency of observations with this hypothesis provide a road map for designing advanced modeling experiment that can effectively test the relation between the KE and the tropical Pacific. Understanding this interaction becomes even more critical because of recent findings suggesting that the coupling between extra-tropics and tropics is intensifying in a warmer climate [*Di Lorenzo and Mantua, 2016; Joh and Di Lorenzo, 2017; Qiu et al., 2014; Kindulff et al., 2015; Liguori and Di Lorenzo, 2018*]. The enhanced coupling, which has been implicated in the rising of the Pacific decadal variance, is also consistent with the stronger periodic cross-correlation between the KE and PMM, suggesting that the interaction of KE and PMM may also be changing in future climate. A higher amplitude quasi-decadal fluctuations of the sequence KE/PMM, may lead to a stronger basis for making decadal predictions, especially for societally relevant biogeochemical quantities (e.g., salinity, oxygen, chlorophyll-A) and fisheries that are linked to the KE decadal variability [Yasuda 2003].

3.6 Supporting Information

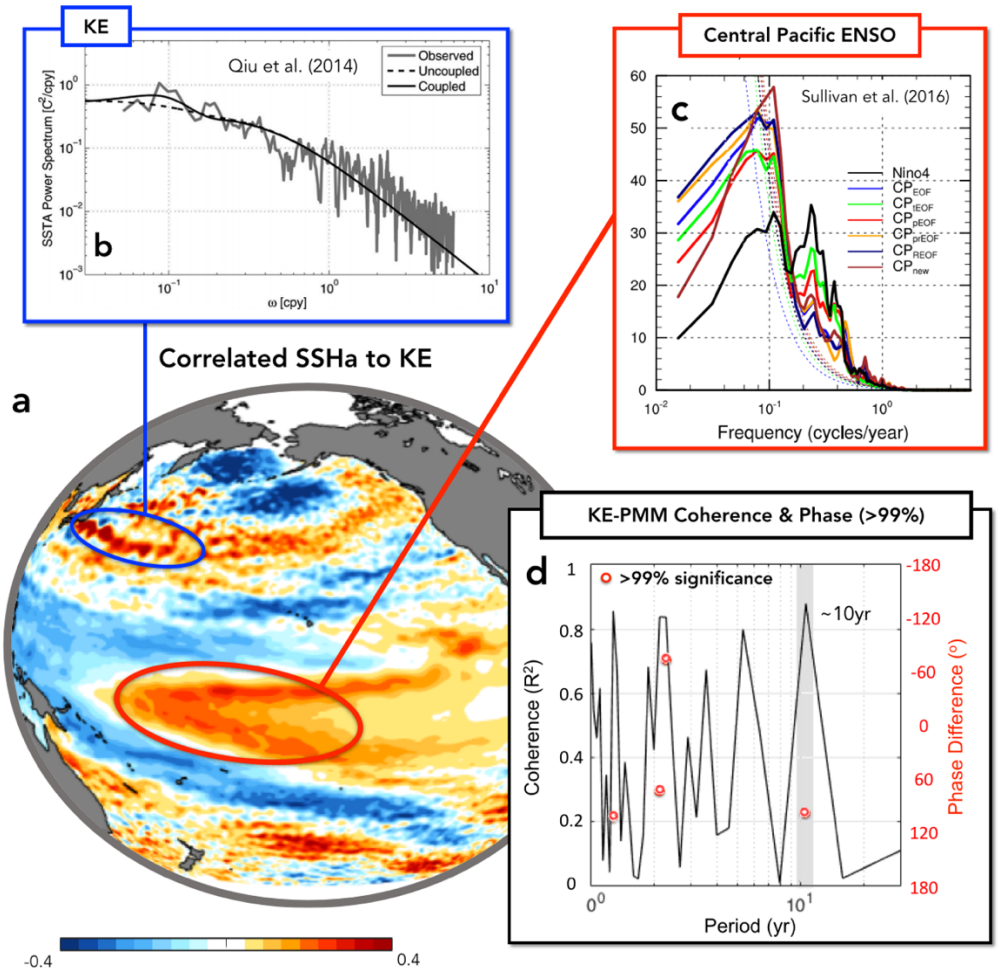

Figure S3.1. Linkages between the Kuroshio Extension (KE) region and the central tropical Pacific basin with the same preferred decadal-timescale of 10 years. (a) Spatial pattern computed by correlating SSH anomalies with the KE index between 1990-2017 using AVISO data (see text for definitions). (b) Power spectrum of the observed sea surface temperature (SST) anomalies in the KE band (gray line) documented by Qiu et al. (2014), where the power spectrum of SST under the air-sea uncoupled scenario is denoted as dashed line and that under the air-sea coupled scenario as the solid line. (c) Power spectrum of indices (computed following previous studies) of central Pacific El Niño Southern Oscillation (ENSO) documented by Sullivan et al. (2016). (d) Coherence and phase difference between KE and PMM indices used in this study.

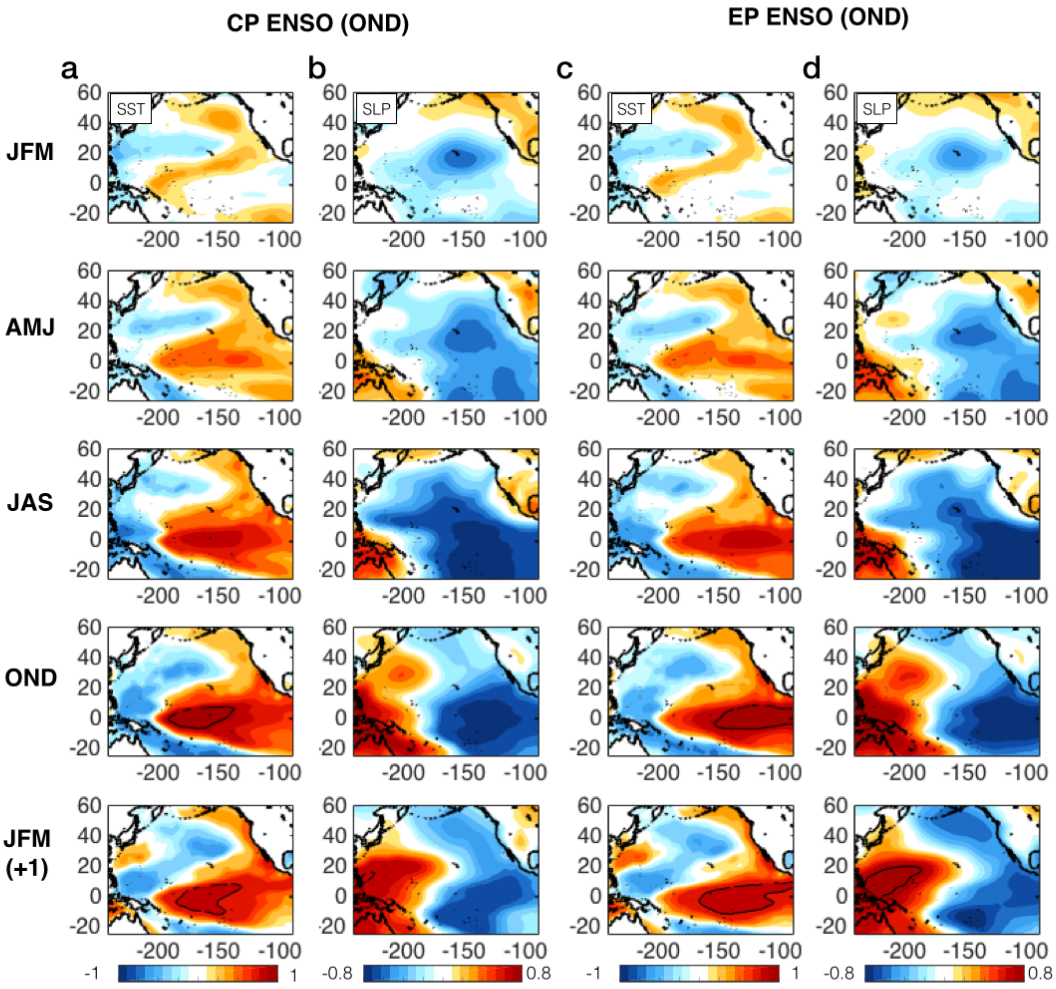

Figure S3.2. Spatial structure and temporal evolution of CP/EP ENSO in SST and SLP field in observations. (a-b) Correlation between the winter (OND) CP-ENSO and prior JFM, AMJ, JAS, concurrent OND, and following JFM seasonal mean (a) SSTa and (b) SLPa. (c-d) Correlation between the winter (OND) EP-ENSO and prior JFM, AMJ, JAS, concurrent OND, and following JFM seasonal mean (c) SSTa and (d) SLPa. CP/EP ENSO indices were simply defined by the Nino4 and Nino3 indices.

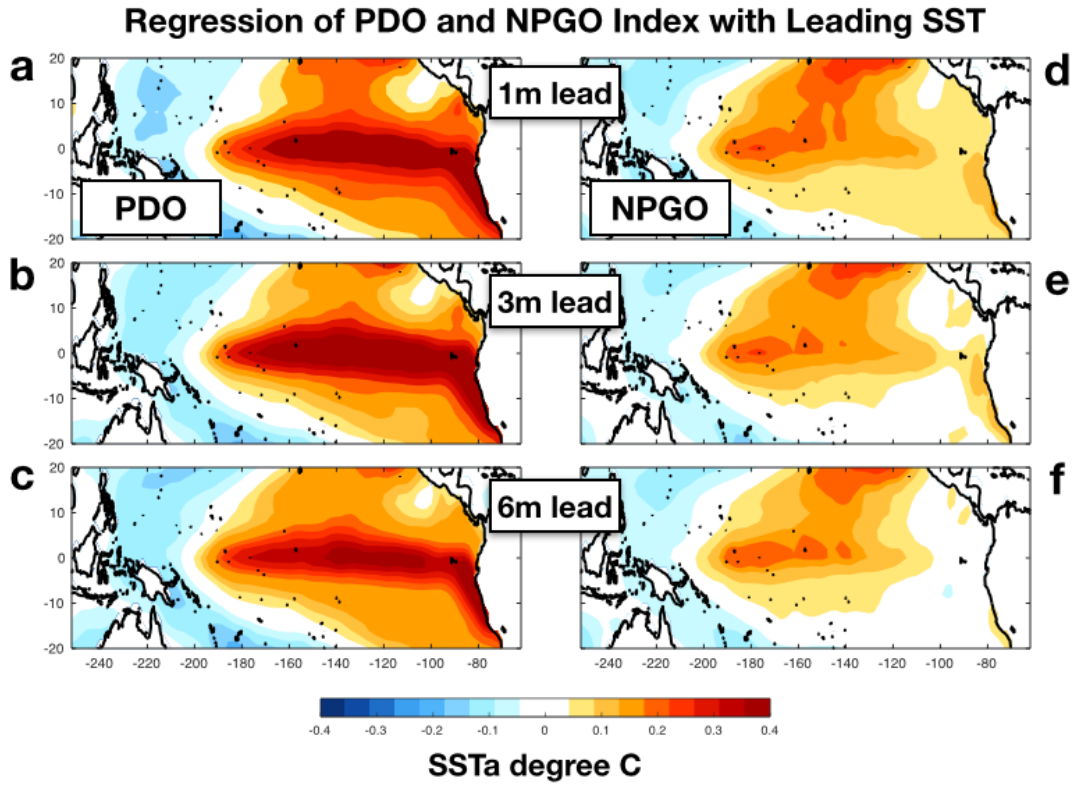

Figure S3.3. Leading SST patterns to PDO and NPGO. (a-c) Regression maps between the PDO index to leading SSTa by (a) 1 month, (b) 3 month, (c) 6 month. (d-f) Regression maps between the NPGO index to leading SSTa by (a) 1 month, (b) 3 month, (c) 6 month.

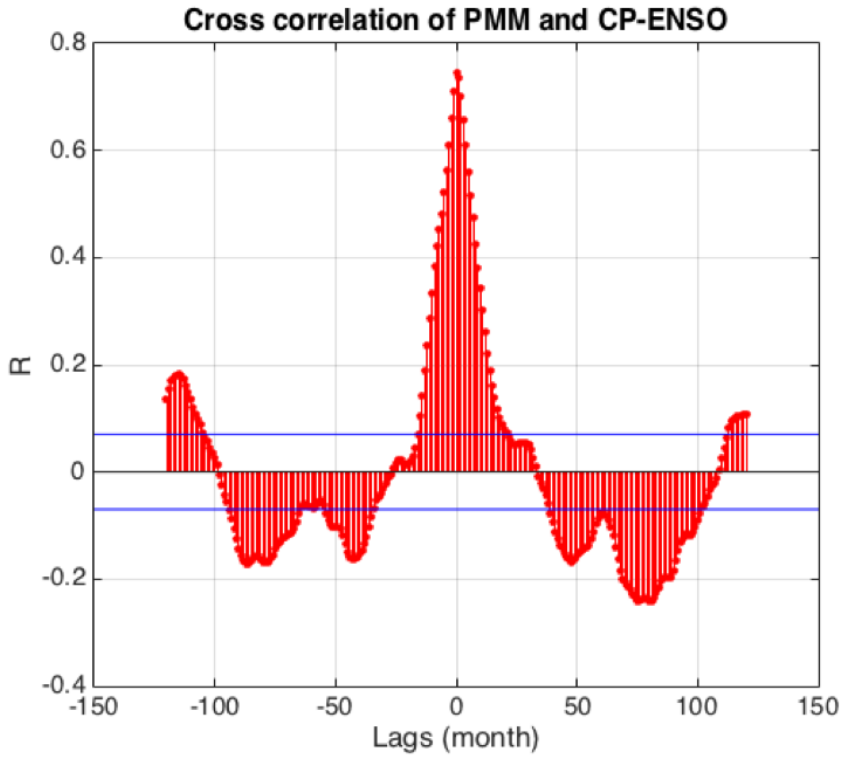

Figure S3.4. Cross correlation function between the PMM and CP-ENSO indices. The CP-ENSO index was utilized by the C index in Takahashi et al. (2011).

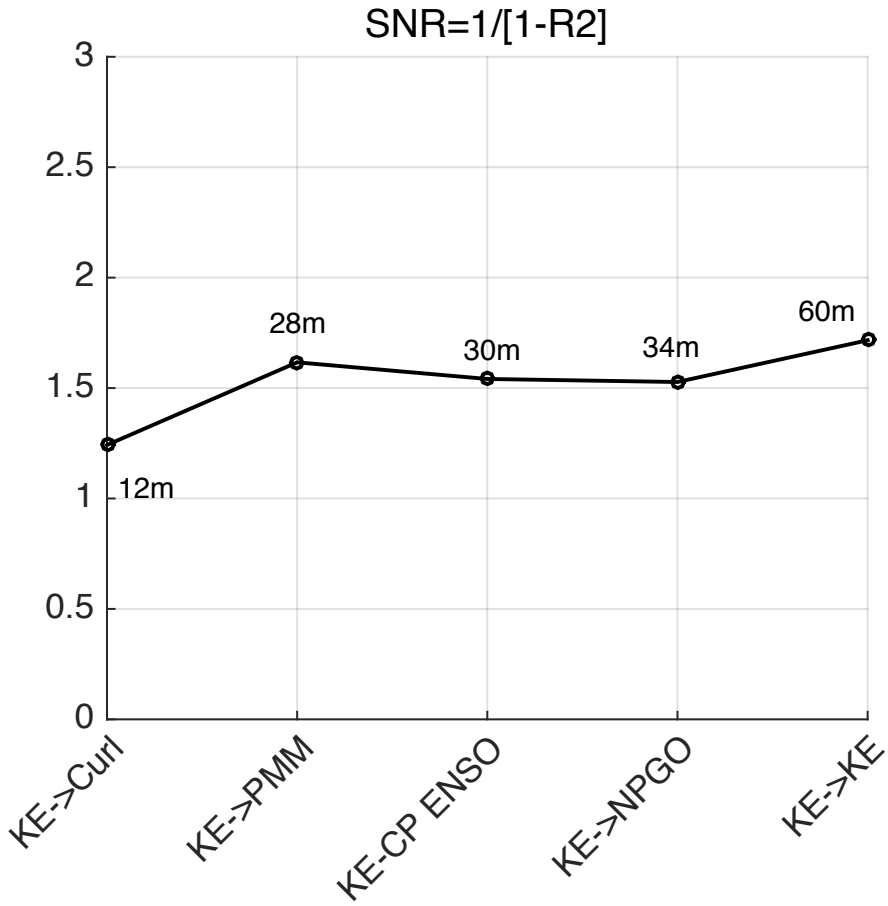

Figure S3.5. The signal to noise ratio (SNR) of the KE index against indices of KE downstream wind stress curl (Figure 1b), PMM, CP-ENSO, NPGO and KE with lag at 12, 28, 30, 34, and 60 months respectively. The ratio of signal and noise for each step is computed by using a linear regression y = a*x + n model to estimate the explained variance, where x is the KE index, y is a signal, and n is noise. The SNR was considered as signal/noise = var(y)/var(n) = $< y'^2 > / < n'^2 >$ = 1 / [1 – r(x,y)^2] using a relationship between a regression coefficient **a** and a correlation coefficient **r** of x and y in our hindcast model, where n'=y' - a*x; a = $< x'y' > / < x'^2 >$; r = $< x'y' > / (\sqrt{< x'^2 >}\sqrt{< y'^2 >})$.

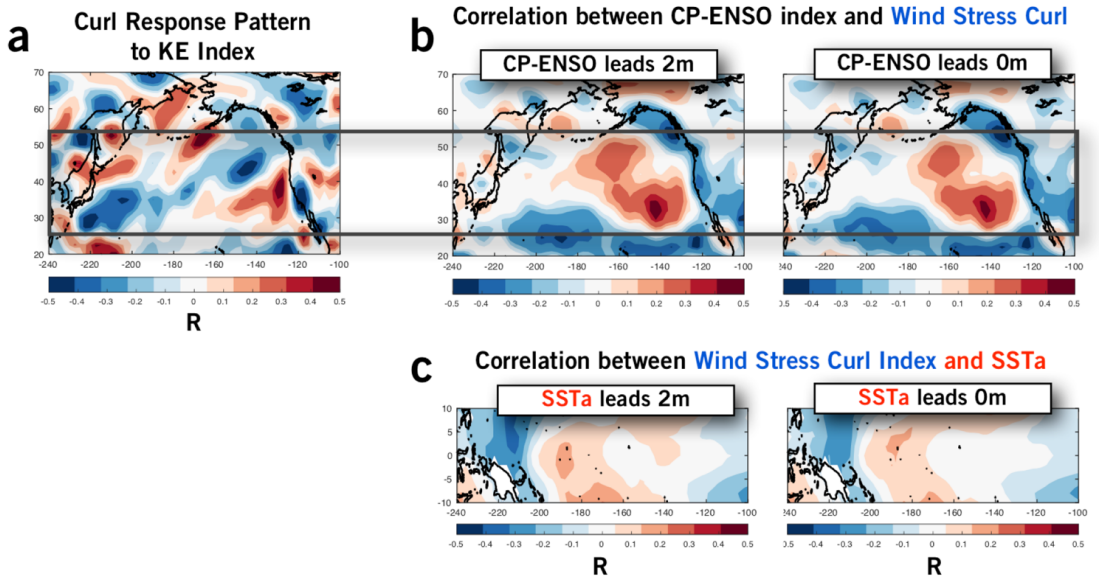

Figure S3.6. The role of the tropical Pacific in driving the KE wind stress curl response pattern. (a) The curl response pattern to the KE as shown in Figure 4a. (b) The curl response patterns to CP-ENSO anomalies extracted through a correlation of the CP-ENSO index with the wind stress curl anomalies at 2 and 0 months lead, whose structures show some important structural differences from the KE curl response pattern in panel a. (c) SSTa in the tropics impacting the KE curl response pattern extracted by correlating the KE curl index with SSTa at leads of 2 and 0 months. Weak correlations R=0.1-0.2 are found in the tropics indicating that some fraction of the variance in the KE curl response pattern may have tropical origin.

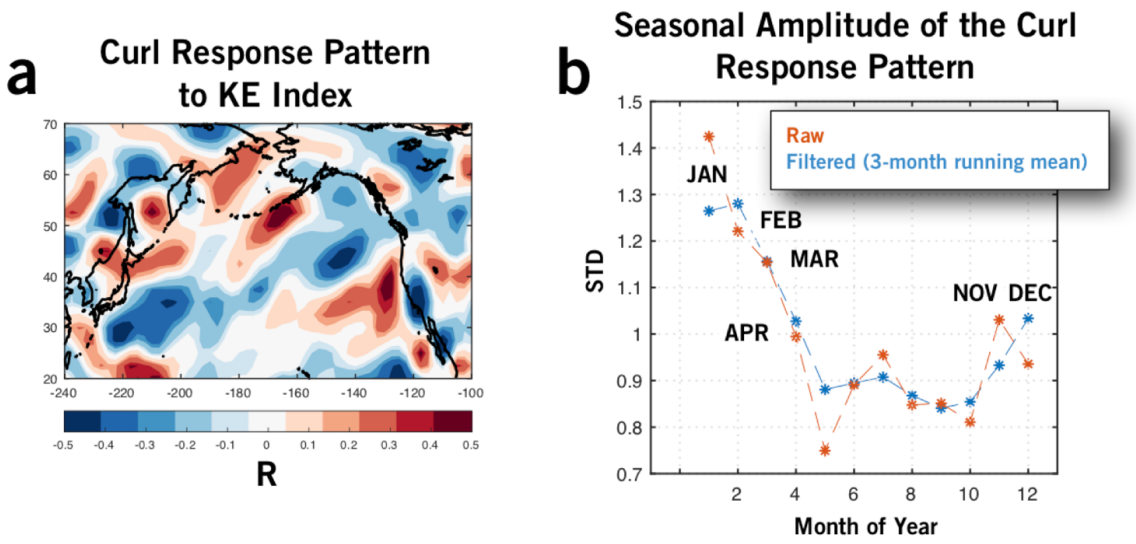

Figure S3.7. Seasonality of the KE wind stress curl response pattern. (a) The curl response pattern to the KE as shown in Figure 4a. (b) Seasonal standard deviation of the curl index extracted by projecting the KE curl pattern onto the raw and filtered (3-month running mean) monthly wind stress curl anomalies.

3.7 References

Francis, R. C. & Hare, S. Decadal-scale regime shifts in the large marine ecosystems of the North-east Pacific: a case for historical science. *Fish. Oceanogr*. **3**, 279–291 (1994).

Mantua, N.J., Hare, S., Zhang, Y, Wallace, J.M. & Francis, R.C. A. Pacific interdecadal climate oscillation with impacts on salmon production. *Bull. Amer. Meteor. Soc*. **78**, 1069-1079 (1997).

Nakata, K. & Hidaka, K. Decadal-scale variability in the Kuroshio marine ecosystem in winter. Fish. Oceanog. **12**, 234-244 (2003).

Di Lorenzo E. *et al*., North Pacific Gyre Oscillation links ocean climate and ecosystem change. *Geophys. Res. Lett.* **35(8)** (2008).

Sydeman, W.J. & Thompson, S.A. The California Current Integrated Ecosystem Assessment (IEA), Module II: Trends and Variability in Climate-ecosystem State. Report to NOAA, SWFSC, Environmental Research Division, Pacific Grove, California, 59 pp. (2010).

Cloern, J. E. & Jassby, A. D. Patterns and scales of Phytoplankton Variability in Estuarine-Coastal Ecosystems. *Estuaries and Coasts* **33**, 230-241 (2010).

Di Lorenzo, E. & Ohman, M. D. A. Double-integration hypothesis to explain ocean ecosystem response to climate forcing. *Proceedings of the National Academy of Sciences of the United States of America* **110(7)**, 2496-2499 (2013).

Hartmann D. L. Pacific sea surface temperature and the winter of 2014. *Geophys. Res. Lett*. **42**. 1894-1902 (2015).

Di Lorenzo, E. & Mantua, N. Multi-year persistence of the 2014/15 North Pacific marine heatwave. *Nature Clim Change* **11**, 1042-1048, (2016).

Joh, Y. & Di Lorenzo, E. Increasing coupling between NPGO and PDO leads to prolonged marine heatwaves in the Northeast Pacific. *Geophys. Res. Lett*, **44**, 11,663-11,671 (2017).

Trenberth, K. E., Branstator, G. W., Karoly, D., Kumar, A., Lau, N. C. & Ropelewski, C. Progress during TOGA in understanding and modeling global teleconnections associated with tropical sea surface temperatures. *J. Geophys. Res*. **103**, 14,291–14,324 (1998).

Liu, Z. & Alexander, M. Atmospheric bridge, oceanic tunnel, and global climatic teleconnections, *Rev. Geophys*. **45**, RG2005 (2007).

Qiu, B. Interannual variability of the Kuroshio Extension and its impact on the wintertime SST field. *J. Phys. Oceanogr*. **30**, 1486–1502 (2000).

Vivier, F., Kelly, K. A. & Thompson, L. A. Heat budget in the Kuroshio Extension region: 1993–99. *J. Phys. Oceanogr*. **32**, 3436–3454 (2002).

Scott, R. B. & Qiu, B. Predictability of SST in a Stochastic Climate Model and Its Application to the Kuroshio Extension Region. *J. Climate* **16**, 312-322 (2003).

Xue, H., Bane Jr., J. M. & Goodman, L. M. Modification of the Gulf Stream through strong air–sea interactions in winter: Observations and numerical simulations. *J. Phys. Oceanogr*. **25**, 533–557 (1995).

Seager, R., Kushnir, Y., Naik, N. H., Cane, M. A. & Miller, J. Wind-driven shifts in the latitude of the Kuroshio–Oyashio Extension and generation of SST anomalies on decadal timescales. *J. Climate* **14**, 4249–4265. (2001).

Chhak, K.C., Di Lorenzo E., Schneider, N., & Cummins, P. F. Forcing of Low-Frequency Ocean Variability in the Northeast Pacific. *J. Climate* **22**,1255-1276 (2009).

Alexander, M. A. & Deser, C. A. Mechanism for the Recurrence of wintertime midlatitude SST anomalies. *J. Phys. Oceanogr*. **25**, 122-137 (1995).

Qiu, B. Kuroshio Extension variability and forcing of the Pacific decadal oscillations: Responses and potential feedback. *J. Phys. Oceanogr*. **33**, 2465–2482 (2003).

Qiu, B., Schneider, N. & Chen, S. Coupled decadal variability in the North Pacific: An observationally constrained idealized model. *J. Climate* **20**, 3602–3620 (2007).

Andres, M. *et al*. Manifestation of the Pacific Decadal Oscillation in the Kuroshio. *Geophys. Res. Lett*. **36**, L16602 (2009).

Ceballos, L., Di Lorenzo, E., Hoyos, C. D. Schneider, N. & Taguchi, B. North Pacific Gyre Oscillation synchronizes climate variability in the eastern and western boundary current systems. *J. Climate* **22**, 5163–5174 (2009).

Newman, M. *et al*., The Pacific Decadal Oscillation, Revisited. *J. Climate* **29**, 4399-4427 (2016).

Cobb, K. M. *et al*. Highly Variable El Nino-Southern Oscillation Throughout the Holocene. *Science* **339(6115)**, 67-70 (2003).

Nurhati, I. S., Cobb, K. M., & Di Lorenzo, E. Decadal-Scale SST and Salinity Variations in the Central Tropical Pacific: Signatures of Natural and Anthropogenic Climate Change. *J. Climate* **24(13),** 3294-3308 (2011).

Sullivan, A. Luo, J. J., Hirst, A. C., Bi, D., Cai, W. & He, J. Robust contribution of decadal anomalies to the frequency of central-Pacific El Nino. *Scientific Reports* **6**, 38540 (2016).

Miller, A. J., Cayan, D. R. & White, W. B. A westward intensified decadal change in the North Pacific thermocline and gyre-scale circulation. *J. Climate* **11**, 3112–3127 (1998).

Schneider, N. & Miller, A. J. Predicting western North Pacific Ocean climate. *J. Climate* **14**, 3997–4002 (2001).

Taguchi, B., Xie, S. P., Schneider, N., Nonaka, M., Sasaki, H. & Sasai, Y. Decadal variability of the Kuroshio Extension: Observations and an eddy-resolving model hindcast. *J. Climate* **20**, 2357–2377 (2007).

Sasaki, Y. N., Minobe, S. & Schneider, N. Decadal response of the Kuroshio Extension jet to Rossby waves: Observation and thin-jet theory. *J. Phys. Oceanogr*. **43**, 442–456. (2013).

Qiu, B., Chen, S. & Schneider, N. Coupled decadal prediction of the dynamic state of the Kuroshio Extension System. *J. Climate* **27**, 1751-1764 (2014).

Kwon, Y. O, Alenxader, M. A., Bond, N. A., Frankignoul, C., Nakamura, H., Qui, B. & Thompson, L. Role of the Gulf Stream and Kuroshio–Oyashio systems in large-scale atmosphere–ocean interaction: A review. *J. Climate* **23**, 3249–3281 (2010).

Nakamura, H., Sampe, T., Tanimoto, Y. & Shimpo, A. Observed associations among storm tracks, jet streams and midlatitude oceanic fronts. Earth's Climate: The Ocean-Atmosphere Interaction, *Geophys. Monogr*. **147**, Amer. Geophys. Union, 329–346. (2004).

Taguchi, B., Nakamura, H., Nonaka, M. & Xie, S. P. Influences of the Kuroshio/Oyashio Extensions on air–sea heat exchanges and storm-track activity as revealed in regional atmospheric model simulations for the 2003/04 cold season. *J. Climate* **22**, 6536–6560 (2009).

Fankignoual, C., Sennechael, N., Kwon, Y. O. & Alexander, M. A. Influence of the meridional shifts of the Kuroshio and the Oyashio Extensions on the atmospheric circulation. *J. Climate* **24**, 762–777 (2010).

Na, H., Kim, K. Y., Minobe, S. & Sasaki, Y. N. Interannual to Decadal Variability of the Upper-Ocean Heat Content in the Western North Pacific and Its Relationship to Oceanic and Atmospheric Variability. *J. Climate* **31**, 5107-5125 (2018).

Miller, A. J., Chai, F., Chiba, S., Moisan, J. R. & Neilson, D. J. Decadal-scale climate and ecosystem interactions in the North Pacific Ocean. *J. Oceanogr*. **60**, 163–188 (2004).

Deser, C., Thomas, R. & Peng, S. The transient atmospheric circulation response to North Atlantic SST and sea ice anomalies. *J. Climate* **20**, 4751–4767 (2007).

Taguchi, B., *et al*. Seasonal evolutions of atmospheric response to decadal SST anomalies in the North Pacific subarctic frontal zone: Observations and a coupled model simulation. *J. Climate* **25**, 111–139 (2012).

Reverald A. *et al*. Influence of the Decadal Variability of the Kuroshio Extension on the Atmospheric Circulation in the Cold Season. *J. Climate* **29**, 2123–2144 (2004).

Chiang, J. C. H. & Vimont, D. J. Analogous Pacific and Atlantic meridional modes of tropical atmosphere-ocean variability. *J. Climate* **17**, 4143–4158 (2004).

Chang, P. *et al*. Pacific meridional mode and El Niño–southern oscillation. *Geophys. Res. Lett*. **34**, L16608 (2007).

Xie S. P. A dynamic ocean–atmosphere model of the tropical Atlantic decadal variability. *J. Climate* **12**, 64–70 (1999).

Vimont, D. J., Battisti, D. S. & Hirst, A. C. Footprinting: A seasonal connection between the Tropics and mid-latitudes. *Geophys. Res. Lett*. **28**, 3923–3926 (2001).

Vimont, D. J., Wallace J. M. & Battisti, D. S. The seasonal footprinting mechanism in the Pacific: Implications for ENSO. *J. Climate* **16**, 2668–2675 (2003).

Alexander, M. A., Vimont, D. J., Chang, P. & Scott, J. D. The impact of extratropical atmospheric variability on ENSO: Testing the seasonal footprinting mechanism using coupled model experiments. *J. Climate* **23**, 2885–2901 (2010).

Xie, S.-P. & Philander, S. G. H. A coupled ocean–atmosphere model of relevance to the ITCZ in the eastern Pacific. *Tellus* **46A**, 340–350 (1994).

Alexander, M. A., Blade, I., Newman, M., Lanzante, J. R., Lau, N. C. & Scott, J. D. The atmospheric bridge: the influence of ENSO teleconnections on air–sea interaction over the global oceans. *J. Climate* **15**, 2205–2231 (2002).

Di Lorenzo, E., *et al*. Nutrient and salinity decadal variations in the central and eastern North Pacific. *Geophys. Res. Lett*. **36**, (2009).

Di Lorenzo, E., *et al*. Central Pacific El Niño and decadal climate change in the North Pacific, *Nature Geoscience* (2010).

Furtado, J. C., Di Lorenzo, E., Anderson, B. T. & Schneider, N. Linkages between the North Pacific Oscillation and central tropical Pacific SSTs at low frequencies. *Clim. Dyn*. **39**, 2833-2846 (2012).

Di Lorenzo, E., Liguori, G., Schneider, N., Furtado, J. C., Anderson, B. T. & Alexander, M. A. ENSO and meridional modes: A null hypothesis for Pacific climate variability. *Geophys. Res. Lett*. **42**, 9440–9448 (2015).

Capatondi, A. *et al*. Understanding ENSO diversity. *Bull. Am. Meteorol. Soc*. **96**, 921–938 (2015).

Kilduff, D. P., Di Lorenzo, E., Botsford, L. W. & Teo, S. L. H. Changing central Pacific El Ninos reduce stability of North American salmon survival rates. *Proceedings of the National Academy of Sciences of the United States of America*, **112(35)**, 10962-10966 (2015).

Liguori, G. & Di Lorenzo, E. Meridional Modes and Increasing Pacific Decadal Variability Under Anthropogenic Forcing. *Geophys. Res. Lett*. **45**, 983-991 (2018).

Yasuda, I. Hydrographic structure and variability in the Kuroshio-Oyashio transition area. *J. Oceanogr*. **59**, 389–402 (2003).

Balmaseda MA, Vidard A, Anderson D. 2008. The ECMWF ORA-S3 ocean analysis system. *Mon. Weather Rev*. **136**, 3018–3034 (2008).

Carton, J. A., Chepurin, G. A. & Chen, L. SODA3: A New Ocean Climate Reanalysis. *J. Climate* **31**, 6967-6983 (2018)

Schaeffer, P., Pujol, M. I., Faugere, Y., Picot, N. & Guillot, A. New Mean Sea Surface CNES_CLS 2015 focusing on the use of geodetic missions of CryoSat-2 and Jason-1. Living Planet Symposium (2016).

Rayner, N. A. et al. Global analyses of sea surface temperature, sea ice, and night marine air temperature since the late nineteenth century. *J. Geophys. Res*. **108(D14)**, 4407 (2003).

Dee, D. P. *et al*. The ERA-Interim reanalysis: configuration and performance of the data assimilation system. *Meteorol. Soc*. **137**, 553–597 (2011).

Takahashi K., Montecinos A., Coubanova K., & Dewitte B. ENSO regimes: Reinterpreting the canonical and Modoki El Nino. *Geophys. Res. Lett*. **38**, L10704 (2011).

Stuecker M. F. Revisiting the Pacific Meridional Mode. *Scientific Reports* **8**, 3216 (2018).

Anderson, B. T., J. C. Furtado, E. Di Lorenzo, and D. J. S. Gianotti. Tracking the Pacific Decadal Precession, *J. Geophys. Res.-Atmos*., **122(6),** 3214-3227 (2017). doi:10.1002/2016jd025962.

Anderson, B. T., D. J. S. Gianotti, J. C. Furtado, and E. Di Lorenzo. A decadal precession of atmospheric pressures over the North Pacific, *Geophys. Res. Lett*., **43(8)**, 3921-3927 (2016) doi:10.1002/2016gl068206.

CHAPTER 4. ENHANCED INTERACTIONS BETWEEN KUROSHIO EXTENSION AND TROPICAL PACIFIC IN A CHANGING CLIMATE

This work is ready to be submitted to Scientific Reports.

Joh, Youngji, Di Lorenzo, E., Leo Sequeira, Benjamin P. Kirtman (2020)

4.1. Introduction

The Kuroshio Extension (KE) is a major component of the North Pacific western boundary current (WBC) system and characterized by prominent decadal fluctuations of sea surface height (SSH) and temperature (SST). These variations are considered to be modulated by mid-latitude air-sea interactions and known for generating and enhancing the decadal to interdecadal variability of the North Pacific coupled ocean-atmosphere system [*Pierce et al. 2001; Kwon and Deser 2007; Qiu 2003; Kwon et al., 2010; Na et al., 2018; Alexander and Deser 1995; Xue at al., 1995; Frankignual et al., 1997; Qiu et al., 2000; Nakamura and Kazmin 2003; Nakamura et al., 2004; Kelly et al., 2010*]. The KE is an *eastward-flowing oceanic jet* accompanied by large amplitude meanders, high level of mesoscale eddy variability, and linked to marked features of ocean circulation dynamics over the North Pacific [e.g., *Mizuno and White, 1983; Yasuda et al., 1992; Qiu, 1999; Ma et al, 2015*]. The pronounced spectral peak of KE SSH fluctuations (~10 years, Figure 4.1a) illustrates the substantial decadal variability of the North Pacific climate [*Qiu, 2003, 2007; Newman et al., 2016*]; thus, it is essential to identify the mechanisms behind the preferred decadal timescale of KE dynamic system.

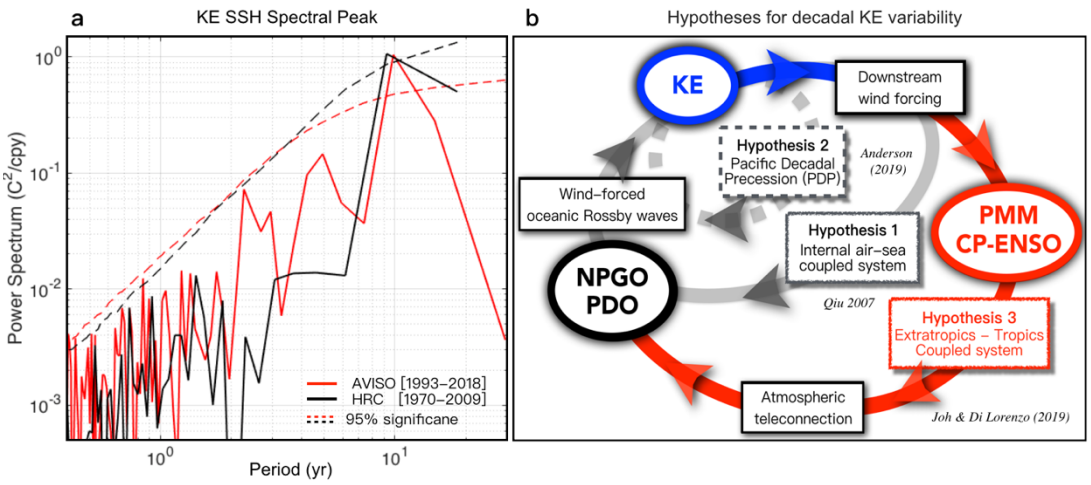

Figure 4.1. The preferred spectral peak of the KE index and diagram of the proposed hypothesis for generating decadal KE variability. (a) Power Spectrum as a function of the SSH-based KE index period (year) from the observations and HRC with 95% significance levels. (b) Internal air-sea coupled KE system (KE → KE downstream response → PDO/ NPGO → KE, hypothesis 1, *Qiu 2007*), Pacific Decadal Precession KE system (KE → north-south teleconnection phase → east-west teleconnection phase → KE, hypothesis 2, *Anderson 2019*), and extratropical-tropical coupled KE system (KE → KE downstream response → PMM/CP-ENSO → NPGO/PDO → KE, hypothesis 3, *Joh and Di Lorenzo 2019*).

Several hypotheses, based on empirical statistical analysis, have been proposed to explain the preferred decadal peak of KE variability (Figure 4.1b). Qiu (2007) has described the KE as an internal North Pacific air-sea coupled system, where the delayed atmospheric response of the downstream region can drive the wind-forced SSH signals over the central/eastern North Pacific. (Hypothesis 1 in Figure 4.1b). In Qiu's hypothesis, the KE downstream wind response is considered as the atmospheric forcing of KE that excites the oceanic Rossby waves switching the decadal KE phase. The follow-up studies demonstrated that KE's negative feedback could enhance the KE predictability on the decadal timescales by using a two-way wave adjustment plus wind feedback scenario [*Qiu 2007; Qiu et al., 2014*].

On the other hand, Anderson (2019) has linked the decadal KE dynamics to a new mode of quasi-decadal variability, the Pacific Decadal Precession (PDP; *Anderson et al., 2016; 2017*), which is characterized by a ~10yr counterclockwise progression of a dipole structure of the North Pacific atmosphere (Hypothesis 2 in Figure 4.1b). This hypothesis asserts that the evolution of the PDP mirrors a quasi-decadal signal in KE. The mesoscale KE variations are dynamically linked to the progression of large-scale atmospheric circulations through changes in zonal wind stress anomalies in the subpolar frontal zone (SPFZ). In hypothesis 2, the KE-PDP dynamics are represented as the migration of subsurface temperature and underlying meridional surface dipole circulations from the eastern to the western North Pacific. In contrast, in hypothesis 1, the midlatitude wind anomalies are described as the direct forcing of KE that triggers the westward propagating oceanic Rossby waves. More recently, Siqueira et al. (2020) suggest, based on observational estimates and ocean eddy-resolving coupled retrospective forecasts, that the near-decadal variability associated with PDP can lead to wind-forced SSH signals that affect the KE state with a time lag of about four years. They investigate the downstream atmospheric and oceanic response to the KE, showing that the dipole in wind stress curl anomalies in the eastern North Pacific does not effectively project on the forcing pattern for the KE variability but is more consistent with the Pacific Meridional Mode forcing by weakening the trade winds in the subtropical eastern Pacific [*Siqueira et al., 2020*].

While these two proposed hypotheses (Hypothesis 1 and 2 in Figure 4.1b) describe KE as the internal air-sea coupled system within the North Pacific, Joh and Di Lorenzo (2019) provide observational evidence showing that the preferred decadal timescale of KE may arise from the interaction between KE and central tropical Pacific (CP) variability, especially El Niño Southern Oscillation (ENSO) through Pacific Meridional Modes (PMM)

(Hypothesis 3 in Figure 4.1b). Through the available observations, this third hypothesis argues that the downstream atmospheric feedback can be interpreted as a slow nudging of the storm track (e.g., wind stress curl, 0-12 months timescale) that projects the atmospheric forcing of PMM and CP-ENSO. By pointing out an apparent difference in the observed spatial patterns of the atmospheric response and forcing of KE, the study hypothesizes that the ENSO atmospheric teleconnections have a key role in enhancing and evolving the KE downstream wind feedback into the large-scale wind forcing, which drives the SSH anomalies enough to excite the westward Rossby waves [e.g., *Deser and Blackmon 1995; Nakamura et al. 1997; Zhang et al. 1997; Seager 2001; Ceballos et al., 2009*].

Consistent with the above hypothesis, the Joh and Di Lorenzo work shows that the lead-lag correlation between the KE and the PMM/CP-ENSO indices exhibits a significant sinusoidal shape, where the interval between their correlation peaks correspond to the 10 years. Based on spatial and temporal evolutions of the KE variability using the observational data, Joh and Di Lorenzo suggest that KE might significantly covary with the tropics on decadal timescales, giving rise to the preferred spectral peak of KE. To provide further support for this observed extratropical-tropical coupled KE system; however, additional analyses using numerical models and large number realizations of the climate system are required.

The objective of this study is to expand upon the observational findings reported in Joh and Di Lorenzo (2019) by investigating the extratropical-tropical coupled KE system represented in the numerical simulations (e.g., high-resolution (0.1°) coupled model, HRC) and empirical model ensembles (Linear Inverse Models, LIM). We first show strong agreement between the observations and HRC on the KE dynamics (e.g., time-scale, atmospheric response and forcing of KE) and consistent noticeable changes in the

interactions of KE and CP-ENSO under a warmer climate. To assess the significance of changes in the KE dynamics and the relation to the tropical Pacific, we compare the decadal statistics of KE before and after the mid-1980 by using reconstructed indices of KE and CP-ENSO in LIM ensembles. Describing the statistical changes in the KE dynamics system, we provide a discussion of the detection and attribution of significant changes in the decadal KE dynamics in a changing climate.

4.2. Data and Method

4.2.1. Model

This study uses monthly mean data of SSH, SST and wind stress curl from National Center for Atmospheric Research (NCAR) Community Climate System Model Version 4 (CCSM4) current-day climate simulation, which is composed of the Community Land Model (CLM), the Community Atmospheric Model (CAM), the Los Alamos Parallel Ocean Program (POP) ocean general circulation model, and the Community Ice Code (CICE) with exchanging the state information and fluxes via a coupler [*Gent* et al. *2011*]. We use a historical run, where the observational estimates of external forcing from 1941-2009 are employed in CAM-4.0 atmospheric model configured to 0.5° × 0.625° latitude/longitude grid. Specifically, following the climate of the 20th Century protocol of the Coupled Model Intercomparison Project version 5 (CMIP5; *Taylor et al., 2012*), the changing historical CO2 fluxes are applied at the air-sea interface are calculated at (6-h) intervals using state variables from the atmospheric model linearly interpolated onto the oceanic grid. The POP2 ocean model uses a tripolar ocean grid (c.f. Murray 1996) with a ~0.1° resolution that allows eddy formation and evolution [*Kirtman* et al., *2012; Kirtman* et al., *2017*].

4.2.2. Data

Observations for investigating the SSH-based KE variability are obtained by two different SSH dataset within the period between 1959 and 2018 from the European Centre for Medium-Range Weather Forecasts (ECMWF) Ocean Reanalysis System: ORA-S3 [1959-2009] [*Balmaseda et al., 2008*], Simple Ocean Data Assimilation (SODA) reanalysis version 3 [*Carton et al., 2018*], and satellite distributed by Archiving, Validation, and Interpretation of Satellite Oceanographic (AVISO) data [1993-2018] obtained from https://www.aviso.altimetry.fr/en/data/products/auxiliary-products/mss.html. To explore the KE variability at the air–sea interface, we use the monthly mean SST data [2° × 2°horizontal grid] of the National Oceanic and Atmospheric Administration Extended Reconstruction SST, version 3 (ERSST.v3) product [*Smith et al., 2008*] and zonal and meridional wind stress from European Centre for Medium-Range Weather Forecasts (ERA) reanalysis product [*Dee et al., 2011*]. All anomalies are constructed by removing the mean monthly climatology and linear trend at each grid point.

4.3 Results

4.3.1. Observed and simulated dynamics of KE variability

We first conduct a singular value decomposition (SVD) analysis to examine the KE atmospheric downstream response and atmospheric forcing of KE based on previous studies that documented the air-sea coupled KE system [*Frankignoul et al., 2011; Qiu, 2003; Taguchi et al., 2007; Ceballos et al., 2009; Qiu et al., 2014; Na et al., 2018*]. The SVD analysis identifies the coupled relationship between the KE SSH and mid-latitude wind anomalies as the response/forcing feedback by extracting the maximum covariability of two variables [e.g., *SSH and windstress curl; Bretherton et al., 1992; Wallace et al., 1992;*

Tootle and Piechota, 2006]. To determine each of the response and forcing pattern of KE, here we apply different time lead/lags of mid-latitude wind anomalies with the KE SSH anomalies [31°–36°N & 140°–165°E], following the schematic of Joh and Di Lorenzo (2019). For example, we use *1yr lagged* Northeast Pacific windstress curl [25°–50°N & 180°–120°W] for the response of KE to capture the persistent downstream atmospheric feedback, which is induced by a migration of extratropical storm tracks [*Qiu et al., 2014; Joh and Di Lorenzo*]. To detect the atmospheric forcing of KE however, we use *3yr leading* mid-latitude windstress curl [30°–50°N & 220°–120°W], which explains the westward-propagating Rossby waves that travel along the midlatitude North Pacific KE band through multi-years [*Miller et al., 1998; Deser et al., 1999; Seager et al., 2001; Schneider et al., 2002; Qiu 2003; Taguchi et al., 2007; Sasaki et al., 2013; Qiu et al., 2014*].

The leading SSH SVD mode clearly represents the well-known spatial patterns of KE variability (Figures 4.2a and 4.2d) and their time series are consistent with the original KE index (area-averaged SSHa in the KE region) (Figures 4.2c and 4.2f) [*Qiu et al., 2014*]. We note that in both the observations and HRC, the Curl SVD patterns reveal a clear difference in their spatial structures between the atmospheric response and forcing of KE (Figures 4.2b & 4.2h vs. 2d & 2k). Specifically, while the KE downstream wind stress response shows a dipole structure of curl anomalies limited in the Northeast Pacific region (Figures 4.2b and 4.2h), the wind forcing of the KE exhibits, rather the large-scale wind anomalies over the central North Pacific (Figures 4.2d and 4.2k). Consistent with the observed KE downstream curl response [*Frankignoul et al., 1994; Qiu et al., 2014; Na et al., 2018; Joh and Di Lorenzo 2019*], the Curl SVD mode (lagged) reflects the changes in Ekman pumping velocity field modulated by the KE-forced meridional shift of extratropical storm track [*Figures 2b and 2h; Qiu et al., 2014*]. The Curl SVD mode (leading), the forcing of KE,

however, shows the large-scale wind forcing over the entire KE band [30°-40°N], which is associated with the internal atmospheric modes of the North Pacific (e.g., Aleutian Low or North Pacific Oscillation) as described in many previous studies [*Frankignoul et al. 1997; Miller et al. 1998; Deser et al. 1999; Schneider et al. 2002; Qiu and Chen 2005; Taguchi et al. 2007*]. The overall similarity of the SVD results between the observations (Figures 4.2a-f) and HRC (Figures 4.2g-l) confirms that the HRC captures not only the observed KE preferred time scale ~10yr (Figure 4.1a), but also the realistic air-sea coupled KE dynamics by reproducing the observed atmospheric response and forcing of KE reasonably well.

Consistent with the observational findings reported by Joh and Di Lorenzo (2019), HRC also captures the interaction between KE and CP-ENSO. Correlation maps between the KE index and lagged SST/Curl/SSH anomalies from HRC (Supplementary Figures S4.1) support that (1) the KE atmospheric downstream feedback can evolve into the atmospheric forcing that projects PMM and CP-ENSO (Figures S4.1-a) and (2) the resulting tropical atmospheric teleconnections enhance the North Pacific wind forcing that drives the oceanic Rossby waves (Figures S4.1-b and c). Specifically, the strong development of tropical warm SST (Figures S4.1-a) and the corresponding robust SSH anomalies over the central North Pacific (Figures S4.1-c) at lag 60 months, indicates that tropical processes (e.g., forced atmospheric stationary Rossby waves) affect the evolution of the KE system. Supporting the observational findings of Joh and Di Lorenzo (2019), we show that coupled climate model simulation also captures the observed extratropical-tropical coupled KE system and can explain the decadal transition of KE related to its preferred time scale.

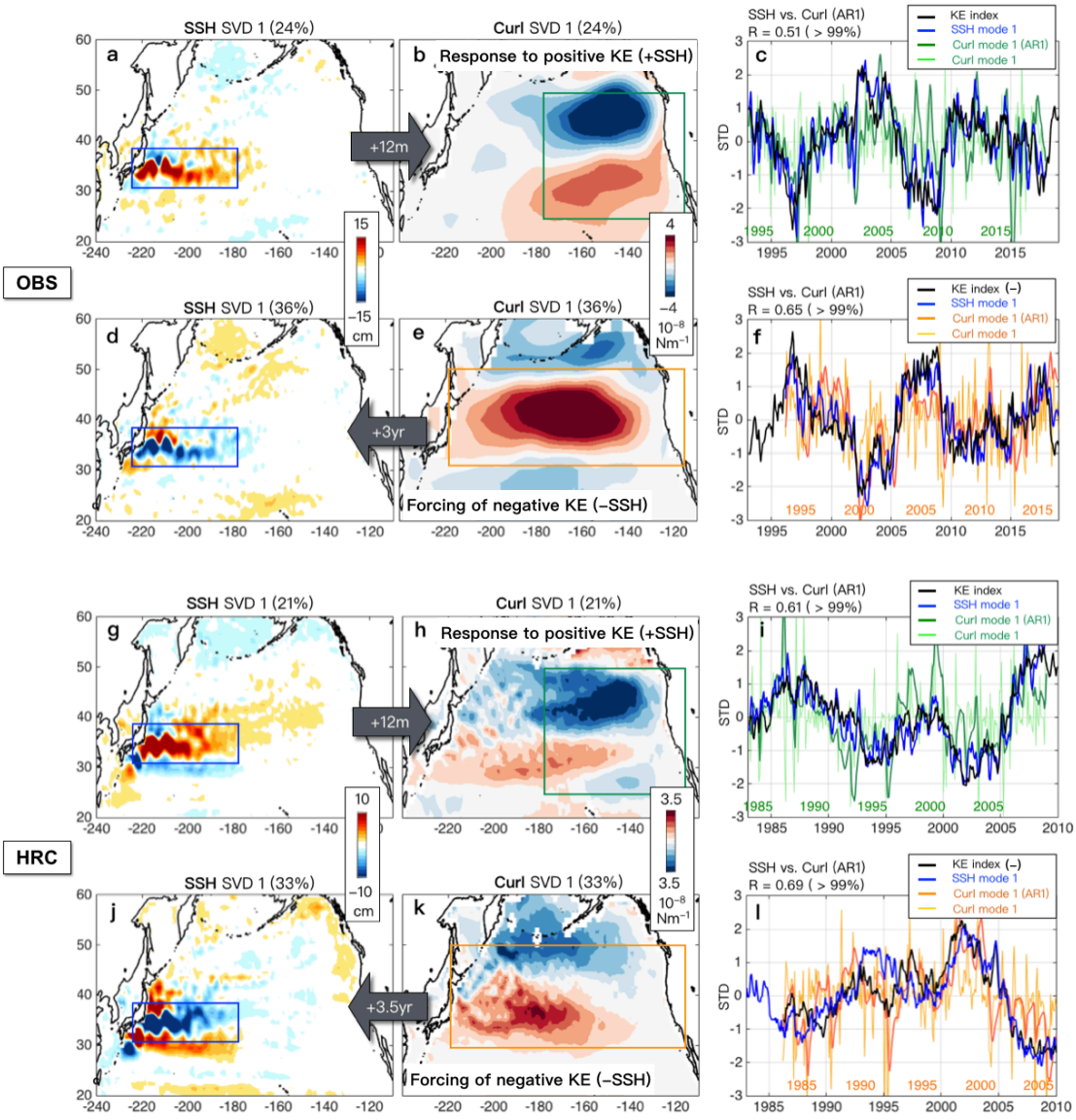

Figure 4.2. Spatial and temporal patterns of KE dynamics (KE atmospheric response and forcing of KE) based on singular value decomposition (SVD) analysis between KE SSH and midlatitude windstress curl with lead/lag times. Patterns of the leading SVD mode between the observed (a) SSH over the KE region (blue box) and (b) 12mon-lagged Curl over the downstream region (green box) for the recent period. (c) The associated time series of corresponding SSH and SVD modes. (d-f) Same as in (a-f), but for with 42mon-leading Curl. The same analysis was repeated with HRC in (g-i).

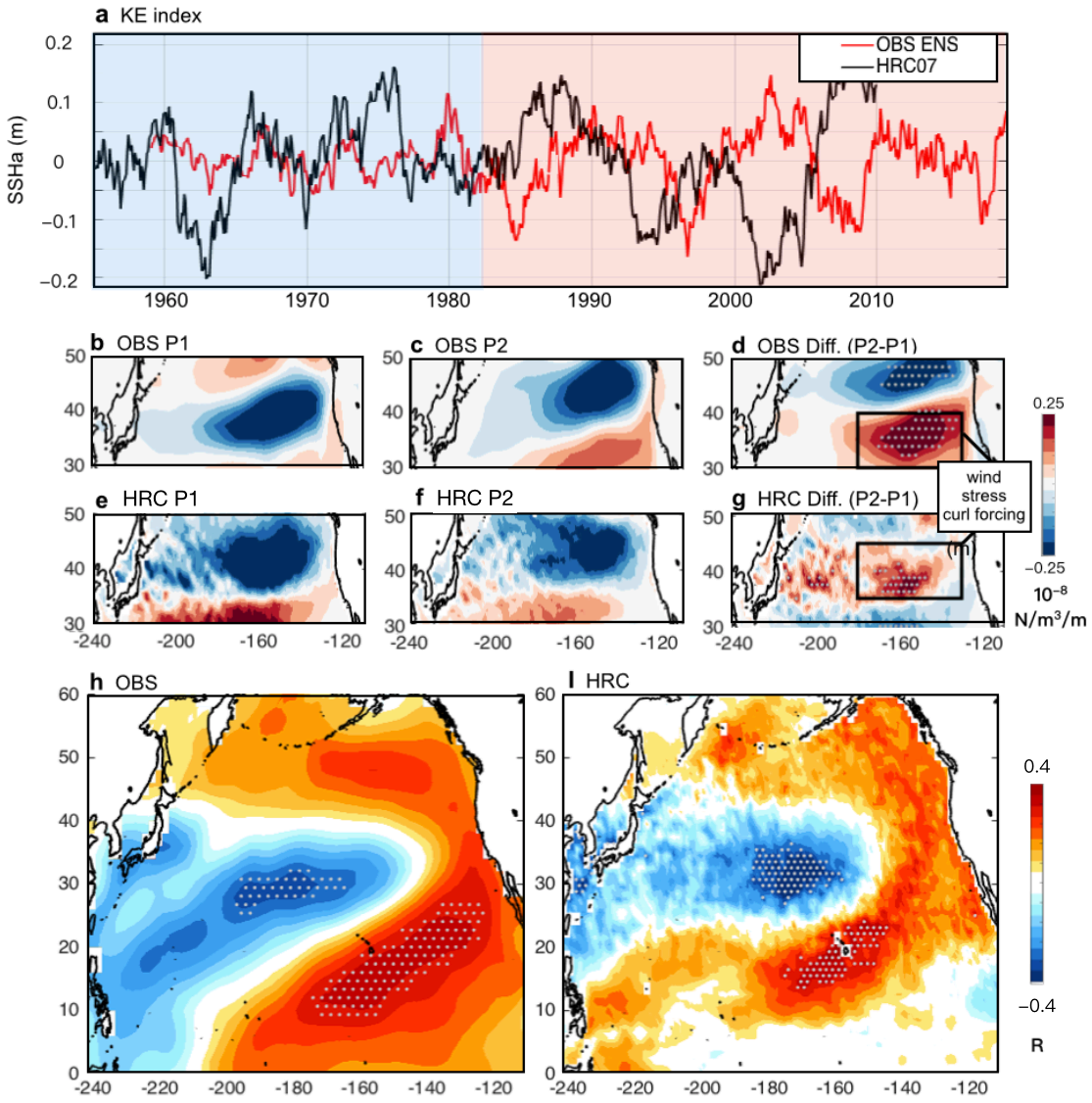

Figure 4.3. Observed and simulated KE SSH fluctuations and changes in the KE atmospheric downstream response from the P1 to P2 (a) Computed KE index using area-averaged SSH anomalies over the KE region from the observational ensembles (ORA and AVISO, red line) and HRC (historical run-no assimilation, black line). Patterns of leading Curl SVD mode between KE SSH and midlatitude Curl (12mon-lagged) for the (b) Period 1 and (c) Period 2 and its difference (Period 2-Period 1, recent-previous) in observations. (e-g) Same as (b-d), but for in HRC. Correlation map of SST anomalies with the timeseries of subtropical wind forcing (black box of d and g) that is computed by regressing the target patterns (black box of d and g) onto the original windstress curl anomalies.

4.3.2. Hypothesis for modification of KE variability

Given a substantial agreement between the observed and simulated dynamics of the KE, we note some changes in characteristics of the KE variability during the recent decades. First, there is strong decadal fluctuations of KE with the preferred spectral peak ~10 yr which only appears after the mid-1980 (Figure 4.3a, note that HRC is not a retrospective forecast, but a free-running simulation with no assimilation) and the interaction between the KE and tropical Pacific has been significantly enhanced both in the observations and HRC. Importantly, we find that the strength of interaction between KE and CP-ENSO depends on the period of time under investigation, with the more recent decades showing an increase in their coupling (Supplementary Figures S4.3). Consistent with this, the spatial evolution of the KE atmospheric/oceanic response after 1980 in HRC (Figure S4.1) shows a clear transition from the KE state to the PMM/CP-ENSO mode with the stronger amplitudes compared to those during earlier decades (Figures S4.2).

To assess whether the above temporal differences in characteristics of KE system are a matter of chance or are statistically significant, we employ Linear Inverse Model (LIM), which can extract dynamical properties of the climate system from its observed behaviors and statistics [e.g., *Penland 1989, 1996; Penland and Matrosova 1995; DelSole and Hou 1999; Newman et al. 2003a; Alexander et al., 2008*]. Linear inverse modeling describes the relevant dynamics as the form of a linear stochastic differential equation that consists of the state of the system, the evolution operator, and the stationary white noise.

Here we construct LIMs based on a reduced space of empirical orthogonal functions (EOFs) with the corresponding principal components (PCs) as the state vectors. To examine the interaction between KE and CP-ENSO in LIM, we define the state vectors using the basin-scale SSH [31°–36°N & 140°–165°E] and SST [20°S–60°N & 120°E–80°W] anomalies

to reconstruct the KE and CP-ENSO indices. We retain 8∼15 leading EOFs (vary depending on different LIM sets), which explain more than 70% of the total variance. To compare the KE variability between before and after the mid-1980, we set two 25-year time-periods as 1960-1984 (previous period, P1) and 1985-2019 (recent period, P2), then construct LIMs separately for P1 and for P2. To build each LIM set, we first determine the system dynamics and stochastic forcing, which capture the observed spatial/temporal characteristics of KE and CP-ENSO for each P1 and P2 (Supplementary Figures S4.4). We next integrate each period of LIM for 25,000 years respectively, following the method in Penland and Matrosova (1994), then divide the output into 1000 25-year segments as the large ensembles for each P1 and P2. Those 1000 25-year segments are used to estimate the sampling uncertainties for the statistical significance test. We repeat the same LIM construction using HRC, but with 20-year time-periods of P1 (1960-1979) and P2 (1980-2009) (Supplementary Figures S4.5). We hereafter refer to LIMs with the different dataset as *OLIM* for LIM using observations and *HLIM* for LIM using HRC and define each period of OLIM and HLIM as *OLIM(P1)* and *HLIM(P1)* for the *earlier period (P1)* and *OLIM(P2)* and *HLIM(P2)* for the *recent period (P2)*. We use output of these several different LIMs to investigate and compare the KE dynamic between the two periods. As we show below, the statistics of KE in P1 (e.g., OLIM(P1) and HLIM(P1)) are not consistent with those in P2 (e.g., OLIM(P2) and HLIM(P2)) (e.g., sampling distribution), suggesting that the KE variability is stationary (i.e., rejecting the null hypothesis). As additional support for rejecting this null hypothesis, we also describe below that the inconsistent temporal characteristic of the KE index and the changes in the coupling of KE and PMM/CP-ENSO is also detected HRC (see also Supplementary Figures S4.1-3).

4.3.3. Statistical changes in the KE variability

A comparison of the lead-lag correlations of KE and CP-ENSO indices between OLIM(P1) vs. OLIM(P2) and HLIM(P1) vs. HLIM(P2) indicates apparent differences in the relationship between KE and the tropics for the two different periods (Figure 4.4). While OLIM(P2) and HLIM(P2) show a significant sinusoidal shape of correlation function distribution (Figures 4b), OLIM(P1) and HLIM(P1) exhibit a nearly flat distribution (Figure 4a). We note that the time interval of recurring peaks in the lead-lag correlation of OLIM(P2) and HLIM(P2) is consistent with the observed interval, which corresponds to ~10 years (Figure 4.4b).

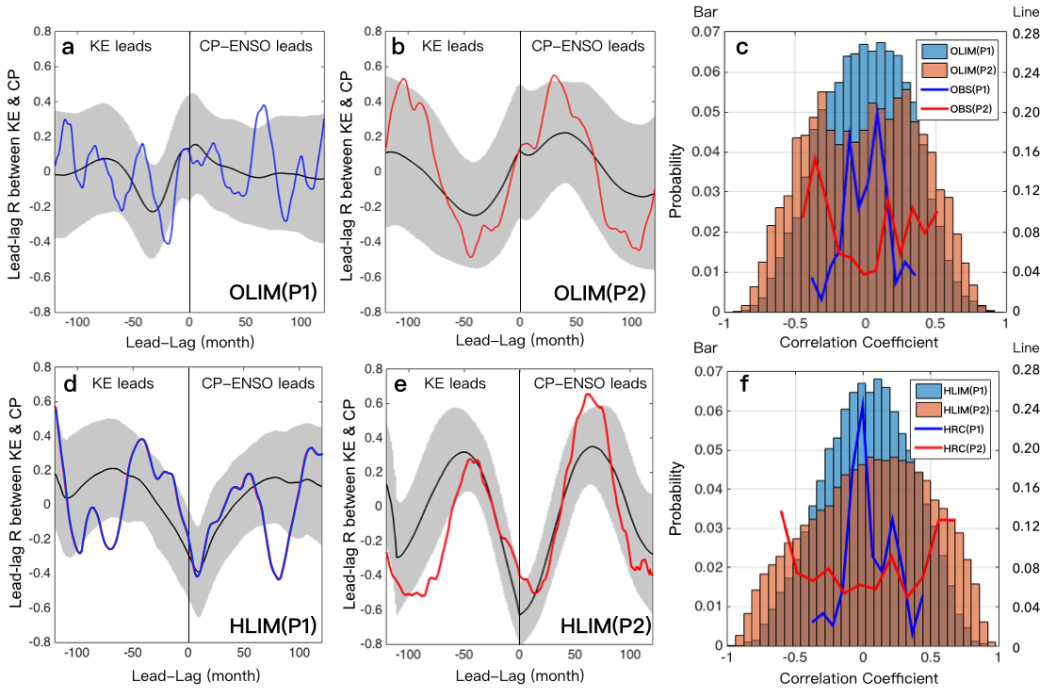

Figure 4.4. Changes in coupling between he KE and CP-ENSO from Period 1 to Period 2. Lead-lag correlation between the KE and CP-ENSO indices during the (a) P1 and (b) P2 in LIM constructed by observational SSH and SST (OLIM), where black and blue/red lines are each the ensemble mean and the observed correlation and shadings show plus and minus two standard deviation in the mean values. (c) Probability distribution function of the observed (lines) and reconstructed (bars) correlation coefficients of a and b for the P1 and P2. (d-e) Same as (a-c), but for LIM constructed by HRC SSH and SST (HLIM).

A power spectrum analysis of the KE index shows that the quasi-decadal peak corresponding to 10 years is dominant in both the OLIM(P2) and HLIM(P2) (Supplementary Figures 4.6). We suggest that this preferred KE spectral peak during P2 may arise from the decadal interaction with the tropical Pacific. A sampling distribution of the lead-lag correlations of KE and CP-ENSO between P1 and P2 (Figure 4.4c) show the noticeable difference in their shape and confirms that there has been a change in the frequencies of the lead-lag correlation. For example, the observed lead-lag correlations between the KE and CP-ENSO indices (lines in Figure 4.4c), and the probability density functions of the reconstructed correlation in OLIMs (bars in Figure 4.4c) show that OLIM(P2) has a fat-tailed distribution. This indicates that the higher correlations (e.g., stronger coupling) are more frequent in P2. We find the similar results when we repeat the same analysis using HLIMs (Figures 4.4d-f). Combining the consistent results from OLIMs (Figures 4.4a-c) and HLIMs (Figures 4.4d-f) thus, we suggest that the KE variability between P1 and P2 are different from each other (i.e., we reject the null hypothesis that the differences are merely sampling issues).

Before concluding, however, we note a non-negligible difference between the observations and HRC regarding the time-scale of their lead-lag correlations during P2 (compare Figure 4.4b vs. 4.4e). For example, in the observations, KE is accompanied by the neutral phase of ENSO at lag 0 yr and drives CP-ENSO at lag ~3 yrs (Figure 4.4b), whereas in HRC, KE is concurrently in the La Nina phase and induces CP-ENSO at lag ~5 yrs (Figure 4.4e). The question, therefore, is whether this difference is associated with a variation in LIM realizations or should be considered as model error in HRC. Because the LIM's dynamical operator is fixed, the ensemble spread results only from different initial conditions, which is comparable to internally generated noise forcing [*Capotondi and*

Sardeshmukh, 2017]. In nature, this atmospheric noise forcing can generate not only interannual fluctuations, but also lower frequency variations by stochastic excitation of climate variability and following red noise process (e.g., PMM and ENSO, *Chiang and Vimont, 2004; Lian et al., 2014; Di Lorenzo et al., 2015*). Thus, identifying the relative importance of stochastic forcing in the decadal KE variability is essential to assess the uncertainty and predictability of the KE dynamic system. In the next section, we examine the role of this noise component in LIM, which is intrinsically generated in the stochastic differential equation, and investigate LIM ensemble spread in the coupling between KE and CP-ENSO.

4.3.4. Role of stochastic forcing on decadal KE dynamics

Comparing across the individual realization in LIMs allows for understanding how the observed extratropical-tropical KE system can vary in the same dynamical system (e.g., the fixed dynamical operator of LIM). In other words, can the difference between the observations and HRC during P2 noted in Fig. 4.4b and 4.4e be captured within the same dynamical operator? To investigate whether the same dynamical operator of OLIM(P2) can reproduce both the observed and simulated characteristics of the lead-lag correlations of KE and CP-ENSO, we subsample two sets of 50 members out of 1000 members of OLIM(P2) whose correlations are the best fit to each observed (red lined in Figure 4.4b) and simulated (red lined in Figure 4.4e) lead-lag correlations, as $OLIM_{OBS}$ and $OLIM_{HRC}$ respectively. To find the subset $OLIM_{OBS}$ ($OLIM_{HRC}$), we compute the correlation of the observed (simulated) and reconstructed lead-lag correlation between the KE and CP-ENSO indices in each member of OLIM(P2), and select the top 50 members based on the computed correlations and show their lead-lag correlation between the KE and CP-ENSO indices in Figure 4.5a

(Figure 4.5b). Because OLIM(P2) is constructed based on observational estimates of SSH and SST anomalies to capture the observed characteristics of KE, it is not surprising that the ensemble spread of $OLIM_{HRC}$ is much larger compared to that of $OLIM_{OBS}$, that is the best fit 50 ensemble members do not fit as well as in OLIM(P2). However, we note that $OLIM_{HRC}$ can capture the lead-lag correlations between KE and CP-ENSO that significantly overlapped with that of HRC (Figures 4.5b). Conversely, using HLIM subsets (Supplementary Figures 4.7c-d), we find the similar results revealing that the dynamic system of HLIM can also represent both different types of coupled KE system shown in the observations and HRC during P2. Taken together, we suggest that the difference in the lead-lag correlation of KE and CP-ENSO between the observations and HRC (Figures 4.4b vs. 4.4e) might be due to the sampling and that the KE behaviors can be irregular and dynamically vary depending on the noise component in the climate system. Simply put, the differences between P1 and P2 are not sampling and are attributed to changes in the KE system, whereas the difference between HRC and observational estimates may indeed be due to sampling.

Supporting the above findings, the spatial evolutions of KE oceanic response from $OLIM_{OBS}$ (Figure 4.5d) and $OLIM_{HRC}$ (Figure 4.5e) exhibit the similar progression of SST (KE oceanic response) shown in the entire OLIM (Supplementary Figure S4.8), where the KE SST pattern becomes the PMM-like oceanic signature and further ENSO-like pattern. Although there is obvious temporal difference of the KE SST progression between the observations (KE → CP-ENSO (~3 yrs) in Figures 4.5c-d) and HRC (KE → CP-ENSO (~5 yrs) in Figures 4.5e-f), this might simply be associated with variation in the concurrent KE-ENSO state that can affect a transition from KE to ENSO. Specifically, while in the observations and $OLIM_{OBS}$, the KE SST at lag 2 months (Figures 4.5c) exhibits the west-east

dipole SST anomalies over the tropics with the eastern Pacific La Nina signature, in $OLIM_{HRC}$ and HRC (Figures 4.5d-f), KE is accompanied by the broad cold SST anomalies extending from the west Pacific warm pool to the South American coast, resembling the central Pacific La Nina mode. Depending on which tropical SST mode is accompanied by KE, temporal interaction between KE and CP-ENSO can vary. The overall similarity between $OLIM_{OBS}$ and $OLIM_{HRC}$ in the KE SST progression supports the argument that the observations and HRC can be considered as any individual ensemble member generated in the same KE dynamical system.

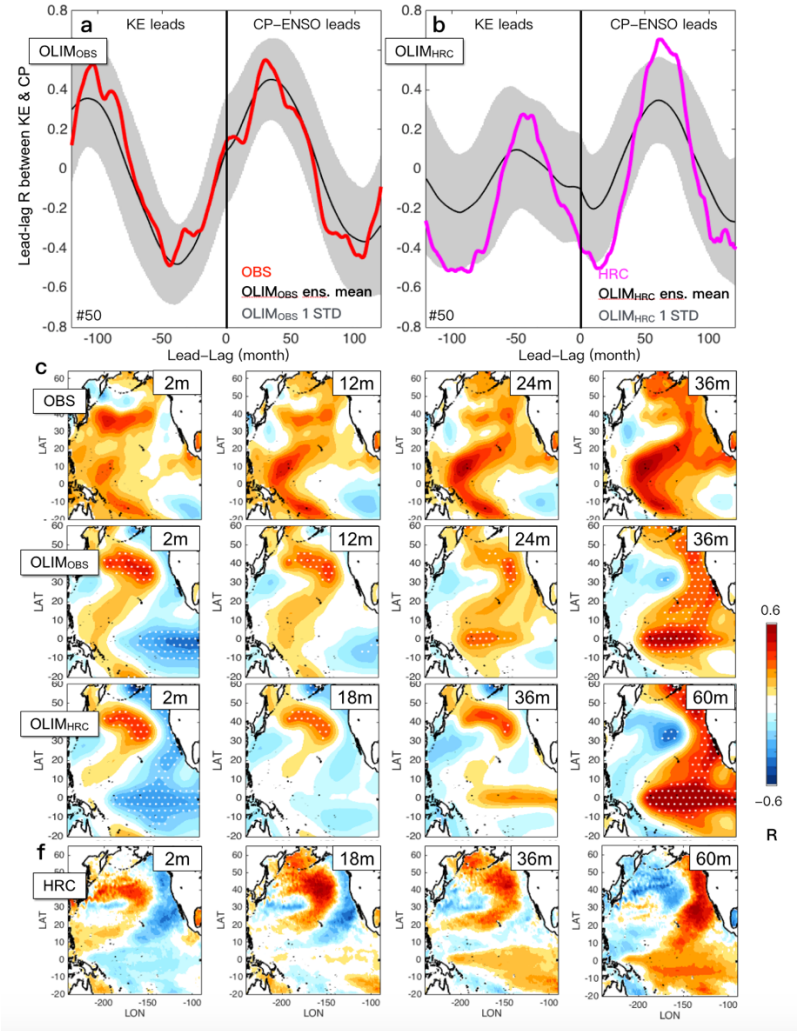

Figure 5. Variation of the extratropical-tropical KE system in presence of stochastic noise forcing. 50-member subsets of OLIM(P2) that best fit to the (a) observed ($OLIM_{OBS}$) and (b)

simulated ($OLIM_{HRC}$) lead-lag correlation between the KE and CP-ENSO indices, where ensemble means and references are denoted as black and red/pink lines with the two standard-deviation confidence interval (shading) in $OLIM_{OBS}$ and $OLIM_{HRC}$ respectively. The dot indicates the grid whose signal is above 95% significance level based on the student t-test. SST progression of KE in the (c) observations, (d) $OLIM_{OBS}$, (e) $OLIM_{HRC}$, and (f) $OLIM_{HRC}$.

4.5. Summary and discussion

Through complementary analysis using observations, numerical simulations, and empirical dynamical models, this study explores the differences in the KE properties between before and after the mid-1980 (e.g., P1 vs. P2). Having shown that the decadal interaction between KE and CP-ENSO has become more robust in the recent period, we propose that the KE variability is not stationary and that these recent changes in the KE system may reflect a response an overall changing climate. We first note the contributions of changes in the background mean state (e.g., surface winds) KE system. A comparison of the KE downstream atmospheric response between P1 and P2 (Figures 4.3b/4.3e vs. Figures 4.3c/ 4.3f) shows that the dipole structure of wind stress curl over the Northeast Pacific has shifted towards the pole, and drives significantly stronger wind forcing in the KE band (31°-39°N) during P2 (Figures 4.3d and 4.3g) compared to P1.

As many previous studies have described, this subtropical wind forcing is linked to positive air-sea thermodynamic coupling known as the winds-evaporation-SST (WES) feedback [*Xie and Philander, 1998*]; thus, we suggest that the stronger KE wind stress feedback might induce the ENSO-favorable condition by preferentially projecting stronger PMM-like oceanic signatures onto the SST in the recent period (Figures 4.3h-i).

Consistent with the above findings, we also detect noticeable changes in the climatology of the surface winds (e.g., zonal wind), showing that the subtropical westerly winds have been significantly intensified after mid-1980, especially for the spring season

(Supplementary Figure S4.9). Considering that the mid-latitude stochastic atmospheric forcing can affect the ENSO via the seasonal footprinting mechanism [*Vimont et al., 2003*], it is plausible that the changes in the background climate might be dynamically linked to the enhanced interaction between KE and CP-ENSO by altering the KE downstream atmospheric response (e.g., latitudinal position of extratropical storm track). On the other hand, we cannot exclude the external forcing on the coupled KE dynamics and related background state, because previous studies have shown that the extratropical-tropical coupling is intensifying under anthropogenic forcing [e.g., *Di Lorenzo and Mantua, 2016; Joh and Di Lorenzo, 2017; Qiu et al., 2014; Kilduff et al., 2015; Liguori and Di Lorenzo., 2018*]. Specifically, the increasing link between the North Pacific ENSO precursor (e.g., North Pacific Oscillation) and ENSO under the enhanced greenhouse forcing [*Wang et al., 2013, 2014*] might be associated with the stronger coupling between KE and CP-ENSO. Therefore, how and how much the background mean state and the external forcing independently or/and jointly affect the decadal KE system should be further investigated, through appropriate modeling experiments (e.g., pre-industrial control vs. historical forcing).

4.6. Supporting Information

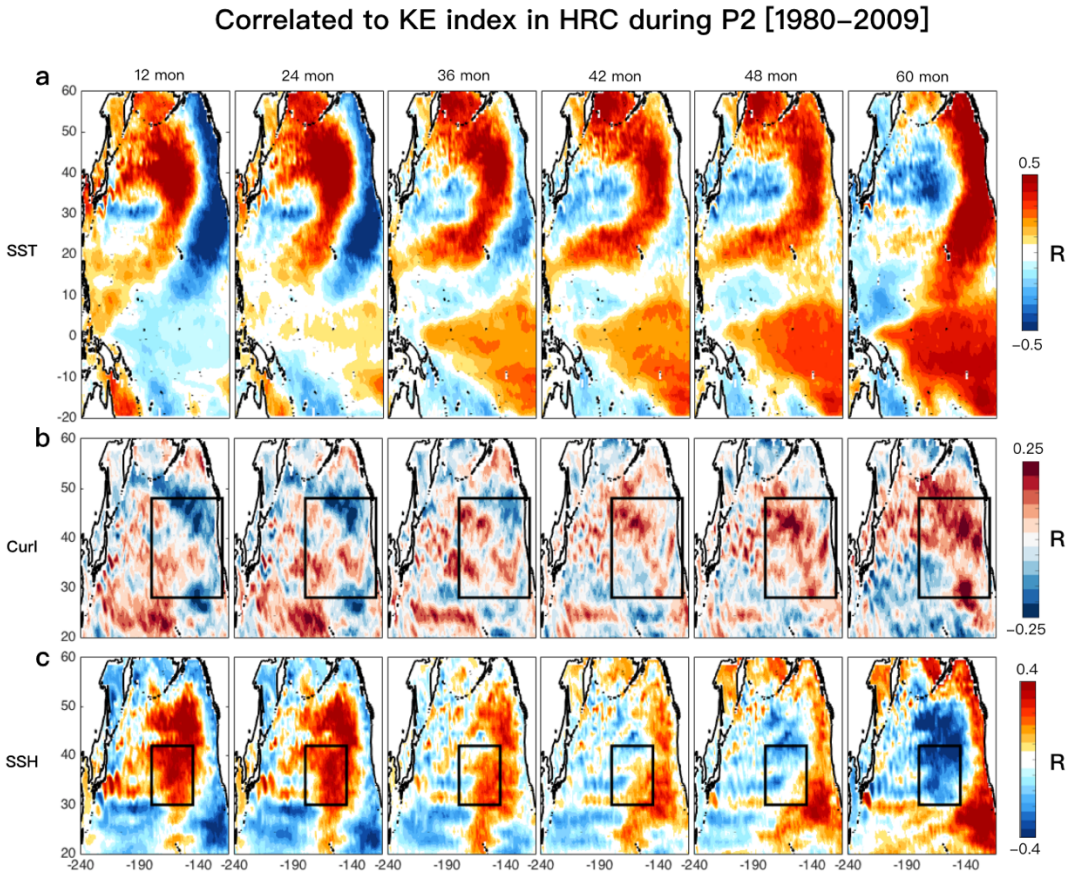

Figure S4.1. Spatial evolution of KE atmospheric/oceanic response. Correlation map between KE and (**a**) SST, (**b**) windstress curl, and (c) SSH anomalies at lag 12, 24, 36, 42, 48, and 60 months simulated in HRC during the recent period.

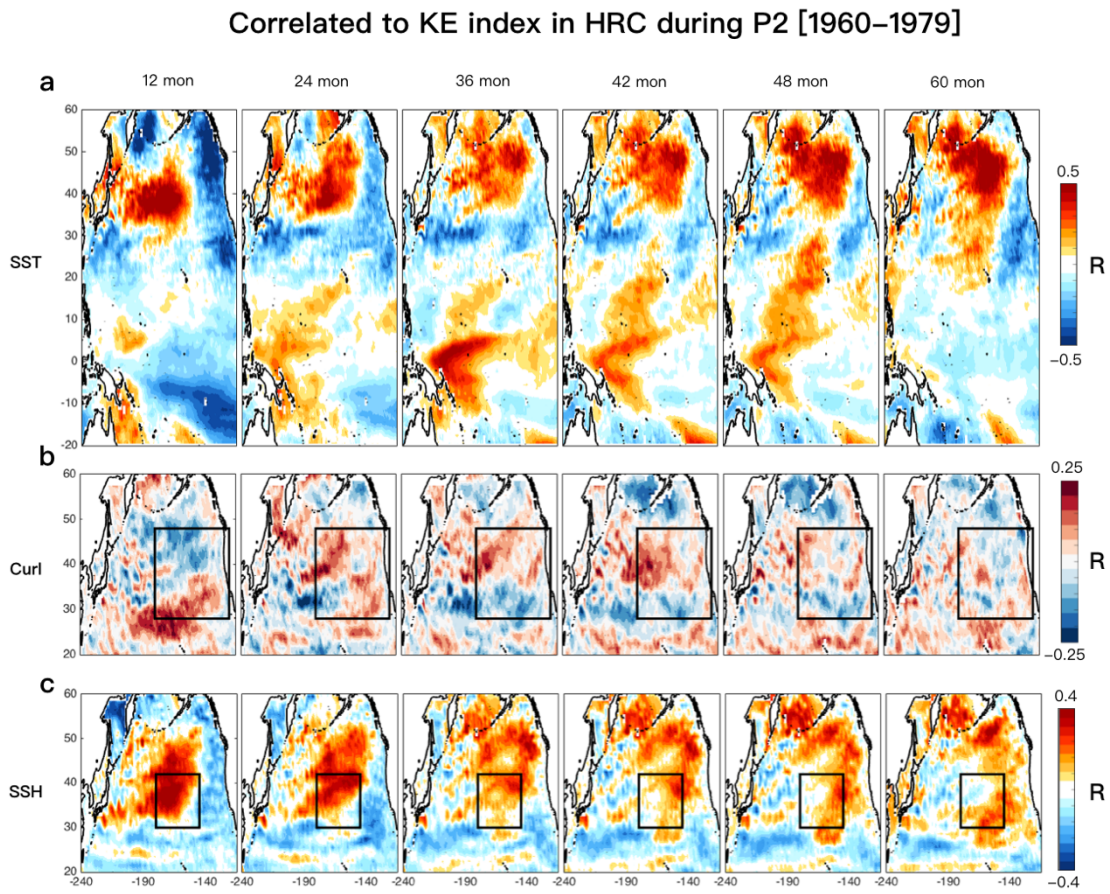

Figure S4.2. Spatial evolution of KE atmospheric/oceanic response. Correlation map between KE and (**a**) SST, (**b**) windstress curl, and (c) SSH anomalies at lag 12, 24, 36, 42, 48, and 60 months simulated in HRC during the previous period.

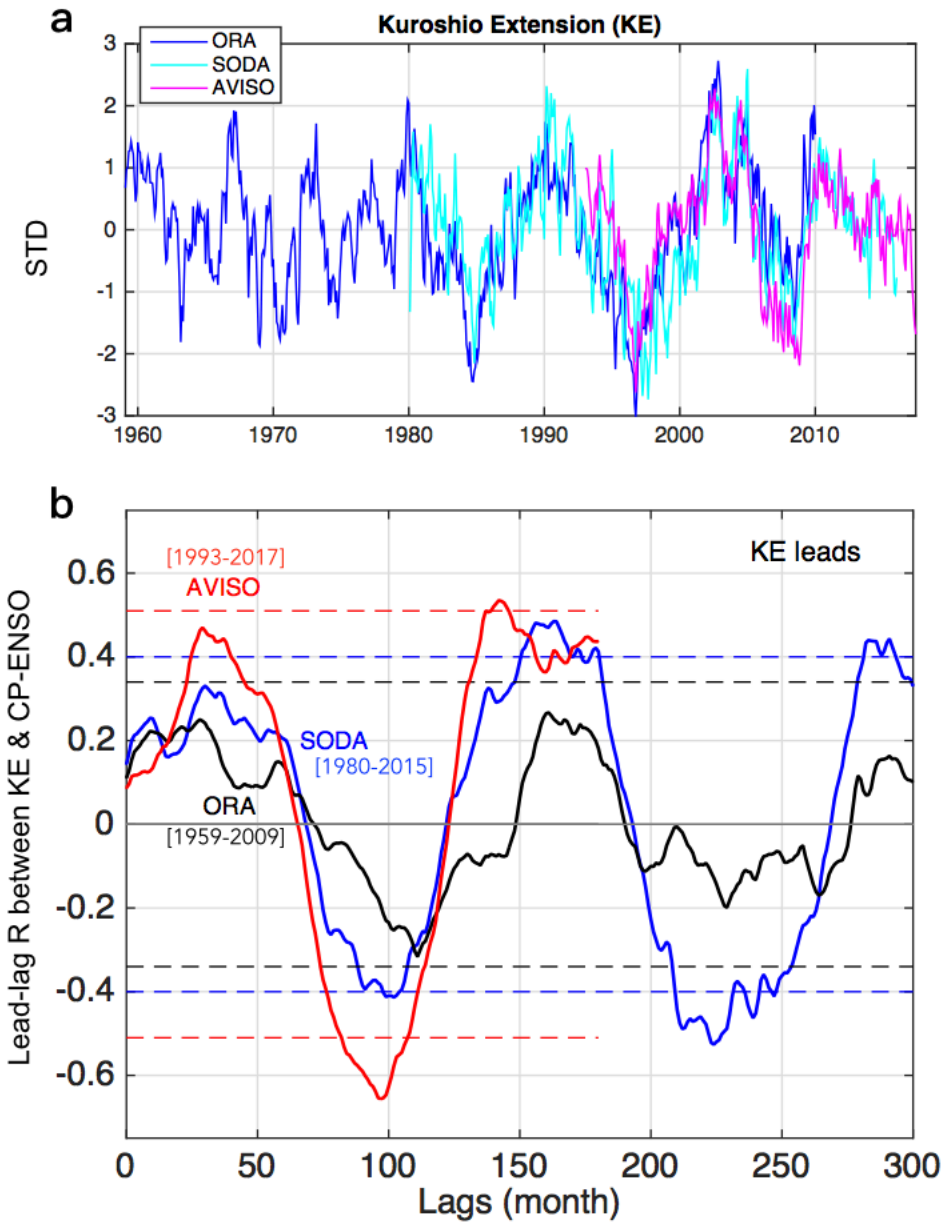

Figure S4.3. Changes in temporal characteristics of KE and the relation between KE and CP-ENSO. (a) Area-averaged SSH anomalies over the KE region [31°–36°N & 140°–165°E] from observational reanalysis data. (b) Lead-lag correlations between the KE and CP-ENSO indices in different time periods. The 95% confidence intervals for each period are denoted as dashed lines based on Monte-Carlo approach.

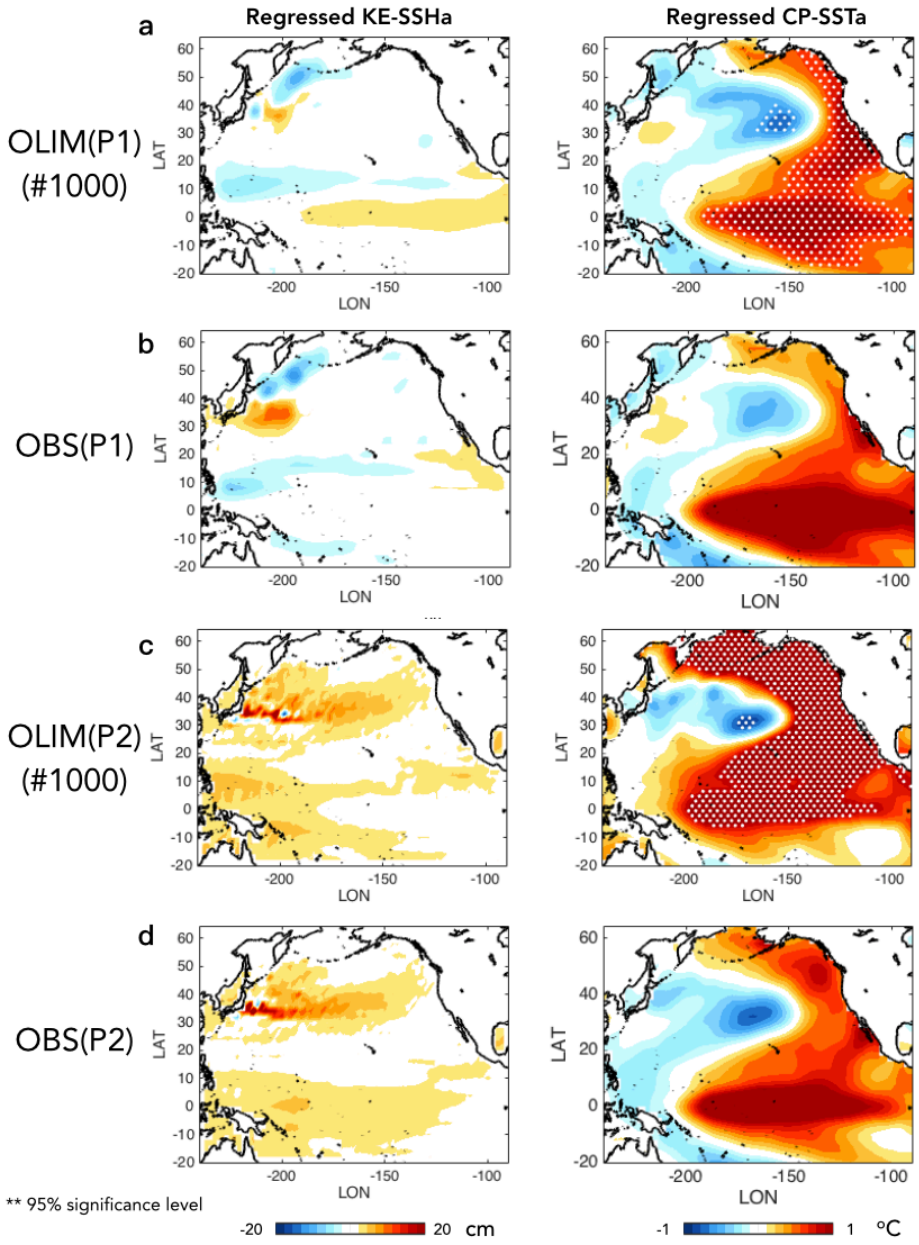

Figure S4.4. Spatial patterns of KE and CP-ENSO in OLIM and HRC. Regression of monthly SSH (left) and SST (right) anomalies onto the KE and CP-ENSO indices of (a) LIM ensemble mean and (b) observations for P1 and (c) LIM ensemble mean and (d) observations for P2. A dot symbol denotes the grid whose signal is significant at the 95% confidence level using a Monte-Carlo approach.

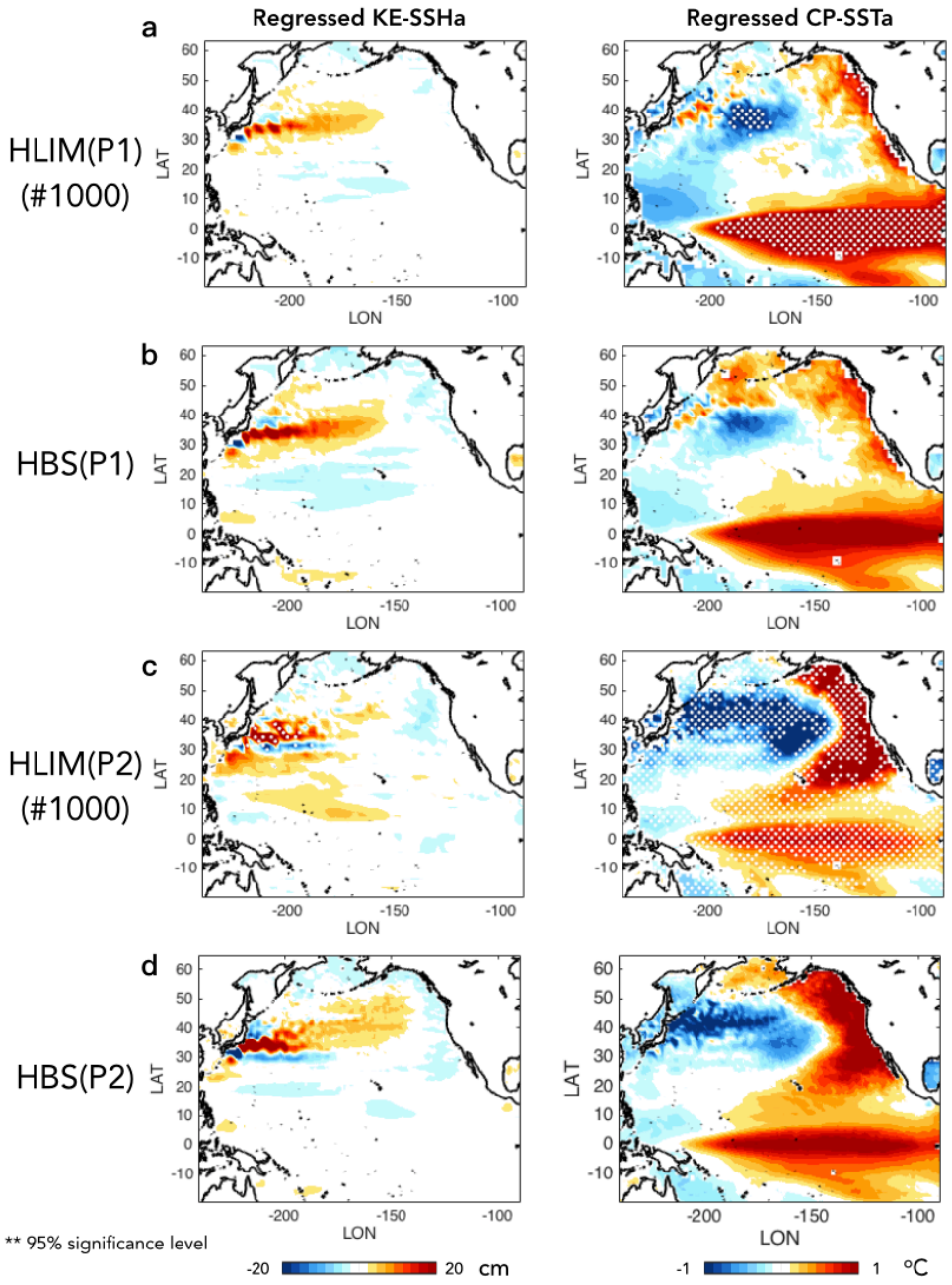

Figure S4.5. Spatial patterns of KE and CP-ENSO in HLIM and HRC. Regression of monthly SSH (left) and SST (right) anomalies onto the KE and CP-ENSO indices of (a) LIM ensemble mean and (b) HRC for P1 and (c) LIM ensemble mean and (d) HRC for P2. A dot symbol denotes the grid whose signal is significant at the 95% confidence level using a Monte-Carlo approach.

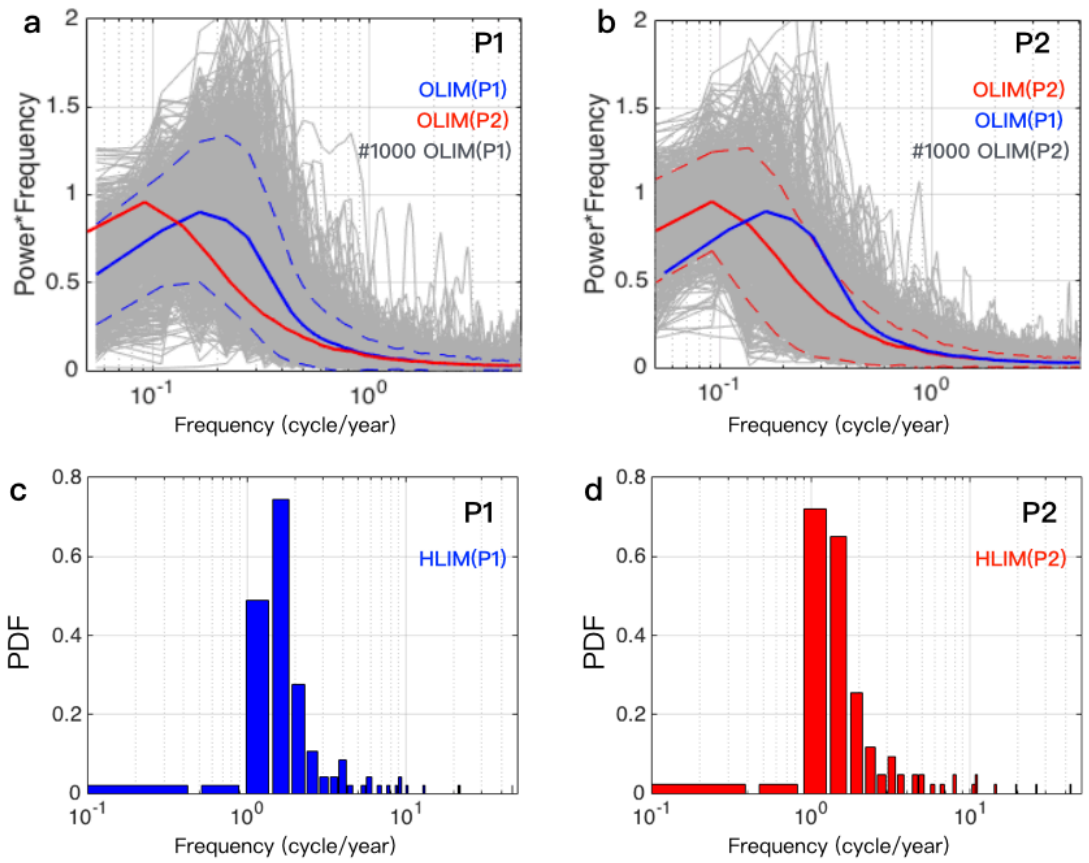

Figure S4.6. Changes in KE power spectra from P1 to P2. Spectra of the KE index for each 25 year segment (gray lines), their ensemble mean (blue for P1 and red for P2), and 10^{th} and 90^{th} percentiles (dotted red/blue line) of each spectral signal in of (a) OLIM(P1) and (b) OLIM(P2). Probability density functions of the power spectra of KE index in (c) HLIM(P1) and (d) HLIM(P2).

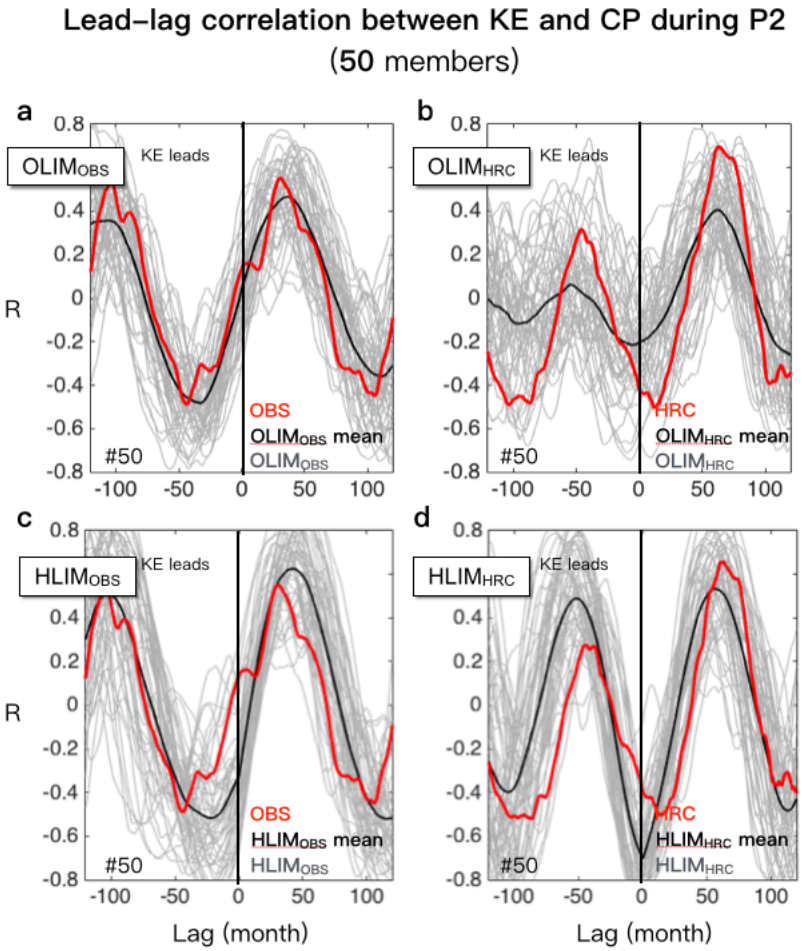

Figure S4.7. Variation in coupling between KE and CP-ENSO in the presence of stochastic noise forcing during the recent period. Lead-lag correlation between the KE and CP-ENSO indices of subsampled 50 LIM members whose correlation is best fit to (a) the observed one and HRC's from OLIMs. (c-d) Same as (a-b), but from HLIMs.

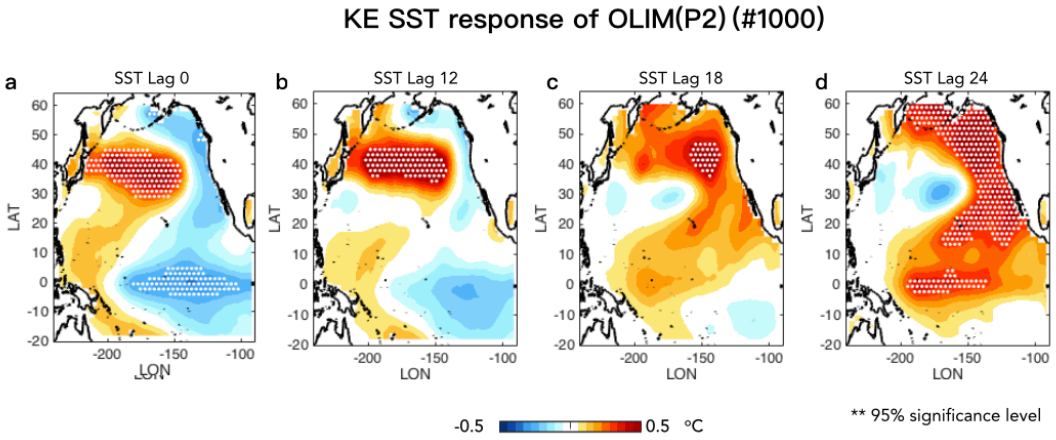

Figure S4.8. Spatial evolution of KE SST in OLIM ensemble for the recent period. LIM ensemble mean of regression between the KE index and lagged SST anomalies in each realization. A dot symbol denotes the grid whose signal is significant at the 95% confidence level in composite SST anomalies using a Monte-Carlo approach.

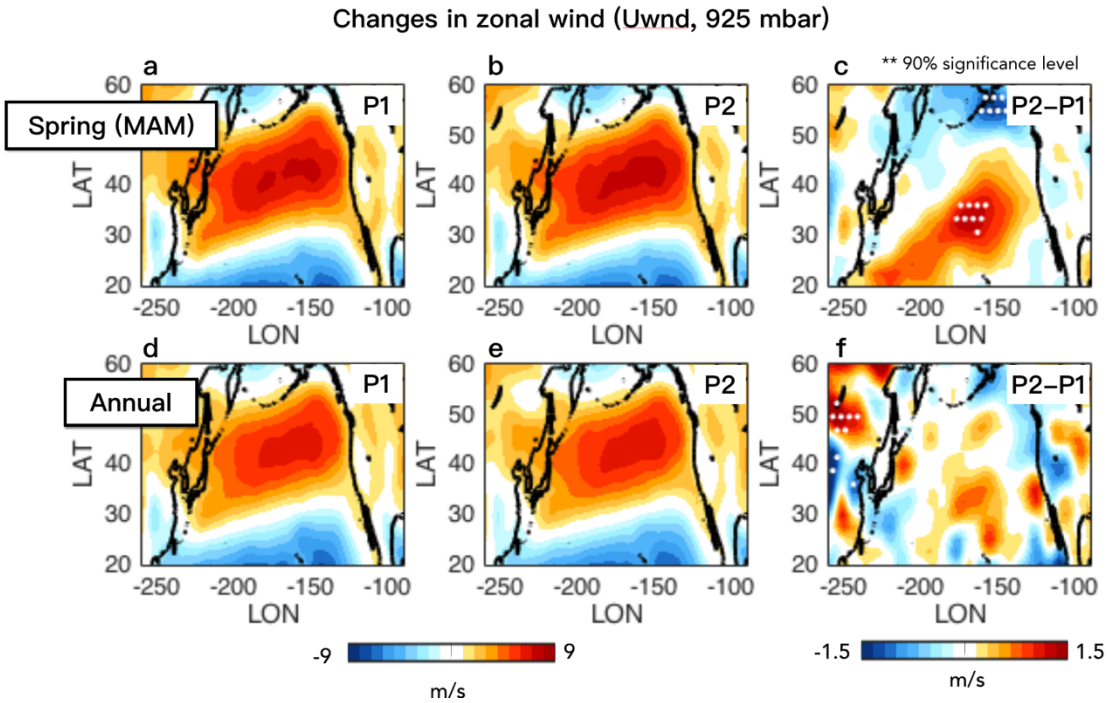

Figure S4.9. Seasonality of changes in surface wind climatology. Long-term mean of 925mb zonal wind for spring season (March-April-May) during (a) P1 and (b) P2 and (c) their difference (P2-P1). (c-f) Same as (a-c), but for the whole season. A dot symbol denotes the grid whose signal is significant at the 90% confidence level using a Monte-Carlo approach.

4.7. References

Pierce, D. M. et al. The role of ocean dynamics in producing decadal climate variability in the North Pacific.*Climate Dyn.*, **18**, 51–70 (2001).

Kwon, Y.-O., and Deser. C. North Pacific decadal variability in the Community Climate System Model version 2. *J. Climate*, **20**, 2416–2433 (2007).

Qiu, B. Kuroshio Extension variability and forcing of the Pacific decadal oscillations: Responses and potential feedback. *J. Phys. Oceanogr.* **33**, 2465–2482 (2003)

Kwon, Y. O. *et al*. Role of the Gulf Stream and Kuroshio–Oyashio systems in large-scale atmosphere–ocean interaction: A review. *J. Climate* **23**, 3249–3281 (2010).

Na, H., Kim, K. Y., Minobe, S. & Sasaki, Y. N. Interannual to Decadal Variability of the Upper-Ocean Heat Content in the Western North Pacific and Its Relationship to Oceanic and Atmospheric Variability. *J. Climate* **31**, 5107–5125 (2018).

Alexander MA, and Deser C. A mechanism for the recurrence of wintertime midlatitude SST anomalies. J. Phys. Oceanogr. 122–37 (1995).

Xue, H., Bane, J. M. Jr. & Goodman, L. M. Modification of the Gulf Stream through strong air–sea interactions in winter: Observations and numerical simulations. *J. Phys. Oceanogr.* **25**, 533–557 (1995).

Frankignual et al. A simple model of the decadal response of the ocean to stochastic wind stress forcing. J. Phys. Oceanogr., **27**, 1533–1546 (1997).

Qiu, B. Interannual variability of the Kuroshio Extension and its impact on the wintertime SST field. *J. Phys. Oceanogr.* **30**, 1486–1502 (2000).

Nakamura, H., and A. S. K. Decadal changes in the North Pacific oceanic frontal zones as revealed in ship and satellite observations. *J. Geophys. Res.*, **108**, 3078 (2003) https://doi.org/10.1029/1999JC000085.

Nakamura, H., Sampe, T., Tanimoto, Y. & Shimpo, A. Observed associations among storm tracks, jet streams and midlatitude oceanic fronts. Earth's Climate: The Ocean-Atmosphere Interaction, *Geophys. Monogr.* **147**, Amer. Geophys. Union, 329–346 (2004).

Kelly, K. A., R. J. Small, R. M. Samelson, B. Qiu, T. M. Joyce, Y.-O. Kwon, and M. Cronin, Western boundary currents and frontal air–sea interaction: Gulf Stream and Kuroshio Extension, J. Clim., **23**, 5644–5667 (2010).

Mizuno, K., and White, W. B. Annual and interannual variability in the Kuroshio Current System, *J. Phys. Oceanogr.*, **13**, 1847–1867 (1983).

Yasuda, I., K. Okuda, and M. Hirai Evolution of a Kuroshio warm-core ring—Variability of the hydrographic structure. Deep-Sea Res., **39**, S131–S161 (1992).

Qiu B. Seasonal eddy field modulation of the North Pacific subtropical countercurrent: TOPEX/Poseidon observations and theory. J Phys Oceanogr **29**, 2471–2486 (1999).

Ma, X. et al. Distant influence of Kuroshio eddies on North Pacific weather patterns? *Sci. Rep.*, **5**, 17785 (2015) doi:https://doi.org/10.1038/srep17785.

Qiu, B., Schneider, N. & Chen, S. Coupled decadal variability in the North Pacific: An observationally constrained idealized model. *J. Climate* **20**, 3602–3620 (2007).

Newman, M. *et al*. The Pacific Decadal Oscillation, Revisited. *J. Climate* **29**, 4399–4427 (2016).

Qiu, B., Chen, S. & Schneider, N. Coupled decadal prediction of the dynamic state of the Kuroshio Extension System. *J. Climate* **27**, 1751–1764 (2014).

Anderson, B. T. Empirical Evidence Linking the Pacific Decadal Precession to Kuroshio Extension Variability. J. Geophys. Res. Atmos., **124**, 12845–12863. (2019). https://doi.org/10.1029/2019JD031163

Anderson, B. T., Gianotti, D. J. S., Furtado, J. C. & Di Lorenzo, E. A decadal precession of atmospheric pressures over the North Pacific. *Geophys. Res. Lett.* **43**(8), 3921–3927, https://doi.org/10.1002/2016gl068206 (2016).

Anderson, B. T., Furtado, J. C., Di Lorenzo, E. & Gianotti, D. J. S. Tracking the Pacific Decadal Precession. *J. Geophys. Res.-Atmos.* **122** (6), 3214–3227, https://doi.org/10.1002/2016jd025962 (2017).

Siqueira, L., L. C. Laurindo, and B. Kirtman. Forecasting Remote Atmospheric Responses to Decadal Kuroshio Stability Transitions. (submitted to *J. Clim* on Jul 29, 2020 and in revision now).

Joh, Y., Di Lorenzo, E. Interactions between Kuroshio Extension and Central Tropical Pacific lead to preferred decadal-timescale oscillations in Pacific climate. *Sci Rep* **9**, 13558 (2019). https://doi.org/10.1038/s41598-019-49927-y

Deser, C., and Blackmon, M. L. On the relationship between tropical and North Pacific sea surface temperature variations. J. Climate, **8**, 1677–1680 (1995).

Nakamura, H., G. Lin, and Yamagata, T. Decadal climate variability in the North Pacific during the recent decades, *Bull. Am. Meteorol. Soc.*, **78**, 2215–2225 (1997).

Zhang Y, Wallace JM, Battisti DS ENSO-like interdecadal variability: 1900–93. J Clim **10**, 1004–1020 (1997)

Seager, R., Kushnir, Y., Naik, N. H., Cane, M. A. & Miller, J. Wind-driven shifts in the latitude of the Kuroshio–Oyashio Extension and generation of SST anomalies on decadal timescales. *J. Climate* **14**, 4249–4265 (2001).

Ceballos, L., Di Lorenzo, E., Hoyos, C. D., Schneider, N. & Taguchi, B. North Pacific Gyre Oscillation synchronizes climate variability in the eastern and western boundary current systems. *J. Climate* **22**, 5163–5174 (2009).

Fankignoual, C., Sennechael, N., Kwon, Y. O. & Alexander, M. A. Influence of the meridional shifts of the Kuroshio and the Oyashio Extensions on the atmospheric circulation. *J. Climate* **24**, 762–777 (2010).

Taguchi, B., S. P.Xie, N.Schneider, M.Nonaka, H.Sasaki, and Sasai, Y. Decadal variability of the Kuroshio extension: Observations and an eddy-resolving model hindcast.*J. Climate*, **20**, 2357–2377 (2007).

Bretherton, C. S., C. Smith, and Wallace, J. M. An intercomparison of methods for finding coupled patterns in climate data. J. Climate, **5**, 541–560 (1992).

Wallace, J. M., D. S. Gutzler, and Bretheron, C. S. Singular value decomposition of wintertime sea surface temperature and 500-mb height anomalies, J. Clim., **5**, 561 – 576 (1992).

Tootle, G. A., and Piechota T. C. Relationships between Pacific and Atlantic ocean sea surface temperatures and U.S. streamflow variability, Water Resour. Res., **42**, W07411 (2006). doi:10.1029/2005WR004184

Miller, A. J., Cayan, D. R. & White, W. B. A westward intensified decadal change in the North Pacific thermocline and gyre-scale circulation. *J. Climate* 11, 3112–3127 (1998).

Deser, C., M. A. Alexander, and Timlin, M. S. Evidence for a Wind-Driven Intensification of the Kuroshio Current Extension from the 1970s to the 1980s. J. Climate, **12**, 1697–1706 (1999) https://doi.org/10.1175/1520-0442(1999)012<1697:EFAWDI>2.0.CO;2.

Schneider, N., A. J. Miller, and Pierce, D. W. Anatomy of North Pacific decadal variability. J. Climate, **15**(6), 586–605 (2002). https://doi.org/10.1175/15200442(2002)015<0586:aonpdv>2.0.co;2.9.

Sasaki, Y. N., Minobe, S., and Schneider, N. (2013). Decadal response of the Kuroshio Extension jet to Rossby waves: Observation and thin-jet theory. J. Phys. Oceanogr., 43, 442–456. https://doi.org/10.1175/JPO-D-12-096.1.

Frankignoul C, Muller P, Zorita E A simple model of the decadal response of the ocean to stochastic wind forcing. J Phys Oceanogr **27**:1533–1546 (1997)

Qiu B and Chen, S. Variability of the Kuroshio extension jet, recirculation gyre, and mesoscale eddies on decadal time scales. J Phys Oceanogr **35**, 2090–2103 (2005).

Penland, C., Random forcing and forecasting using principal oscillation pattern analysis. Mon. Wea. Rev., **117**, 2165–2185 (1989).

Penland, C. A stochastic model of Indo-Pacific sea surface temperature anomalies, *Phys. D*, **98**, 534–558 (1996).

Penland, C., and Matrosova, L. A balance condition for stochastic numerical models with application to the El Niño–Southern Oscillation, *J. Clim.*, **7**, 1352–1372 (1994).

DelSole, T., Hou, and A. Y. Empirical correction of a dynamical model. Part I: Fundamental issues. Mon. Wea. Rev., **127**, 2533–2545 (1999).

Newman, M., Interannual to decadal predictability of tropical and North Pacific sea surface temperatures. *J. Climate*, **20**, 2333–2356 (2007) doi:https://doi.org/10.1175/JCLI4165.1.

Alexander, M. A., L.Matrosova, C.Penland, J. D.Scott, and Chang, P. Forecasting Pacific SSTs: Linear inverse model predictions of the PDO. *J. Climate*, **21**, 385–402 (2008) doi:https://doi.org/10.1175/2007JCLI1849.1.

Capotondi, A., and Sardeshmukh, P. D. Optimal precursors of different types of ENSO events. *Geophys. Res. Lett.*, **42**, 9952–9960 (2015) https://doi.org/10.1002/2015GL066171.

Chiang, J. C. H. & Vimont, D. J. Analogous Pacific and Atlantic Meridional Modes of Tropical Atmosphere-Ocean Variability. *J. Climate* **17**, 4143–4158 (2004).

Lian, T., Chen, D., Tang, Y. & Wu, Q. Effects of westerly wind bursts on El Niño: A new perspective. *Geophys. Res. Lett.* **41**, 3522–3527, https://doi.org/10.1002/2014GL059989 (2014)

Zhang, H., A. Clement, and Di Nezio P. The South-Pacific meridional mode: A mechanism for ENSO-like variability, *J. Clim.*, **27**, 769–783 (2014).

Di Lorenzo, E. *et al*. ENSO and meridional modes: A null hypothesis for Pacific climate variability. *Geophys. Res. Lett.* **42**, 9440–9448 (2015)

Xie, S. P. & Philander, S. G. H. A coupled ocean-atmosphere model of relevance to the ITCZ in the eastern Pacific. *Tellus* **46A**, 340–350 (1994).

Vimont, D. J., Wallace, J. W. & Battisti, D. S. The Seasonal Footprinting Mechanism in the Pacific: Implications for ENSO. *J. Climate* **16**, 2668–2675 (2003).

Di Lorenzo, E., & Mantua, N. (2016). Multi-year persistence of the 2014/15 North Pacific marine heatwave. *Nature Climate Change*, **6(11)**, 1042–1047.

Kilduff, D. P., Di Lorenzo, E., Botsford, L. W. & Teo, S. L. H. Changing central Pacific El Ninos reduce stability of North American salmon survival rates. *Proceedings of the National Academy of Sciences of the United States of America* **112(35)**, 10962–10966 (2015).

Joh, Y. & Di Lorenzo, E. Increasing coupling between NPGO and PDO leads to prolonged marine heatwaves in the Northeast Pacific. *Geophys. Res. Lett* **44(11)**, 663–11,671 (2017)

Liguori, G. & Di Lorenzo, E. Meridional Modes and Increasing Pacific Decadal Variability Under Anthropogenic Forcing. *Geophys. Res. Lett.* **45**, 983–991 (2018).

Gent, P. R., et al. (2011), The Community Climate System Model Version 4, *J. Clim.*, **24**, 4973–4991.

Taylor, K. E., R. J. Stouffer, and Meehl, G. A. An overview of CMIP5 and the experiment design, *Bull. Am. Meteorol. Soc.*, **90**, (2012) 485–498, doi:10.1175/BAMS-D-11-00094.1.

Murray, M. J., M. R.Allen, and Mutlow, C. T. Global evaluation of sea surface temperature retrievals from the along-track scanning radiometer through comparison with the NOAA operational analysis.Tech. Rep. RAL-TR-96-60, 12 pp (1996)

Kirtman, B. P. et al., Impact of ocean model resolution on CCSM climate simulations, Climate Dyn., 39, 1303 (2012) https://doi.org/10.1007/s00382-012-1500-3.

Kirtman, B. P., et al: The subseasonal experiment (subx). IRI Data Library, doi:10.7916/d8pg249h

Balmaseda, M. A., Vidard, A. & Anderson, D. The ECMWF ORA-S3 ocean analysis system. *Mon. Weather Rev.* **136**, 3018–3034 (2008).

Carton, J. A., Chepurin, G. A. & Chen, L. SODA3: A New Ocean Climate Reanalysis. *J. Climate* **31**, 6967–6983 (2018).

Smith, T. M., R. W. Reynolds, R. E. Livezey, and Stokes, D. C. Reconstruction of Historical Sea Surface Temperatures Using Empirical Orthogonal Functions. *J. Climate*, **9**,

1403–1420 (1996) https://doi.org/10.1175/1520-0442(1996)009<1403:ROHSST>2.0.CO;2.

Dee, D. P. *et al*. The ERA-Interim reanalysis: configuration and performance of the data assimilation system. *Meteorol. Soc.* **137**, 553–597 (2011).